2007

Silicon carbide biocompatibility, surface control, and electronic cellular interaction for biosensing applications

Camilla Coletti
University of South Florida

Silicon Carbide Biocompatibility, Surface Control and Electronic Cellular Interaction for Biosensing Applications

by

Camilla Coletti

A dissertation submitted in partial fulfillment
of the requirements for the degree of
Doctor of Philosophy in Electrical Engineering
Department of Electrical Engineering
College of Engineering
University of South Florida

Major Professor: Stephen E. Saddow, Ph.D.
Andrew M. Hoff, Ph.D.
Mark J. Jaroszeski, Ph.D.
Ulrich Starke, Ph. D.
Jing Wang, Ph. D.

Date of Approval:
October 9, 2007

Keywords: biological cell, semiconductor, hybrid system,
surface topography, surface potential, surface chemistry

Dedication

To Gene, for making home a better place, for having the patience to be with me 24/7, and for sharing with me the good and the bad of most of these three years of 'Florida-life' (including the long sleepless nights which resulted in this manuscript).

To Mom Anna Enrica, Dad Fabiano and Sis Giulia for all the love, the continuous support and the daily endless phone calls which made me feel at home in Italy with them every day of these three long years. Despite the ocean.

Acknowledgments

In the first place I wish to thank Dr. S.E. Saddow, who offered me the chance to start a doctorate program in his group and provided moral and financial support through all these years. My gratitude also goes to Dr. A.M. Hoff, Dr. M.J. Jaroszeski, Dr. U. Starke, and Dr. J. Wang, for agreeing to serve on my Ph.D. committee and for providing valuable suggestions for the improvement of the manuscript. For their assistance in LEED and AES measurements (Chapter 2), my gratitude goes to M. Hetzel and Dr. C. Virojanadara of Dr. Starke's group at the MPI of Stuttgart (DE). C. Coggins of PSIA (Santa Clara, CA) is ackowledeged for her contribution in AFM imaging (§ 3.1.4). I wish to thank Dr. Iannotta of the IFN-CNR of Trento (IT) and his group, in particular A. Pallaoro and T. Toccoli for their contribution in the wettability studies and Drs. M. Nardi and R. Verrucchi for their contribution in XPS studies (§ 3.2.3 and § 3.3.3). I am thankful to Dr. B. Grayson and J. Jimenez of USF for their valuable assistance in XPS and ATR-FTIR measurements, respectively (§ 4.4.2). I owe the survival of my cell cultures in my periods of absence from the lab to R. Connelly, N. Ramachandran and D. Bazley to whom I am most grateful. For technical support with CPD instrumentation I wish to thank Dr. E. Oborina and SDI (Semiconductor Diagnostic Inc., Tampa, FL). For providing a very enjoyable working atmosphere and helping me in many issues whose list would be too long to be contained in one page I deeply thank my colleagues and friends: Chris Frewin, Ian Haselbarth, Chris Locke, Norelli Schettini, and Dr. Jeremy Walker.

Table of Contents

List of Tables

List of Figures

Silicon Carbide Biocompatibility, Surface Control and
Electronic Cellular Interaction for Biosensing Applications

Camilla Coletti

ABSTRACT

Cell-semiconductor hybrid systems are a potential centerpiece in the scenery of biotechnological applications. The selection and study of promising crystalline semiconductor materials for bio-sensing applications is at the basis of the development of such hybrid systems. In this work we introduce crystalline SiC as an extremely appealing material for bio-applications. For the first time we report biocompatibility studies of different SiC polytypes whose results document the biocompatibility of this material and its capability of directly interfacing cells without the need of surface functionalization. Since the successful implementation of biosensors requires a good understanding and versatile control of the semiconductor surface properties, the chemistry, crystallography and electronic status of different SiC surfaces are extensively studied while their surface morphologies are thoroughly controlled via hydrogen etching. Also, investigations of the effect of cell surface charge on the electronic status of SiC surfaces are attempted adopting a contactless surface potential monitoring technique. The results obtained from these contactless measurements lead to the development of theoretical models well-suited for the description of cell-semiconductor hybrid systems electronic interactions.

Chapter 1. Introduction

1.1. Research objective and motivation

Cell-semiconductor hybrid systems represent an emerging topic of research in the biotechnological area with intriguing possible applications. A comprehensive understanding of the interactions governing such systems is the basis of present and future development of biologically interfaced device performance. To date, very little is known about the main processes that govern the communication between cells and the surfaces they adhere to. When cells adhere to an external surface an eterophilic binding is generated between the cell adhesion proteins and the surface molecules. After they adhere, the interface between them and the substrate becomes a dynamic environment where surface chemistry, topology, and electronic properties have been shown to play important roles [1-3]. Although previous works have demonstrated that cells display a net charge on their external surface [4-7] little is known about cell-semiconductor electronic interactions. Studying how and in which magnitude the electronic properties of biological entities such as cells may influence and interact with the electronic status of a crystal, and describing it with the means provided by solid-state physics would be an enormous step forward in science and would represent the foundation for successful future implementation of electrically based bio-sensors.

For this purpose, a suitable crystalline material displaying both biomedical and sensing potentialities should be selected and its properties fully characterized. A direct

interfacing of cells with the selected semiconductor is a requirement for the detection, study and modeling of electronic signals. However, to date, the biocompatibility of only a few crystalline semiconductors has been investigated, with Si and titanium dioxide (TiO_2) drawing most of the attention [3, 8-12]. In fact, since the present trend in research is the functionalization and polymer coating of semiconducting surfaces, simple biocompatibility studies of crystalline semiconductor materials have been mostly neglected. Both Si and Ti are unsuitable for the purpose of studying cellular electronic interactions with semiconductors. Si has been shown to display different degrees of cytotoxicity, mostly due to its instability in aqueous solutions with subsequent formation of silica and silicates, which are known for their harmful effects on cells [9, 13, 14]. On the other hand, TiO_2, which can become a semiconductor upon ion implantation [3], does not display sufficiently satisfying electronic properties that may justify its adoption for electronic sensing applications. Therefore, it appears evident that there is a need for the introduction of a different semiconducting material that, displaying both biocompatibility and great sensing potentiality may fill the existing gap.

Single-crystal silicon carbide (SiC) is a wide band gap semiconductor with vast sensing potentiality, very resistant to wear and corrosion, and with optimal tribological properties. In the past, because of its chemical inertness and superior resistance, the amorphous phase (a-SiC) of this promising material has been suggested for prosthesis and implant coating [15, 16]. For the same reasons, a-SiC biocompatibility has been widely studied yielding promising results [17-19]. Also, a-SiC has been found to be highly haemocompatible and an optimal coating for heart stents [20]. Although amorphous SiC has been widely characterized by bio-medical research, surprisingly, to

date, no studies report on the biocompatibility of crystalline SiC, which, because of its wide electronic energy band gap, appears particularly appealing for bio-sensing applications.

For the reasons listed above, we selected crystalline SiC as the ideal substrate material for bio-sensing investigations which may uncover the complex nature of semiconductor-cell electronic communication. Since the degree of success in the use of a semiconductor material for biosensing applications strongly depends on its biocompatibility and surface properties, we exhaustively studied crystalline SiC biocompatibility and characterized SiC surfaces at a chemical, crystallographic and morphological level. The interesting and insightful results obtained in the course of these studies are reported in the next chapters and, for the most part, are novel contributions that range from surface science to biomedical fields.

Cell-semiconductor electronic interaction investigations were also part of this project. For these studies, we used fully characterized SiC surfaces in combination with a contactless surface potential monitoring technique: contact potential difference (CPD) measurements. The CPD technique was selected because of its extremely appealing capability of monitoring the potential of a surface without discharging it. The main idea at the basis of this experiment was to monitor the effect that the cell charge has on the electronic status (e.g., energy band bending → surface potential) of a semiconductor. Specifically, its implementation consists of monitoring, via CPD, the surface potential variation caused by the presence of cells cultured or deposited directly on SiC substrates. The success of such measurements would, as mentioned before, greatly impact the modeling and design of electronic biosensors. However, to the extent that the final goal is

attractive, its implementation is equally challenging. One of the major obstacles involved with the CPD monitoring of cell-semiconductor systems resides in the fact that cells need to be immersed in liquid (e.g., culturing media) to be kept alive. This requirement introduces a significant challenge since the few CPD measurement attempts in the past using objects immersed in liquid have provided conflicting results [21-23]. Another issue related with the design of these CPD experiments is the very limited knowledge that we have presently on the effective charge of a cell immersed in an electrolyte. The only experimental technique currently used with success which is capable of detecting the cell surface charge is electrophoresis [5, 24, 25]. However, because of theoretical and modeling problems, the electrophoretic data do not allow a direct calculation of the cell charge. As a result, except for erythrocytes, no estimations of the surface charge of cells are found in the existent literature. The lack of a definite quantification of this charge adds difficulty to the proper design of CPD experiments.

Thanks to a suitable experimental approach we were able to overcome electrolyte-related experimental issues and to successfully perform CPD measurements on surfaces immersed in liquids. This allowed us to electronically characterize the semiconductor-electrolyte interface and move towards the desired cell-semiconductor electronic interaction investigations. Our attempts to monitor possible changes in the semiconductor band bending due to the presence of live cells are also reported in this work and provide interesting information and the basis for future cell-semiconductor electronic interaction studies.

In this chapter we first describe the general characteristics of single-crystal SiC and the present knowledge of the bio-medical potentialities of its amorphous phase (§ 1.2).

We then give a brief overview of all techniques used in our work to characterize SiC surfaces (§ 1.3) and focus in particular on the CPD monitoring technique which is used later in this work for cell-semiconductor electronic interaction investigations (§ 1.4).

1.2. Silicon carbide: a promising material for bio-sensing applications

To the best of our knowledge, this is the first work that introduces crystalline SiC as a promising biomaterial for bio-sensing applications. In the following sections we review the basic properties of this interesting semiconductor (§ 1.2.1) and the background information related to the use of its amorphous form, a-SiC, in biomedical research (§ 1.2.2).

1.2.1. SiC general properties

Naturally occurring silicon carbide (SiC), which has the gem name of moissianite, was first observed in 1893 by Henri Moissan in the Canyon Diablo meteorite in Arizona. SiC is, in fact, extremely rare in nature and typically found only in minute quantities in corundum deposits, kimberlite, and meteorites. Analysis of SiC grains contained in meteorites revealed that this material originated from stars evolved in higher-metallicity regions than our galaxy and suggested that SiC is older than our solar system [26]. To date, more than 170 crystalline forms of SiC can be synthesized, which is a property called polytypism. A tetrahedron of four carbon atoms covalently bonded to a silicon atom in the centre is at the basis of every SiC crystal (Fig. 1.1). Each carbon atom is located 3.08 Å from the others, while the distance between the silicon and the carbon atom is 1.89 Å.

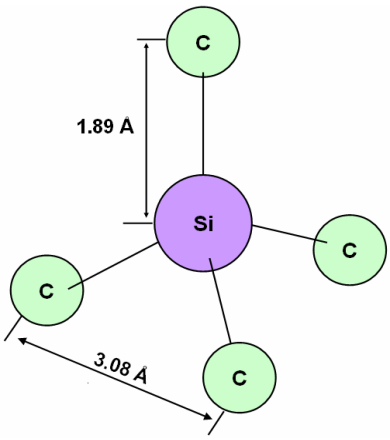

Figure 1.1. Tetrahedron building block of all SiC crystals showing the bond lengths between Si and C atoms.

An interesting feature of SiC is that it displays a two-dimensional polymorphism called polytypism. All the SiC crystals have a hexagonal frame of Si and C bilayers. The stacking order between succeeding double layers of carbon and silicon atoms is a variable that defines the different polytypes of SiC. Specifically, in Fig. 1.2 the three different positions that the hexagonal frame can assume in the lattice are reported and referenced as A, B, and C.

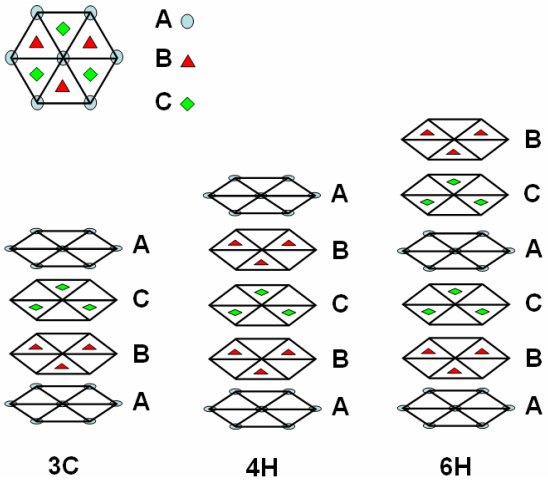

Figure 1.2. Illustration of the three different positions that the hexagonal frame of SiC bilayers can assume in the lattice (top) and stacking sequence of the three most common polytypes (bottom).

What is defined as the cubic polytype (β- or 3C-SiC) in SiC presents a stacking sequence ABCABC.... The hexagonal polytypes, 4H- and 6H-SiC (α-SiC), have stacking sequences of ABCBABCB… and ABCACBABCACB…, respectively (Fig. 1.2). Due to the different crystallographic structure, different polytypes present different electronic and optical characteristics. The electron energy band gap is 2.39 eV for 3C-SiC, 3.023 eV for 6H-SiC, and 3.265 eV for 4H-SiC [27].

The properties that make this material particularly promising for biosensing applications are: 1) the wide bandgap that, as mentioned before, increases the sensing capabilities of a semiconductor; 2) the chemical inertness that suggests the material resistance to corrosion in harsh environments such as body fluids (e.g. SiC does not react with any known material at room temperature, the only efficient etch being molten KOH at 400-600 ºC); 3) the high hardness (5.8 GPa), high elastic modulus (424 GPa), and low friction coefficient (0.17) that make it an ideal material for smart-implants and *in-vivo* biosensors [15, 28, 29].

As we mentioned above, the three major polytypes of SiC present different properties. For completeness in this work we characterized the surfaces and evaluated the biocompatibility of the most studied SiC polytype (e.g., 3C-, 4H-, 6H-SiC).

1.2.2. SiC as a biomaterial: background information

Even though crystalline SiC biocompatibility has not been investigated in the past, information exists concerning the biocompatibility of the amorphous phase of this material (a-SiC). First, it is important to mention that a-SiC is one of the principal materials of choice for cardiovascular applications. In fact, a-SiC haemocompatibility has

been not only suggested by numerous studies [29-31] but also greatly proved by the successful use of a-SiC coated heart stents in *in-vivo* clinical trials. In fact, to date, hydrogen rich amorphous SiC (a-SiC:H, also known as Tenax) coated stents have been implanted in thousands of moderate-to-high risk patients yielding only a minor incidence of adverse events [20, 32-35]. At present, a-SiC:H is known for its high thromboresistance induced by the optimal barrier that this material presents for protein (and therefore platelet) adhesion. Also, amorphous SiC superior tribological and mechanical properties, together with the fact that it exhibits hydroxyapatite-like osseointegration, make it an excellent candidate material for medical prosthetic implants [16, 36]. Although *in-vivo* trials of SiC coated hip or oral prostheses have not been performed (or at least reported) to date, *in-vitro* preliminary studies have shown promising results [16, 17, 37]. On the other hand, one of the possible drawbacks that may be associated with the use of SiC *in-vivo* is related to the unclear and highly debated cytotoxic level of SiC particles [38, 39, 17, 18]. Nonetheless, we believe that the potential cytotoxicity of SiC particles does not represent a dramatic issue as much as it does for Si, since the great tribological properties of SiC make it less likely to generate debris.

In conclusion, most of the studies conducted in the past on a-SiC provide evidence of the attractive bio-potentialities of this material and hence suggest similar properties for crystalline SiC. The promising information found in the literature combined with the well-known sensing potentiality of single-crystal SiC are at the basis of our choice to investigate the potentialities of this material for bio-sensing applications.

1.3. Surface characterization tools

We previously mentioned that a successful implementation of a material for bio-sensing applications largely depends on the chemical, crystallographic and morphological properties of its surface. In fact, it is present knowledge that the bonding of cell adhesion proteins to the molecules of a foreign surface is mostly influenced by the chemistry, hydrophilicity, morphology, and electrostatics of the surface itself [1-3]. For these reasons, this work also focused on the characterization of the surface of the semiconducting material that we propose as ideal for bio-sensing applications, namely SiC. In order to study SiC surfaces, we used different characterization techniques whose main features are reported below:

Atomic force microscopy (AFM) operates by measuring the atomic forces between a sharp probing tip (typically a few nm in radius) and a sample surface. Even though it can be updated for different uses (e.g., magnetic characterization in magnetic force microscopy (MFM), doping profiling in scanning spreading resistance microscopy (SSRM), etc.) the basic AFM system is used for morphological characterization of surfaces. The AFM can operate in several modes: contact (the cantilever contacts the surface while experiencing repulsive van der Waals forces), non contact (the cantilever is held above the surface and senses the attractive van der Waals forces), and tapping mode (e.g., the cantilever vibrates at or near its resonant frequency and 'taps' the surface). The AFM basic principle of operation is the following: a cantilever with a sharp tip is dragged across the sample surface while a laser is focused on the back side of the cantilever. The vertical probe motion is then sensed by a position-sensitive photodetector and a feedback loop adjusts the probe-sample separation to maintain a constant amplitude and force on

the probe. Hence, the feedback loop gives a measurement of the sample height variation. The measurements are typically performed in atmosphere but, with proper equipment, can also be performed in vacuum. All the AFM results presented in this work were obtained working under atmosphere and, if not otherwise specified, in tapping mode. For the imaging in liquid, the contact mode was used.

Scanning electron microscopy (SEM) is a technique for qualitative morphological characterization of a sample surface. An electron beam with electron energies ranging from 10 to 30 keV is raster-scanned across the sample surface and the resulting electrons emitted from the sample are collected to form an image of the surface. SEM resolution is lower than that obtainable from AFM. Therefore, for high resolution and quantitative information the AFM method is preferred. SEM is typically used in this work to obtain large-scale characterization of sample surfaces followed by quantitative evaluation via AFM.

Low energy electron diffraction (LEED) is used to investigate the crystallography of sample surfaces. Specifically, low energy (10-1000 eV) electrons incident on the sample are diffracted by the periodic arrangement of the atoms. The diffracted electrons emerge from the surface in directions satisfying interference conditions from the crystal periodicity and strike a fluorescent screen, forming a distinct array of diffraction spots due to the orientation of the crystal lattice of the sample [40]. Obviously, because of their low energy, the incident electrons penetrate only a few atomic layers into the surface. The LEED results presented in Chapter 2 were obtained in an ultra-high vacuum (UHV) analysis chamber at the Max Planck Institute (Stuttgart, DE) equipped with LEED optics,

an electron spectrometer for AES, a Si evaporator and sample heating facilities. The pressure in the chamber during the measurements was in the 10^{-11} mbar range.

Auger electron spectroscopy (AES) is a chemical characterization technique based on the Auger effect which describes the phenomenon in physics for which the emission of an electron from an atom causes the filling of a vacancy in an inner electron shell. Specifically, primary electrons with typically 1-5 keV energy are emitted from an electron gun and impinge on the studied surface. If its energy is sufficient, an incident electron can remove a core state electron from a surface atom. This now empty core state can be filled by an outer shell electron from the same atom, in which case the electron moves to a lower energy state. The energy associated with this transition is typically imparted to a second outer shell electron, the Auger electron, which hence is ejected from the atom. The characteristic energy of this ejected electron defines the originating atom. By analyzing the resulting energy spectra it is possible to determine the chemical composition of the studied surface with the exception of hydrogen and helium, which, having less than three electrons, cannot be detected by this technique. The sampling depth of AES ranges from 0.5 to 5 nm [40]. The AES results presented in Chapter 2 were obtained in the same ultra-high vacuum (UHV) analysis chamber used for the LEED investigations. The energy of the incident electron beam was 2.25 keV. The pressure in the chamber during the measurements was again in the 10^{-11} mbar range.

X-ray photoelectron spectroscopy (XPS) is a chemical characterization technique based on the photoelectric effect which allows, as AES, identification of elements and their chemical status, with the exception of hydrogen and helium (in theory hydrogen and helium could be detected by using a very good spectrometer). Primary X-rays with

energies of 1 to 2 keV (e.g., Mg K_α radiation or Al K_α radiation) impinge on the sample surface causing ejection of electrons from any orbital. Obviously, photoemission occurs only for X-ray energies exceeding the electron binding energy. Therefore, each element generates a characteristic set of peaks in the photoelectron spectrum at kinetic energies determined by the photon energy and the respective binding energies. Analysis of the peaks allows determination of the composition of the sample surface. Like AES, XPS allows sampling depths in the 0.5-5 nm range. All the XPS results presented in this work were obtained working at a maximum pressure of 10^{-9} mbar.

Total attenuated reflectance Fourier transform infrared spectroscopy (ATR-FTIR) is a chemical characterization technique which uses IR to determine the molecular composition of a surface. The FTIR principle of operation is based on the fact that part of the incident infrared radiation is absorbed by molecules only if the frequency of the radiation provides energy in the exact quantity required by the bonds to vibrate. The infrared spectra collected after the beam has passed through the sample is indicative of the chemical bonds present at the surface (i.e., different molecules absorb at different characteristic frequencies). Unlike AES and XPS, this technique is capable of detecting H and its compounds. Attenuated total reflectance (ATR) is used in particular for obtaining IR spectra of difficult samples such as the solid/liquid interface. ATR occurs when the incident beam enters from a more-dense (with a higher refractive index) into a less-dense (with a lower refractive index) medium. The evanescent wave from the primary optical beam penetrates a very short distance beyond the interface and into the less-dense medium before the complete reflection occurs (typically a few μm). The wave intensity is reduced by the sample in regions of the IR spectrum where molecular absorption takes

place. To utilize the ATR effect, the sample is placed in close contact with a high-refractive-index optical crystal. A 45 º beveled zinc selenide (ZnSe) crystal was used in the ATR-FTIR experiments performed in this work. Atmospheric CO_2 and H_2O absorption lines were reduced by purging the apparatus with dry nitrogen [41].

Other surface characterization techniques and experimental apparatus were sporadically used during the course of this research project, and will be introduced as the corresponding results are presented.

1.4. Contact potential difference technique for cell-semiconductor electronic interaction studies

Contact potential difference (CPD) measurement is the technique selected in this research project for investigation of cell-semiconductor electronic interactions. In this section we first introduce semiconductor energy band diagrams, which are of primary importance for a complete understanding of the CPD technique (§ 1.4.1), and then discuss the principle of operation behind CPD measurements (§ 1.4.2). In § 1.4.3, we describe how CPD measurements can be used to detect charges on a semiconducting surface. Also, since the CPD investigations we intend to perform involve a liquid layer which wets the semiconductor surface, it is important to discuss energy band diagrams for liquids and the existent theory for semiconductor/electrolyte interfaces (§ 1.4.4) and to use this information to model the CPD measurements of semiconductor-electrolyte systems (§ 1.4.5).

1.4.1. Semiconductor energy band diagrams

The energy spectrum of an ideal semiconductor presents two different typologies of energy levels: the allowed energy levels, situated within the conduction and the valence bands, and the forbidden energy levels, situated within the so-called band gap. Energy band diagrams of semiconductors are characterized by: the conduction band edge, E_c, which is the lowest unfilled energy level in the conduction band; the valence band edge, E_v, which is the uppermost filled energy level in the valence band; the Fermi level, E_F, which represents the maximum energy occupied by an electron at 0 K; the energy band gap, E_g, which is given by $E_c - E_v$ and contains all the forbidden energy levels; and the vacuum energy level, E_0, which is a reference level representing the energy of a free electron. The basic band diagram for a semiconductor is sketched in Fig. 1.3. Besides those already listed, different quantities appear in this figure: the difference between E_0 and E_F is called the work function, $q\varphi$, and represents the average energy required to extract an electron from the semiconducting surface; while the difference between E_0 and E_c is called the electron affinity, qX, and is the energy necessary to free an electron from the conduction band edge. In an intrinsic semiconductor (where electrons and holes are present in equal amounts), the Fermi level is near the middle of the forbidden gap and is called the intrinsic Fermi level (E_i). However, for n-type semiconductors (i.e., electrons are majority carriers) $E_F > E_i$ and for a p-type semiconductors (i.e., holes are majority carriers) $E_F < E_i$. This basic information will help the reader to understand better the energy band diagrams presented in the remainder of this work.

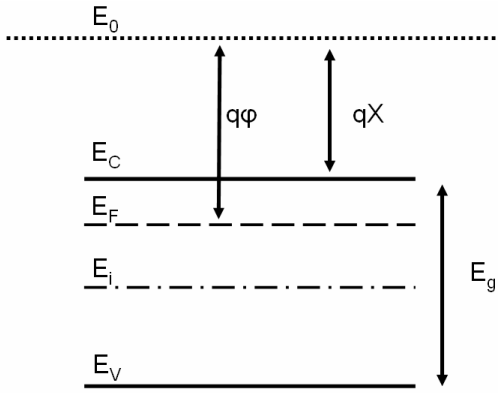

Figure 1.3. Energy band diagram for an ideal n-type semiconductor.

Fig. 1.3 represents the energy band diagram of an ideal semiconductor, where it is assumed that the allowed energy states at the surface are not different from those in the bulk. However this assumption is not valid for a real semiconductor, where the asymmetric nature of the crystal at the surface (atoms at the surface are only single-side bonded) and the existence of crystal defects and foreign bonded atoms introduce extra-allowed energy states. These allowed energy states are known as surface states and vary in energy and typology. For example, states that are neutral when occupied by electrons and positively charged when unoccupied are classified as donor states. States that are negative when occupied but neutral when empty are classified as acceptor states. This nomenclature will be often used in the following chapters. The major effect that surface states have on an energy band diagram, and therefore on the electronic status of a semiconductor, is that of generating a band bending (e.g., the surface is naturally charged). In fact it is the change in the band bending near semiconductor surfaces that is typically exploited in sensing applications and thus the key physical concept to take away from this introductory discussion.

Now that we have presented the basics of semiconductor energy band diagrams, we introduce the concept of surface potential that is the quantity measured by the dark/light CPD technique to be presented later. The surface potential, φ_s, is a measure of the semiconductor surface departure from the state of electrical neutrality, and is measured as the energy difference between the conduction band (valence band) edge at the surface and the conduction band (valence band) edge in the undisturbed part (e.g., the bulk) of the semiconductor. From this definition it is clear that an ideal semiconductor presents a null surface potential, while the surface potential of a real semiconductor is not zero because of the existence of surface states. In fact surface states cause a natural charging of the semiconductor surface with subsequent depletion or accumulation of majority carriers within the surface region. The band diagram for a real n-type semiconductor, and its relative surface potential, is reported in Fig. 1.4.

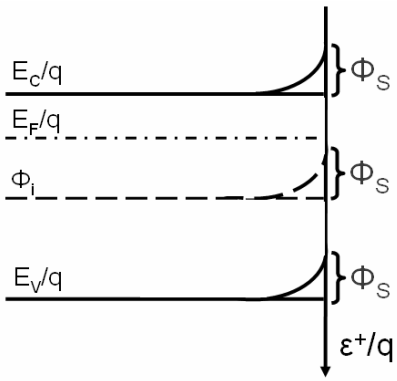

Figure 1.4. Energy band diagram of a real n-type semiconductor which contains an amount of band bending at the surface. The dotted lines (small dots) represent the ideal condition for E_c/q, E_v/q and φ_i. The surface potential φ_s is indicated.

As is evident from Fig. 1.4, the surface potential can equally be defined using as a reference level the intrinsic potential, φ_i. The surface region where depletion or accumulation of the majority carriers take place is named the space charge region (SCR).

The electronic condition where the SCR is depleted of majority carriers is called depletion and corresponds to an upward bending of the bands for n-type ($\varphi_s < 0$, Fig. 1.4) and a downward bending of the bands ($\varphi_s > 0$) for p-type semiconductors. In the case where the majority carriers accumulate at the surface (e.g., the condition named accumulation), the bands bend down ($\varphi_s > 0$) for n-type and up ($\varphi_s < 0$) for p-type semiconductors. The condition for which the intrinsic potential and the surface potential coincide is called flatband and obviously in this case $\varphi_s = 0$. The treatment of these concepts will be resumed later in Chapter 4.

1.4.2. CPD principles of operation

Surface potentials of a semiconductor are commonly measured via dark/light contact potential difference (CPD) measurements. In a CPD apparatus, a pick-up electrode (i.e., probe) is placed near the semiconductor surface, whose back-side is grounded, hence forming a capacitor, C, with the semiconductor. Either a Monroe or Kelvin probe can be used for this purpose [42]. Since in the apparatus implemented for this work we used a Monroe probe [43], which typically presents a low sensitivity to external vibrations, we now describe the Monroe probe-CPD principle of operation.

The final value obtained from a CPD measurement is the contact potential difference, V_{cpd}, between the probe and the sample. This voltage can be easily detected by a Monroe probe-electrostatic voltmeter combination in the fashion we now describe. In the Monroe probe, the electrode is fixed and a grounded shutter, mounted in front of the electrode, is vibrated horizontally, varying the area of the capacitor plates and thereby modulating the probe-to-wafer capacitance as shown in Fig. 1.5 (e.g., $C = \varepsilon \cdot A/d$ where C

is the capacitance, A is the area of each plate, d is the separation between the plates and ε is the permittivity of the insulator between the plates).

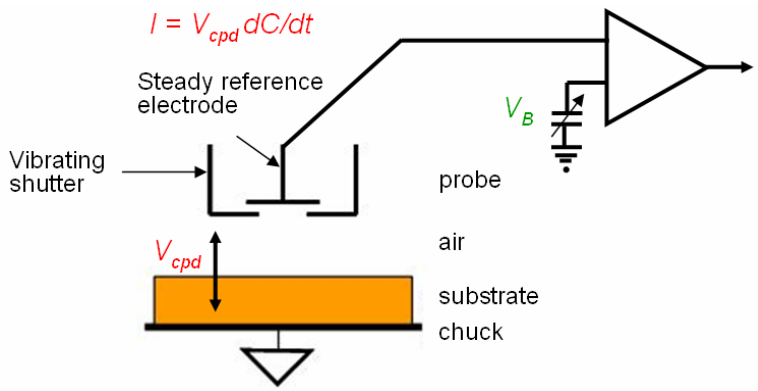

Figure 1.5. Schematic representation of a Monroe probe-grounded sample system.

Because of the vibrating shutters the capacitance is time variable. Since $I = V_{cpd}\, dC/dt$, an alternating current (ac) is generated in the electrode. The contact potential difference V_{cpd} is determined by the electronics of the electrostatic voltmeter by applying the null-arrangement, initially proposed by Kelvin [44]. Specifically, the current generated in the probe is nullified by adjusting the bias voltage V_B until $I = 0$, in which case $V_B = V_{cpd}$. Summarizing, a CPD apparatus determines the contact potential difference that exists between the probing electrode and the investigated semiconductor by means of a current-nulling method applied on the current signal generated by a variable capacitor.

Let us now introduce the principle of operation of dark/light CPD measurements and explain how this technique yields the surface potential of the analyzed sample. In dark/light CPD two contact potential difference values are measured: $V_{cpd,dark}$ which is the value measured as described before in dark, and $V_{cpd,light}$ which is the value obtained

under deep illumination of the sample. Assuming that the chuck-semiconductor contact is ohmic the CPD value measured in dark is a sum of different contributing potentials:

$$V_{cpd,dark} = V_{FB} + V_{air} + \varphi_s \quad (1)$$

where the flatband voltage, V_{FB}, is a function of the metal-semiconductor work function difference and V_{air} is the voltage drop associated with the air. Moreover, if an oxide is present at the semiconductor surface the contact potential difference measured at the probe is given by:

$$V_{cpd,dark} = V_{FB} + V_{air} + V_{ox} + \varphi_s \quad (2)$$

where V_{ox} is the voltage drop associated with the oxide. As is evident from (1) and (2), a single CPD measurement is insufficient to determine the surface potential of a semiconductor. This is why measurements under deep illumination are performed. Light-CPD measurements are performed using a light source with a photon energy higher than the energy band gap of the semiconductor under study. Therefore, electrons are excited from the valence band to the conduction band (i.e., electron hole pair (EHP) generation) and force the semiconductor to a flatband condition ($\varphi_s \rightarrow 0$). Hence the contact potential difference measured by the probe under intense illumination is:

$$V_{cpd,light} = V_{FB} + V_{air} + V_{ox} \quad (3)$$

Therefore the surface potential can be easily calculated as the difference between these two measurements:

$$\varphi_s = V_{cpd,dark} - V_{cpd,light} \quad (4)$$

1.4.3. CPD measurements for charge detection: general considerations

It is now clear what a surface potential is and how dark/light CPD measurements detect it. Presently, this technique is widely used for the determination of the effect of

chemical treatments and ionic charges on a semiconductor surface. In fact, charges deposited or trapped on the semiconductor surface induce a bending of the energy bands. The entity of this band bending, and therefore the sign and magnitude of the charge at the surface, can be determined by performing CPD measurements of the surface not charged and comparing the measured φ_s value with the one obtained for the same charged surface. Let us now consider an n-type semiconductor in a naturally depleted condition (e.g., majority carrier absence in the SCR) as the one depicted in Fig. 1.6(a). By adding negative charges on its surface we will enhance the magnitude of the band bending (e.g., majority carriers are pushed deeper into the semiconductor bulk because of repulsion from the negative charge at the surface, Fig. 1.6(b)). CPD measurements of the surface in these two different conditions will yield different values of φ_s. Supposing that we did not know the sign of the deposited charge, a shift of φs towards more negative values upon charge addition would have been a direct indication that the charge deposited was negative. Upon previous corona charge characterization of the specific semiconducting surface we would also be able, by comparing the two measured φ_s values, to define the magnitude of the deposited charge [45].

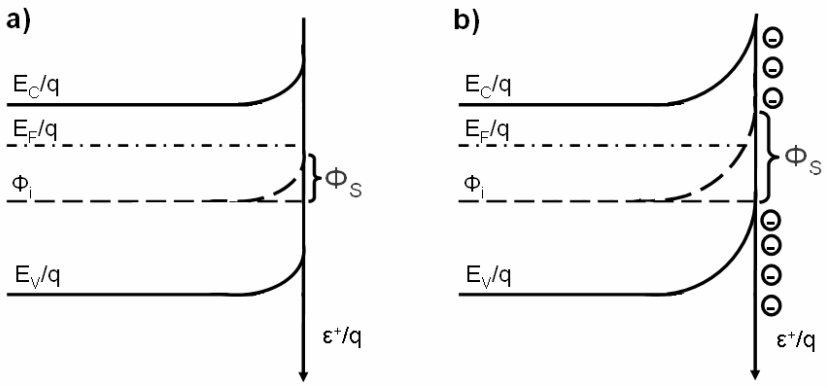

Figure 1.6. Energy band diagram of an n-type semiconductor (a) not charged and (b) with the negative charges on the surface. Note the difference in magnitude of the two φ_s values.

Only one thing could actually impede an estimation of the amount of charge deposited on the surface: surface state density. In fact, when measuring the surface potential via CPD we are actually measuring the capacitor formed between the probe and the semiconductor surface. On the semiconductor surface (e.g., one plate of the capacitor), the charge is a sum of the charge in the SCR and that in the surface states. Therefore the capacitance measured via CPD is a parallel combination of the surface state capacitance C_{ss} and the space charge capacitance C_{sc}. The presence of a high density of surface states may cause Fermi level pinning [13, 46], in which case charge addition on the semiconducting surface will not result in a response of excess charge in the SCR and the value of C_{ss} will be predominant in the capacitance measured via CPD.

As we already pointed out our goal is to implement the CPD technique for detecting the charge associated with cells once they are cultured/deposited on SiC surfaces. Obviously, this can be achieved only if the surfaces we use present a reduced amount of surface states. This issue will be treated later in Chapters 2 and 4.

1.4.4. The electrolyte-semiconductor interface

As explained in the previous section, CPD dark/light measurements of a bare semiconductor surface allow determination of the semiconductor surface potential. However, in this project we aim to perform CPD measurements of a more complex structure, the semiconductor-cell-electrolyte system, for the determination of the surface potential variation induced in a semiconductor by the presence of charged cells. For this purpose we will perform CPD measurements of the semiconductor-electrolyte and semiconductor-cell-electrolyte systems and compare the surface potentials calculated for the two cases. Eventual differences in these values would allow us to define the effect of the charge of cells on the electronic status of a semiconductor. To be able to understand the results obtained from CPD measurements of semiconductors immersed in electrolytes we first need to model the semiconductor/electrolyte interface. For this purpose we introduce an existent model that electronically characterizes this complex interface and subsequently apply it for the modeling of our CPD measurements (§ 1.4.4).

Let us first introduce the distribution of energy levels within an electrolyte as we did for a semiconductor in § 1.4.1. An electrolyte is electronically characterized by: a redox energy level, E_{RedOx}, which defines the average energy level at equilibrium of all the individual redox species; the most probable energy level of the reduced species, E_{Red}; and the most probable energy level of the oxidized species, E_{Ox}. A schematic representation of the energy band diagram for an electrolyte is reported in Fig. 1.7 and, also in this case, referenced to the energy vacuum level, E_0.

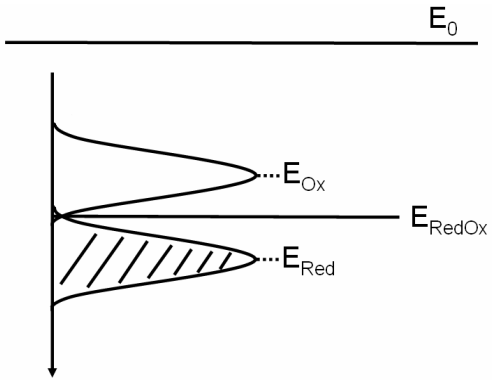

Figure 1.7. Electron energy levels for an electrolyte with respect to the vacuum level.

Immersion of a semiconductor in an electrolyte results in a charge transfer process (i.e., electron exchange) between the two phases until equilibrium is obtained, that is when the Fermi level in the semiconductor and the redox level in the electrolyte are equal ($E_F = E_{RedOx}$). This produces an electric field at the semiconductor/electrolyte interface which generates an electrical double layer well described by the Stern model depicted in Fig. 1.8.

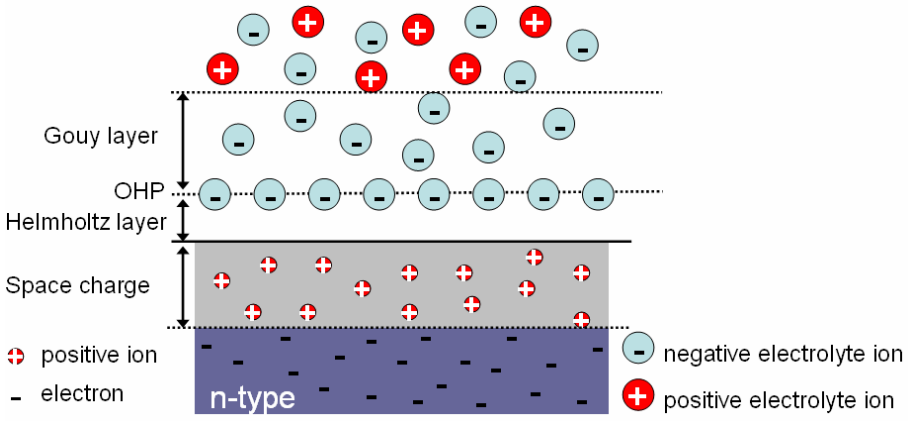

Figure 1.8. Electrical double layer model describing the charge distribution at an n-type semiconductor/electrolyte interface.

On the electrolyte side the position of the closest approach of mobile ions is called the outer Helmholtz plane (OHP). The Helmholtz layer is the region between the

semiconductor surface and the OHP and contains ions attracted to the semiconductor surface by the excess charge in the space charge region and by polar water molecules. Outside of the Helmholtz layer a region with excess ions of one sign whose thickness depends on the electrolyte concentration exists, the so-called Gouy layer [13, 47]. As is evident from Fig. 1.9, the Gouy layer is a diffuse space charge region with excess ions of the same sign as those accumulating in the OHP.

1.4.5. Modeling of CPD measurements of electrolyte-semiconductor systems

Now that we have introduced the existent model for semiconductor/electrolyte interfaces we can apply this knowledge to model the CPD measurements in liquid that we will describe in Chapter 5 and that may lead to a better understanding of the semiconductor-cell electronic interaction.

When measuring, via CPD, a semiconductor-electrolyte system different voltage drop contributions will sum to yield the Vcpd value measured by the Monroe probe. To ensure that the value obtained from the difference of dark and light measurements is the surface potential (i.e., $\varphi_s = V_{cpd,dark} - V_{cpd,light}$) all the additional voltage drops should be constant values independent of the illumination. Furthermore, we must define their magnitude to ensure that their contribution is not predominant in the measured V_{cpd} value. An equivalent circuit for the electrical components at the semiconductor/electrolyte interface is reported in Fig. 1.9.

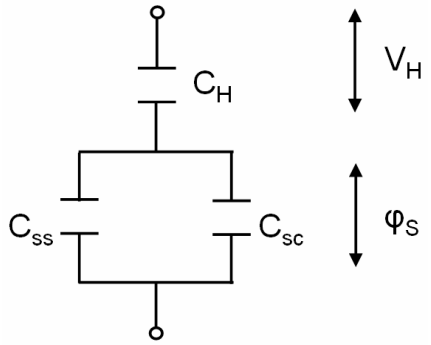

Figure 1.9. Equivalent circuit at the semiconductor/electrolyte interface where C_H, C_{SS} and C_{SC} are the Helmholtz, surface state and space-charge capacitance, respectively.

The voltage drop between the semiconductor bulk and its surface is the value φ_s, which for a dry semiconductor can be directly calculated via dark/light CPD. As discussed in § 1.4.3, this voltage drops across two capacitances in parallel, the space charge capacitance, C_{sc}, and the surface states capacitance, C_{ss}. In a semiconductor-electrolyte system φ_s will also be in series with the voltage drops associated with air (V_{air}), with the Helmholtz layer (V_H) and with the Gouy layer (V_G). However, for electrolyte concentrated solutions (e.g., above 10^{-2} M), the value of V_G is negligible [48]. Therefore the final electronic equivalent circuit in terms of the relevant capacitances will be given by the series of the Helmholz capacitance C_H with the parallel of the space charge capacitance C_{sc} and the surface states capacitance C_{ss}, as shown in Fig. 1.9 and described by equation (5).

$$C_{cpd} = \frac{C_H(C_{sc} + C_{ss})}{C_H + C_{ss} + C_{sc}} \tag{5}$$

Therefore it is evident that in order to monitor the effect that the charge associated with cells has on the electronic status of a semiconductor (e.g., changes to its space charge region) we need: $C_{ss} \ll C_{sc}$ and $C_{sc} \ll C_H$. Since typical values of C_H for a concentrated

solution like the ones used in this work are close to 20 $\mu F/cm^2$ [49] and typical values of C_{sc} for SiC samples range from 10^{-2} to 10^{-1} $\mu F/cm^2$ (depletion to accumulation, respectively) the latter condition can be considered satisfied. Also, the value of C_{sc} is influenced by the doping density in the SiC crystals and, therefore, can be controlled. However C_{ss}, which is determined by the surface state density, is another matter and is highly dependent on how the crystals are prepared and their surfaces treated. Therefore reduction of surface state density on SiC surfaces was attempted using hydrogen etching (Chapter 2) in order to ensure that the above condition was met.

1.5. Summary and dissertation organization

The electronic interactions that exist between biological cells and semiconductors are, to date, unknown. In this work we aim to move towards a better understanding of how, and in which magnitude, the charge of a cell may influence the electronic status of a semiconductor. In order to accomplish this very ambitious objective a semiconductor that combines both biocompatibility and sensing potentialities needs to be selected and fully characterized. In this chapter we introduced crystalline SiC as a promising material for this task: its wide band gap is extremely appealing for sensing applications and the well-known biocompatibility of amorphous SiC likely suggests that the crystalline phase may display similar properties. In order to characterize SiC surfaces different techniques were used in the course of this work, which have been introduced in this chapter. Moreover we suggested an apparently promising technique to investigate cell-semiconductor electronic interactions: contact potential difference (CPD) measurements. Since, to date, no studies report on the direct investigation of the effect of cell charges on semiconductors, the implementation of successful measurements that may lead to uncover the electronic

communication ongoing between the biological and the semiconductor world is pioneering and extremely challenging. Also, although the CPD technique appears to be ideal for our goal because of its contactless nature, its implementation for hybrid system monitoring is not trivial. In particular, the necessary presence of an electrolyte during the measurements complicates the matter and accurate modeling of both the hybrid system, which is the object of measurements, and of the measurement itself due to such artifacts, are required to better design and understand the investigations we performed.

The organization of the dissertation, based on the individual chapters, is as follows. In Chapter 2 we introduce hydrogen etching as an ideal technique for obtaining high quality, atomically flat SiC surfaces with resulting low surface state charge densities. The H-etched surfaces are also perfectly suitable (e.g., well prepared) for surface science studies. This allowed us to characterize in a comprehensive fashion the morphological, chemical, and crystallographic features of SiC surfaces by using AFM, AES, and LEED methods, respectively.

Chapter 3 reports an exhaustive study on the biocompatibility of SiC. Fluorescence microscopy, viability assays and atomic force microscopy were used to characterize the morphology, adhesion quality and proliferation of mammalian cells on SiC substrates. This study, besides offering, for the first time, quantitative and qualitative information on the biocompatibility of SiC, also describes the possibility of directly interfacing cells with SiC surfaces. This result definitely confirms the potentialities of SiC as a biomaterial and an ideal substrate for cell-semiconductor electronic interaction studies.

Chapter 4 describes the implementation of a CPD apparatus for cell-semiconductor electronic interaction studies and reports on the electronic characterization of SiC

surfaces. The effect of charges on SiC substrates is exhaustively investigated and the possibility of passivating electronically the surface of 3C-SiC is presented and discussed.

Chapter 5 reports the procedures developed for CPD measurements of semiconductors immersed in liquids and investigates the effect that different electrolytes have on the electronic status of SiC surfaces. Also, in this chapter we report the procedure and results for CPD measurements of semiconductor-cell-electrolyte systems.

Chapter 6 summarizes the results reported in the previous chapters and uses the knowledge acquired in the course of this research to suggest future developments and possible implementations of cell-semiconductor electronic interaction studies.

Chapter 2. SiC Surface Preparation and Characterization

In order to succeed in the implementation of sensors for biomedical applications the surfaces of the semicoducting materials that are going to be interfaced with cells have to fulfill several requirements. First, they need to be fully characterized at a chemical, crystallographic, and morphological level. It is in fact well known that cell adhesion to a surface is regulated by a combination of chemical, morphological and energetic properties of the surface [1-3]. Also, atomically flat surfaces may be preferable, depending on the targeted application. Specifically, for the investigation of cell-semiconductor electronic interactions that we aim to perform, working with atomically flat surfaces is particularly appealing: the reduction of surface defects and hence of associated surface states surely simplifies the task by reducing trapping at the cell/semiconductor interface.

In this section we present the processes developed for producing atomically flat SiC surfaces, and their chemical and crystallographic characterization. Commercially available SiC crystals present slicing and polishing scratches at the surface as a result of the wafer preparation processes, which imply a high density of surface states in addition to a high surface roughness. Moreover, these surfaces are not feasible for chemical and crystallographic studies, which would allow for their accurate characterization. A comprehensive understanding of the chemical, structural and morphological surface characteristics is of primary importance for all those biosensing applications which, as

the CPD measurements proposed later in this work, rely on the direct interfacing of biological cells and semiconducting material. Hence, the need for a full characterization of the surfaces that will be used in the rest of this work becomes clear.

Scratch-free, passivated SiC surfaces suitable for surface science studies can be obtained by using an appropriate surface preparation technique. The chemical inertness of SiC makes it impossible to use wet chemical etchants to remove the slicing and polishing damage. To date, the SiC surface preparation techniques which have been developed and used with different degrees of success are: oxidation [50, 51], sublimation etching [52], photoelectrochemical etching [53], chemomechanical polishing (CMP) [54], plasma etching [55], and hydrogen etching (H-etching) [56-58]. Among these, the latter has been shown to be the most effective to completely remove polishing scratches while producing atomically flat surfaces perfectly suitable for surface science studies [58-61].

This section focuses on the production and characterization of well-ordered 3C-, 4H- and 6H-SiC surfaces via H-etching in a hot-wall chemical vapor deposition (CVD) reactor. Morphological, crystallographic and chemical analyses are performed via atomic force microscopy (AFM), low energy electron diffraction (LEED) and auger electron spectroscopy (AES), respectively.

2.1. H-etching of SiC surfaces

H-etching of SiC surfaces has been primarily used in the past to improve the surface quality of bulk substrates prior to epitaxial growth [62-64]. It is usually performed in a chemical vapor deposition (CVD) reactor (either hot-wall or cold-wall) flowing variable hydrogen fluxes at high temperatures (typically in the range of 1000-1700 ºC), and at a pressure varying between 100-760 Torr.

Hydrogen etching of SiC is believed to be a two-step process [59, 63], which can be simplified as follows. The high temperature characteristics of the process cause the evaporation of Si atoms from the surface and the subsequent exposure of the underlying C atoms. At this stage, hydrogen atoms from the etching gas bond to the surface C atoms forming hydrocarbons which in turn desorb from the crystal uncovering the next layer of Si which then evaporates, and so on. However, the removal of many monolayers (up to several hundred nanometers) of SiC material not always produces atomically flat and ordered surfaces. First, the morphology of the surface obtained after etching is highly dependent on the original surface condition. If the surface has a high density of hidden defects or presents heavy polishing damage, the etching will expose and enlarge the subsurface defects and worsen the surface morphology. Also, one of the most common problems in SiC H-etching is the condensation of Si droplets on the surface due to the preferential hydrocarbon evaporation caused by the higher equilibrium pressure of C-H groups with respect to Si [62]. Also, over-etching of the SiC surfaces, which results in step-bunching and defect enlargement, must be prevented to achieve an atomically-flat surface. In the following sections, we will use the terminology ‘optimum process’ to designate an etching process which improves the surface morphology and the atomic order of the starting surface without causing the aforementioned drawbacks. Careful planning of the etching experiment, together with an understanding of hydrogen etching kinetics allowed us to develop ‘optimum’ H-etching processes for 3C-, 4H- and 6H-SiC.

2.2. 3C-SiC

In the past, the lack of sufficiently large high-quality 3C-SiC substrates has led to a delay in the development of growth techniques for this polytype and a subsequent lack of

good quality 3C-SiC epilayers. As a consequence, the chemical, morphological and crystallographic characteristics of 3C-SiC epilayers have been investigated on a smaller scale than those of the SiC hexagonal polytypes (i.e., 4H/6H-SiC described in § 2.3).

Since no reports on H-etching of 3C-SiC surfaces were found in the literature, we had no references to help us define the optimal etching parameters. Therefore, in order to develop the 'optimum' etching process, we first studied the effect of H-etching on the morphology of 3C-SiC epilayers for different etching parameters (§ 2.2.1). Etching rates of 3C-SiC(001) for different etching temperatures are reported in § 2.2.2. Crystallographic studies of the 3C-SiC surfaces etched under optimum conditions showed a surface reconstruction (e.g., (5×1)) which has not been investigated previously in the literature and was therefore thoroughly examined in § 2.2.3. Also, the 'optimum' H-etching process presented in § 2.2.1 may be helpful in the development of a H-etching process for the removal of damage and scratches on polished 3C-SiC surfaces after CMP treatment.

2.2.1. Effect of H-etching on the morphology of 3C-SiC surfaces and development of an 'optimum' etching process

The 3C-SiC(001) epilayers used in this work were grown on 8x10 mm Si(001) dice in a low-pressure, hot-wall, horizontal chemical vapor deposition (CVD) reactor [65] using a chlorinated growth chemistry [66]. The film crystallinity was confirmed by x-ray diffraction (XRD) rocking curves [66]. Non-contact doping profiling measurements were also performed which assessed the film doping to be n-type and in the low 10^{15} cm^{-3} range [67]. The thickness of the studied epilayers varied between 2 and 6 μm, as measured by Fourier transform infrared spectroscopy (FTIR). Only the epilayers which

showed, during AFM inspection, similar morphological characteristics were used in this work. AFM micrographs representative of these as-grown 3C-SiC(001) surfaces are shown in Figures 2.1 and 2.2.

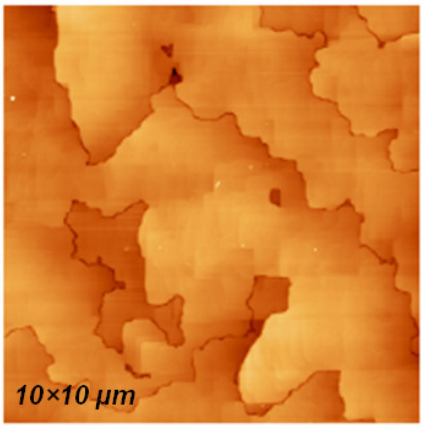

Figure 2.1. 10×10µm AFM micrograph showing the typical surface morphology of 3C-SiC epilayer before H-etching treatment. Note the presence of APDs. AFM data taken in tapping mode.

Figure 2.1 reveals that the as-grown surfaces presented anti-phase domain boundaries (APDs), which are typical features of 3C-SiC films heteroepitaxially grown on Si and are due to the large lattice mismatch (~20%) between the 3C-SiC and the Si crystals.

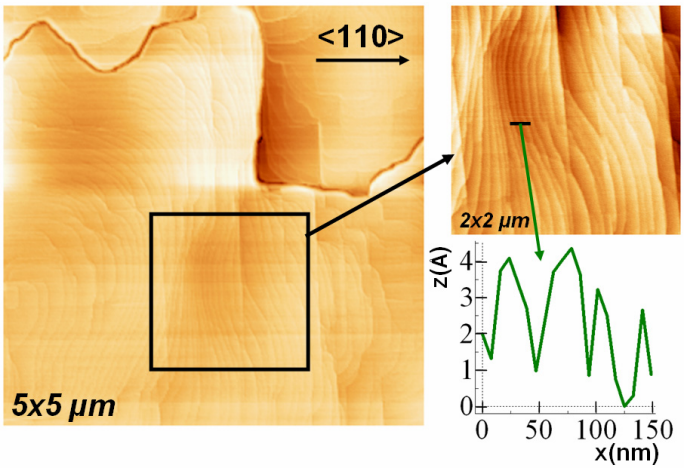

Figure 2.2. 5×5µm AFM micrograph and 2×2µm (inset) of as-grown 3C-SiC(001) epilayers showing atomic steps. Step height and terrace width along the [110] direction are depicted in the higher resolution image and extracted by line profile. AFM data taken in tapping mode.

As is evident from the 5×5 µm micrograph in Fig. 2.2, the samples exhibited the atomic structure of the SiC crystal even immediately after growth. Within individual APDs the AFM images revealed atomically flat terraces with small steps. However, the steps were only loosely aligned along the low-Miller index directions [110] and [$\bar{1}$10] and were rather wavy. Nevertheless, typical step heights, as determined from the higher resolution micrograph and the line profile also displayed in Fig. 2.2, were in the 2-3 Å regime which corresponds well to biatomic steps (2.18 Å) in the 3C-SiC crystal structure which in the <001> direction is characterized by alternating C and Si layers. For reference the trenches observed between different APDs were at least 15 nm deep.

Four parameters can be varied in a H-etching process: temperature (T), pressure (p), hydrogen flow (H_f), and etching time (t_{etch}). In the set of experiments that will be described in this section, which has been designed with the double aim of studying the effect of H-etching on cubic SiC surfaces and developing an 'optimum' etching process,

only temperature was varied from experiment to experiment, while the other parameters were kept constant. Since the epilayers to be etched presented APDs, aggressive etching had to be avoided in order to prevent preferential etching and subsequent enlargement of the trenches (i.e. sites with higher surface energy are subjected to higher etch rates). Low pressure (LP) etching is known to increase the etch rate (Si diffuses better through the thinner boundary layer caused by lower pressures): therefore, the whole set of experiments was performed at atmospheric pressure (AP) while Pd-purified hydrogen was flown at the moderate rate of 10 SLM (standard liters per minute). H-etching of a crystal operates in an opposite fashion than growth, therefore etching temperatures are typically comparable to those used for growth. The 3C-SiC epilayers studied in this work were grown on Si(001) (whose melting temperature is 1410 ºC) at temperatures around 1385 ºC. However, for our experiments, we opted for a lower range of etching temperatures (between 1200 and 1350 ºC) since a low processing temperature has fewer requirements on the reactor, lower cost and reduced contamination. An etching time of 30 min was chosen as a constant in all the experiments performed.

To summarize, all the etching experiments were performed at AP, flowing 10 SLM of Pd-purified hydrogen, for 30 min and with temperatures ranging between 1200 and 1350 ºC in a hot-wall CVD reactor specifically designed for 3C-SiC growth and processing [68]. The reactor hot-zone graphite and parts used were not exposed to growth in order to minimize the possibility that particles removed during the growth would deposit on the SiC surface. In order to remove the native oxide present on the 3C-SiC epilayers, the samples were dipped in a 50:1 mixture of de-ionized (DI) water and hydrofluoridic acid (HF), rinsed with DI water, and dried with nitrogen. The samples

were then immediately loaded into the reactor and brought under vacuum so as to minimize the growth of any native oxide on the crystal surface. AFM micrographs representative of the surfaces obtained after etching at 1200, 1300 and 1350 ºC are reported in Figures 2.3 and 2.4.

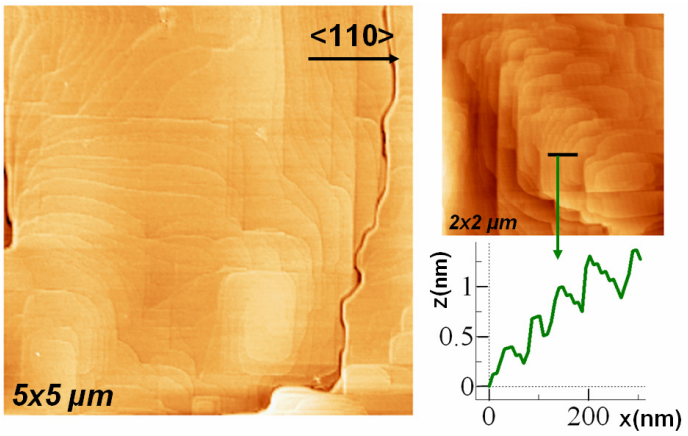

Figure 2.3. 5×5µm AFM micrograph and 2×2µm inset of a typical 3C-SiC surface after H-etching at 1200 ºC. Step height and terrace width along the [110] direction are depicted in the higher resolution image and extracted by line profile. AFM data taken in tapping mode.

As is immediately evident by comparison of the three AFM micrographs shown in Figures 2.3 and 2.4, the best surface morphology was obtained after etching at 1200 ºC. The samples etched at this temperature, in fact, presented a well-defined cubic morphology with steps perfectly aligned along the [110] and [$\bar{1}$10] directions, as shown in Figure 2.3. The more clear alignment of the atomic steps along the low-Miller index directions represent an evident improvement of the processed surface with respect to the as-grown (un-etched) surface of Figure 2.2. Again the terraces are atomically flat, 50–100 nm wide, and typically separated by 2–3 Å steps as seen from the higher resolution image and corresponding line profile in Figure 2.3. Step bunching to multiples of the 2.18 Å

value was only occasionally observed, while the trenches of the APDs did not appear to be enlarged or deepened when compared to the as-grown (un-etched) samples.

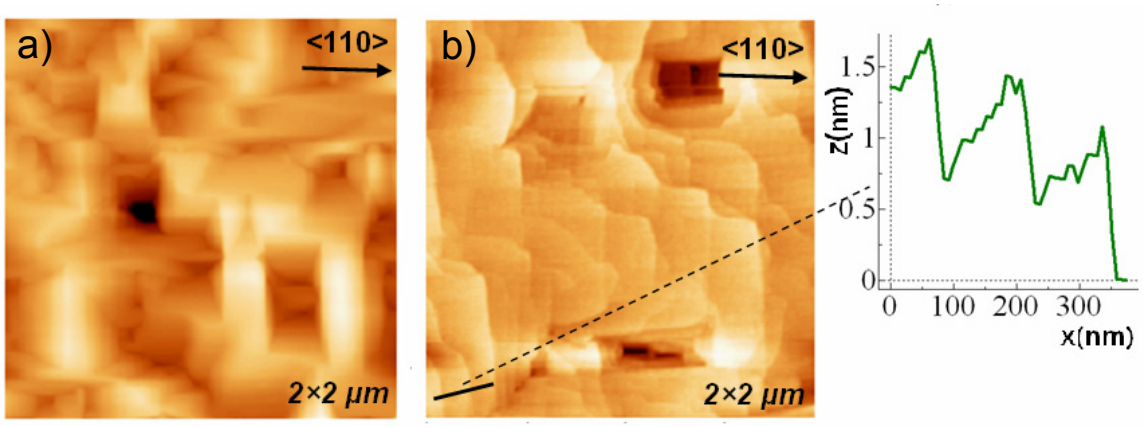

Figure 2.4. 2×2μm AFM micrographs of the morphology of 3C-SiC surfaces etched at 1350 ºC (a) and 1300 ºC (b), respectively. Note the highly damaged surface after etching at 1350 ºC. As a reference, R_q = 35 nm for image (a) while is 0.88 nm for image (b). The line profile along the [110] direction is extracted from figure (b) and depicts the step height and terrace width. AFM data taken in tapping mode.

On the other hand, a significant enlargement of defects (generally in the form of square-shaped pits) was observed in samples etched at 1300 °C. At this temperature, step bunching becomes evident, as indicated by the higher step heights (0.8-1.2 nm) and larger terrace widths (150-400 nm) depicted in Fig. 2.4(b) and in the extracted line profile. At 1350 °C, a drastic change of the surface morphology into a highly mosaic cubic structure was observed (Fig. 2.4(a)). As a reference, the root mean square roughness (R_q) of a 2×2μm AFM micrograph of samples etched at 1300 °C was typically less than 1 nm and comparable to the roughness of samples either as-grown or H-etched at 1200 °C. Instead, the highly damaged samples etched at 1350 °C presented a R_q higher than 30 nm.

SEM studies, while adding new information in a more macroscopic scale, confirmed what was revealed by AFM analysis. SEM micrographs of samples etched at

1200, 1250, 1300 and 1350 °C are shown in Figure 2.5. For as-grown samples, SEM analysis revealed a significant presence of two defect types on the surface: SiC cluster hillocks and film cracks. A micrograph of the surface crack feature is shown in Figure 2.5(a). In samples etched at 1200 °C we found a surface pit density similar to the original surface crack density. Since the pit defects (Fig. 2.5(b)) were never found on as-grown surfaces it is logical to assume that these are enlargements of the surface cracks caused by hydrogen etching. In support of this assumption are the SEM micrographs of samples etched at 1300 °C presenting very large and deep pits extending down to the Si substrate (Fig. 2.5(c)). Fig. 2.5(d) shows the highly damaged mosaic structure, already observed via AFM, of surfaces etched at 1350 °C, which is caused by the aggressive preferential etching of surface defects and grain boundaries that takes place at this temperature. It has to be mentioned that surfaces etched at 1250 ºC were also studied via AFM and SEM. While AFM micrographs revealed no evident morphological differences with respect to the samples etched at 1200 ºC, SEM analysis showed a higher density of pits and defects on these surfaces.

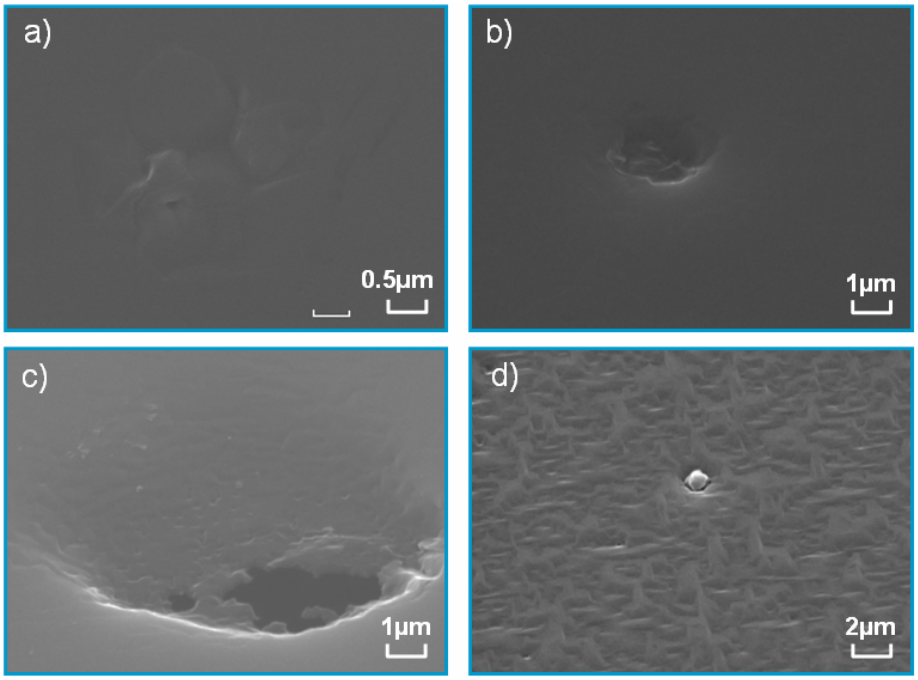

Figure 2.5. Plan-view SEM micrographs of typical defects observed on as-grown (a) and H-etched samples at 1200 (b), 1300 (c) and 1350 °C (d), respectively. A growth hillock is present in the center of the highly damaged mosaic surface morphology depicted in (d) for reference [69].

From the reported results we can conclude that the 'optimum' process parameters for the 3C-SiC(001) epilayers studied in this work are the following: p = 760 torr, T = 1200 ºC, H_f = 10 SLM, and t_{etch} = 30 min. However, for a more complete study of the effect of H-etching on 3C-SiC(001) we also performed etching processes where either the pressure or the etching time were varied with respect to the 'optimum' values. An etching time of 10 to 20 min seemed to produce little or no differences on the macroscopic surface morphology. However, the resulting atomic steps appeared to be less clearly aligned with the [110] and [$\bar{1}$10] directions for shorter etching processes. Also, as expected, LP processes provoked a more aggressive etching of the surface defects and APD trenches.

2.2.2. H-etching rates of 3C-SiC(001)

The etching rate of 3C-SiC(001) was evaluated at different temperatures by measuring the thickness of the epilayers before and after etching via Fourier Transform Infrared Spectroscopy (FTIR). For this experiment the etching time was fixed at 1 hour, the pressure at 760 torr, H_f was 10 SLM while the etching temperature was varied between 1200 and 1375 ºC. From this set of experiments we observed an exponential dependence of the etching rate on temperature as shown in Fig. 2.6. The mean etch rate and standard deviations were calculated from three etching experiments conducted at each temperature and are reported in Table 2.1. Very small etch rates were observed when etching at temperatures below 1300 °C. Also, it appears that the 'optimum' etching process (1200 °C for 30 min) was actually removing just few monolayers of material. It has to be pointed out that while the thickness variation for samples etched at temperatures higher than 1300 °C was easily resolved by FTIR measurement, the etch rate determination at lower temperatures was affected by the limited sensitivity of the FTIR, the relative flatness of the samples, and the difficulty to perform the measurement always in the same position on the sample.

Table 2.1. Etch rates of 3C-SiC(001) at different temperatures as resolved by FTIR measurement [69]. Values reported as mean ± standard deviation.

T (°C)	1200	1250	1300	1325	1350	1375
Etch rate ± sd (nm/hr)	17.5 ± 6.2	21.3 ± 11.8	75.1 ± 9.9	170 ± 2.8	344.5 ± 25.9	580.5 ± 45.9

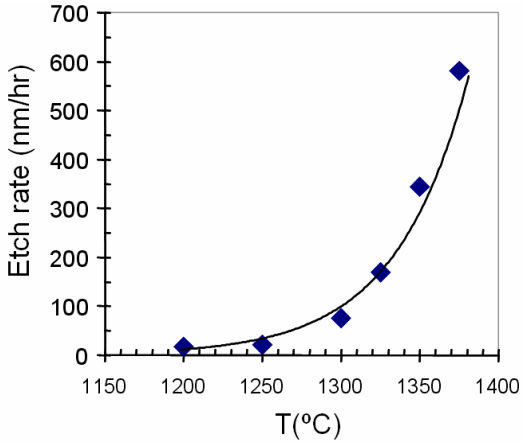

Figure 2.6. Etch rates of 3C-SiC(001) versus H-etch temperature as measured by FTIR. Note exponential dependence of etch rate vs. temperature with only a few monolayers of material removed at the optimum temperature of 1200 °C [69].

2.2.3. Crystallographic studies and chemical analysis of the near surface region: LEED, AES

The surface structure and the chemical composition of the near surface region of the 3C-SiC(001) samples etched with the 'optimum' process were investigated in a ultra-high vacuum (UHV) analysis chamber at the Max-Planck-Institute (Stuttgart, DE). This was accomplished via low-energy electron diffraction (LEED) and Auger electron spectroscopy (AES) analysis conducted on a set of 4 samples. The UHV chamber was equipped with LEED optics, an electron spectrometer for AES, a Si evaporator and sample heating facilities. The pressure in the chamber during the measurements was in the 10^{-11} mbar range. The symmetry and location of the diffraction spots in the LEED pattern were used to reveal surface order and superstructure periodicities. Comparison of peak intensities of the differentiated AES spectra served to determine relative concentrations of elements in the near surface region. The samples were investigated in UHV in their native state after hydrogen etching and subsequently after Si deposition and

annealing at different temperatures. As-grown samples, cooled down under Ar flow, were also studied for comparison.

After loading into the UHV chamber and without any intermediate treatment, the samples revealed a sharp LEED pattern of approximate (5×1) periodicity. Fig. 2.7(a) shows the superposition of the diffraction patterns of two domain orientations of this structure rotated by 90° with respect to each other. A similar LEED pattern has been briefly noted by Kaplan [70] to occur during the partial reduction of a strongly oxidized 3C-SiC(001) surface, however, without being further interpreted. In our study we observed that the long unit vector of the supercell was not exactly an integer multiple of the substrate (1×1) unit vector. Rather, the superstructure was incommensurate and its unit vector varied on different samples of nominally equal preparation. We found supercell sizes varying in the range from (4.5×1) to (6.5×1). It appeared that the substrate and the overlayer fail to have a precise epitaxial relationship. For convenience, the periodicity of the structure is denoted as "5x1" from this point forward in the text. The chemical composition of the "5×1" structure was investigated using the AES spectra shown in Fig. 2.7(c). Most notably, the as introduced surface contained oxygen as seen in the bottom curve, indicating either the formation of a thin oxide layer after air exposure or, similar to the case of the SiC(0001) and SiC($000\bar{1}$) surfaces, silicate layer formation during the etching process [56]. The significant intensities of the Si and C peaks suggest the oxide thickness to be limited to one or a few atomic layers at most. As inferred from the AES spectra in Fig. 2.7(c) (top curve), the oxygen was completely removed from the surface by flashing the sample in UHV to about 1120 ˚C for 5 min. Concurrently, the "5×1" diffraction spots disappeared from the LEED pattern in favor of a poorly ordered

version of the known (2×1) reconstruction [71]. Evidently, the "5×1" phase represents an ultra-thin reconstructed oxidic layer on the 3C-SiC(001) surface. It should be noted that this "5×1" pattern was found on both H-etched and as-grown epi-layers, and even after RCA cleaning of an as-grown sample.

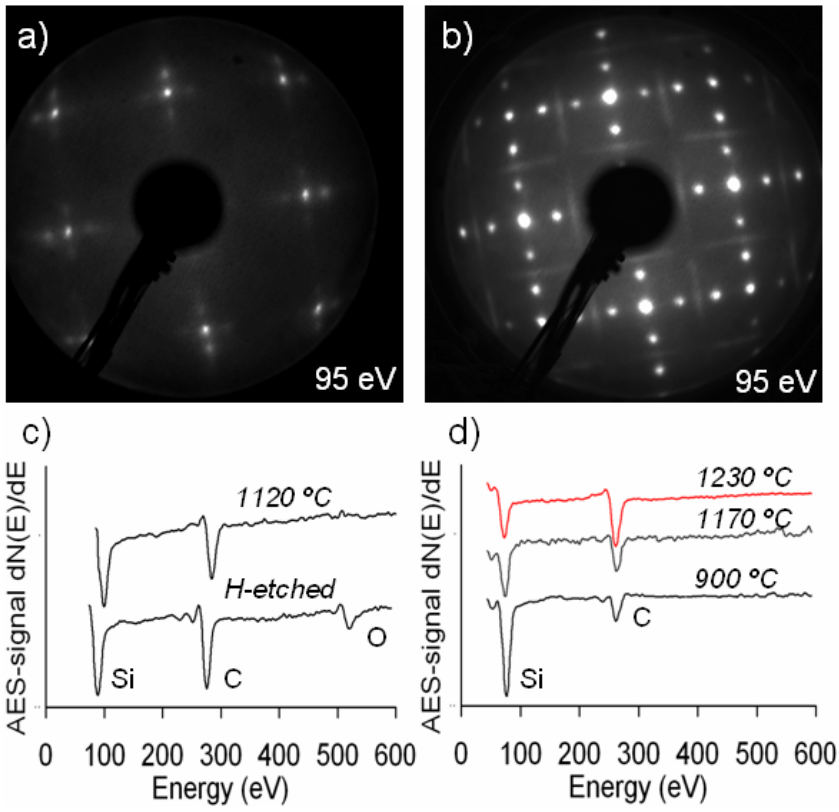

Figure 2.7. UHV analysis of hydrogen etched 3C-SiC(001) samples. (a) LEED pattern of the "5x1" phase as observed after hydrogen etching (without any further treatment). (b) LEED pattern of the (3×2) phase obtained after Si deposition and annealing to 1070 ˚C in UHV. (c) AES spectra with the Si, C and O transitions indicated for the hydrogen etched and the annealed sample, and (d) for the (3×2), (2×1) and c(2×2) phases [72].

The composition of this oxide phase was determined from a comparison with established surface phases on 3C-SiC(001) prepared by Si deposition and subsequent annealing. After stepwise (5 min each) annealing of the Si enriched surface to temperatures in the range of 700-1100 °C, the LEED pattern showed a (3×2) surface

reconstruction with sharp and intense 1/3 order spots on the integer rows, i.e. (m/3,n) spots, and streaky contributions on half order position, i.e. the (m/3,n+1/2) spots, the latter of which were best developed at about 1070 °C (Fig. 2.7(b)). The AES spectra in this temperature range revealed that the surface was still Si-rich (Fig. 2.7(d), bottom curve). At 1170 °C the (3×2) transformed into a well-ordered (2×1) phase. The AES spectrum indicated a lower concentration of Si for this phase (Fig. 2.7(d), middle curve). Annealing to 1230 °C provoked further preferential desorption of Si from the 3C-SiC surface and produced a C-rich surface (top curve in Fig. 2.7(d)) with a c(2×2) LEED pattern. All three phases are well known on 3C-SiC(001) [71]. The (3×2) structure is believed to be strongly Si-rich [73], as also shown by our results. The (2×1) reconstruction is also reported as a Si-rich phase [74], while the c(2×2) phase is usually interpreted as a C-terminated structure [75, 76], which again is consistent with the AES development in our studies.

Table 2.2. AES data for the different structures observed on 3C-SiC(001). Peak-to-peak amplitudes evaluated for differentiated Si, C and O AES signals and element intensity ratios. For comparison data are listed for the so-called silicate layer reconstructions on the basal plane surfaces SiC(0001) and SiC(000$\bar{1}$) taken from ref. [56].

	H-etched "5×1"	1120 °C diffuse (2×1)	(3×2)	(2×1)	c(2×2)	SiO_x-Si-face[56]	SiO_x-C-face[56]
Si	1	0.9	1.2	0.6	0.7	1.4	1.7
C	1.3	0.9	0.3	0.5	0.75	0.75	1.4
O	0.35	-	-	-	-	0.225	0.10
Si/C	0.77	1.0	4.0	1.2	0.95	1.9	1.2
O/Si	0.35	-	-	-	-	0.16	0.06

Table 2.2 summarizes the peak-to-peak amplitudes of the differentiated Si, C and O AES signals and element intensity ratios for all structures observed here on 3C-SiC(001). In addition data are recalled for the so-called silicate layer reconstructions on the basal plane surfaces SiC(0001) and SiC($000\bar{1}$) taken from ref. [56]. Consideration of the Si/C intensity ratio clearly places the "5×1" reconstruction on the less Si rich side of the phase diagram. With some caution one might even favor a carbon termination underneath the oxidic layer. On the other hand the surface might contain some hydrocarbon contamination and the observed C enrichment may not be entirely due to the SiC structure. However, the data definitely rules out that the observed "5×1" structure is a derivative of the UHV prepared (5×2) phase which is known to be strongly Si rich and is characterized by a Si-dimer reconstruction layer [77]. The O/Si ratio observed is slightly higher than for the silicate reconstructions on the basal plane surfaces, which at a first glance suggests the presence of more than one monolayer of oxide. However, on the basal plane surfaces the Si/C ratio is larger than in our hydrogen etched case which, applying the above argument again, could suggest that, after correction for possible carbon contamination, the oxide thickness is similar, i.e. one monolayer in our case. Thus, as a feasible scenario for the oxide related "5×1" reconstruction we suggest the presence of a nearly bulk terminated SiC surface with an oxygen containing reconstruction layer of the observed "5×1" periodicity. The varying interface periodicity suggests a relatively weak bonding relationship between the substrate and the oxide overlayer, which in turn might be due to an (at least partially) internally passivated SiOx network with a certain energetic degeneracy for the distance of adjacent oxide-substrate bonds.

Finally, we should recall the presence of the two-domain superposition in the "5×1" LEED pattern. Due to the alternating layer stacking sequence in the crystallographic <001> direction of 3C-SiC(001), the substrate surface possesses only a two-fold symmetry, which would necessarily imply that only one of the domains can be present. Provided that the interface does not form arbitrarily on both Si and C surface terminating layers, the presence of both domains can only indicate that the 3C-SiC APD's can have both possible epitaxial orientations with respect to the Si(001) substrate, [100] || [100] or [100] || [010]. This is an important observation for possible further optimization of the growth process.

2.3. 4H/6H SiC

Unlike 3C-SiC, H-etching of the SiC hexagonal polytypes (4H- and 6H-SiC) has been largely studied and practiced during the past couple of decades [56-59, 62-64, 78, 79]. Typical etching apparatus are tantalum strip heaters [80], vapor phase epitaxial (VPE) reactors [81], hot-wall [62] and cold-wall CVD reactors [58] where the SiC etching temperatures range between 1400 and 1600 ºC. Low pressure etching or chlorinated chemistry (HCl addition) can be used to increase the etch rate [59]. However, HCl addition has been found to cause preferential etching at low etching temperatures (e.g. 1400 ºC) [59, 81], and in general higher etching rates can worsen the resulting surface if the original substrate is highly scratched or defective. Because of the large amount of information which can be found in the existent literature [56-59, 62-64, 80, 81] the design of the etching processes for 4H- and 6H-SiC has been more straightforward than for 3C-SiC. This implies that no studies of the effect of temperature and pressure on the crystals was necessary in this work. In fact atomically flat surfaces were obtained

both for 4H- and 6H-SiC after the first etching attempt, which was probably due to an accurate choice of the etching parameters based on careful studies of the data found in the existent literature and insightful considerations concerning the kinetics in the CVD reactor used for the processing.

2.3.1. H-etching processes for hexagonal SiC polytypes

Hydrogen etching of both 4H and 6H-SiC samples was performed in a hot-wall CVD reactor mostly used for SiC epilayer growth [65]. The hydrogen flown during the process was Pd-purified. The substrates used in this study were: eight 4H-SiC(0001) 8º off-axis, of which half were chemo-mechanical polished (CMP) by Novasic; two on-axis 4H-SiC(0001); two 3º off-axis 6H-SiC(0001); two on-axis 6H-SiC(0001). All the samples were 8×10 mm diced from SiC bulk crystals purchased from Cree Research, Inc, with n-type doping ranging from 10^{-18} to 10^{-19} cm-3. Also in this case the samples were dipped in H_2O:HF (50:1) and rinsed in DI water just prior to the etching experiments.

Etching of off-axis surfaces is known to be more problematic than for on-axis. Theoretically, one would expect a faster material removal on off-axis surfaces where there is a higher density of high surface energy zones (e.g. steps edges, because of the narrower terraces). Instead, several studies report higher etching rates for on-axis rather than for off-axis SiC surfaces and suggest the use of higher temperatures or more aggressive etching processes to completely remove the polishing scratches from off-axis surfaces [58, 59, 62, 82]. Also, the morphology of off-axis surfaces is reported to be less ordered than that of on-axis, with terraces much narrower (because of the larger off-axis angle) and steps not perfectly oriented along the low-index Miller directions [59, 62].

In this work, we first tried to develop two etching processes, one for off-axis 4H-SiC and one for off-axis 6H-SiC, and successfully adopted them also for etching on-axis samples. Surprisingly, both the designed etching processes produced, independently from the presence of a miscut, atomically flat 4H- and 6H-SiC surfaces, which are described in the next section. Even though the on-axis surfaces present some triangular peninsulas between steps, which may be caused by the use of an etching process specifically designed for off-axis surfaces and therefore more aggressive, their surface quality after etching is still satisfactory. This suggests that the presented etching processes are quite versatile for the etching of both on-axis and off-axis hexagonal SiC surfaces. Also, it has to be pointed out that all the samples used presented polishing scratches prior to H-etching and that those scratches were completely removed by the adopted etching processes.

The etching parameters for the off-axis processes were chosen in an attempt to minimize the etching temperature and based on the following considerations. Successful etching processes in hot-wall CVD reactors were reported to operate at temperatures between 1500 and 1600 ºC for off-axis 4H-SiC and above 1600 ºC for off-axis 6H-SiC, with a pressure of 760 Torr, and an etching time between 10 and 80 minutes [62, 64]. The higher etching temperatures needed for 6H-SiC may be explained by the different growth conditions adopted for the two polytypes. The CVD reactor used in our etching processes presents a peculiar tapering of the susceptor, which has been designed to avoid the preferential consumption of growth precursors at the susceptor entrance and to maintain a constant gas concentration throughout the whole growth-zone by increasing the velocity of the gases along the flow direction [83]. As a result, the higher gas flow generates, for

the same etching parameters, a more effective etching. Hence, we chose etching temperatures of 1400 ºC for 4H-SiC and of 1550 ºC for 6H-SiC, while the pressure was fixed at 760 Torr, the H-flow at 10 SLM, and the etching time at 30 min for both processes.

As pointed out at the beginning of this section, the CVD reactor used for etching hexagonal SiC was mostly a 'growth-dedicated' reactor. In order to prevent the formation of the typical defects (e.g., Si-droplets, particulate deposition, undulate surface patterns) usually found in the crystal surface after etching with a 'growth-dedicated' CVD reactor, clean susceptor and poly-crystalline SiC sample support plates (e.g., not exposed to growth) were used. However, the graphite foam used in these experiments was also used in the past for growth experiments, increasing the risk of particle contamination which can nucleate triangular surface defects during etching. The presence of residual growth precursors in the reactor can in fact interfere with the initial stage of etching causing an initial localized growth at some areas on the substrate either due to the incomplete deposition of species or to localized etching of the surface. Initial localized growth can then result in triangular (or 'undulate') patterns on the surface as reported in [62]. For these reasons, the precaution of baking the CVD reactor in hydrogen with all its etching components was taken. The baking was performed for 1 hour at atmospheric pressure and 1400 ºC before each 4H/6H etching experiment.

2.3.2. Surface morphology: AFM

The 4H off-axis samples which underwent the H-etching process presented different initial morphological features: half, chemo-mechanical polished by Novasic, displayed during AFM analysis an extremely flat surface but no atomic steps (Fig. 2.8(b)) while the remaining presented typical polishing scratches (Fig. 2.8(a)).

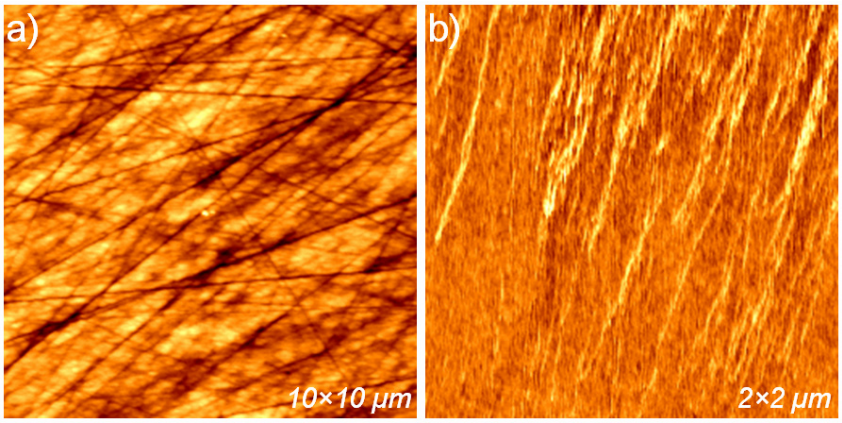

Figure 2.8. AFM micrographs of 4H-SiC(0001) before H-etching. (a) typical polishing scratches on the 'regularly' polished surfaces; (b) flat surfaces of the chemo-mechanical polished samples. Note the smaller scale in (b) helps to visualize the absence of atomic steps. As a reference, the deepest scratches in (a) are 20 nm deep. AFM micrographs taken in tapping mode.

After etching, both sets of samples presented atomically flat surfaces with terraces 50-100 nm in width and steps half a unit cell in height (5 Å) (Fig. 2.9). The steps were aligned along the $[1\bar{1}00]$ direction while unit cell steps were seldom observed.

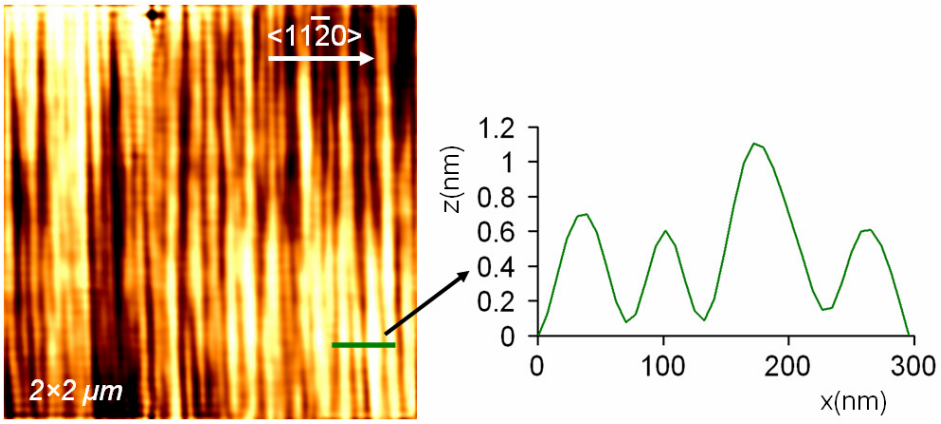

Figure 2.9. AFM micrograph and extracted line profile showing the presence of atomic steps on the surface of H-etched 4H-SiC(0001) surfaces.
Etch parameters were: T = 1400 °C, H_f = 10 SLM, p = 760 Torr and t_{etch} = 30 min. AFM micrographs taken in contact mode.

On the other hand, the on-axis 4H-SiC samples, which before etching presented a morphology like the one depicted in Fig. 2.8 (a), presented much wider atomic terraces after being etched with the same process used for the off-axis surfaces. This result is in total agreement with what has been reported in the literature [62]. The terraces observed for the on-axis surfaces were 1 μm wide, while the steps had unit cell height (Fig. 2.10). Also in this case the steps were aligned along the [1$\bar{1}$00] direction. In Fig. 2.10 it is evident the presence of triangular peninsulas protruding from the steps onto the terraces below them. Their height was assessed to be half a unit cell via AFM. These peninsulas are explained in [63] in terms of "fast-etch" and "slow-etch" directions. We suggest that they may be an indication of a slight over-etching of the 4H-SiC on-axis surfaces.

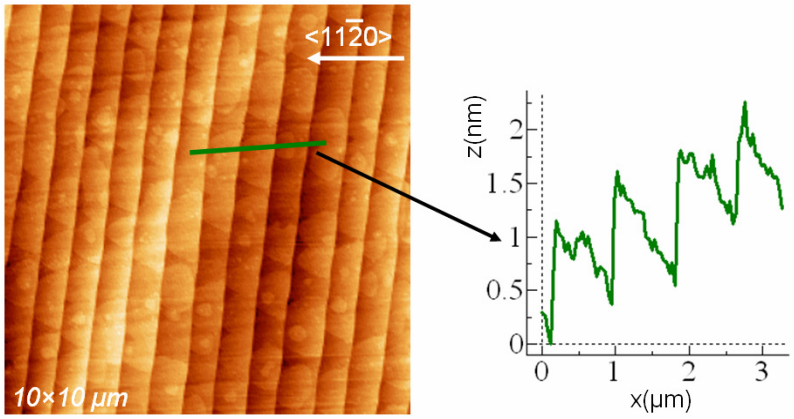

Figure 2.10. AFM micrograph of the surface morphology of on-axis 4H-SiC(0001) after H-etching. Relative line profile defines the step height to be 1 nm and the terrace width 1 μm. Note the presence of triangular peninsulas. Etch parameters were: T = 1400 °C, H_f = 10 SLM, p = 760 Torr and t_{etch} = 30 min. AFM micrographs taken in tapping mode.

Similarly to the 4H-SiC surfaces, both the on-axis and off-axis 6H-SiC(0001) surfaces displayed a morphology as the one reported in Fig. 2.8(a) before etching. After etching at 1550 ºC for 30 minutes both the off-axis and on-axis 6H-SiC(0001) presented atomic steps during AFM inspection. Also in this case, as for 4H-SiC, the steps were observed to be aligned along the [1$\bar{1}$00] direction and the ones on off-axis surfaces were much narrower than the ones for on-axis crystals, as expected. A typical AFM micrograph of the atomically flat surfaces obtained after etching off-axis 6H-SiC samples is reported in Fig. 2.11. The extracted line profile indicates that the steps are between 5 and 7.5 Å high and the terraces are 40-80 nm wide. These values are comparable to those reported in [59, 64] for off-axis 6H-SiC surfaces. Since one unit cell of 6H-SiC is 15.12 Å high in the direction perpendicular to the (0001) plane, the steps observed after etching were most certainly half a unit cell high (7.5 Å). The 5 Å high steps observed in Fig. 2.11 are probably an underestimation of half a unit cell steps due to the difficulty to resolve with precision the height of narrow terraces with the software analysis program used.

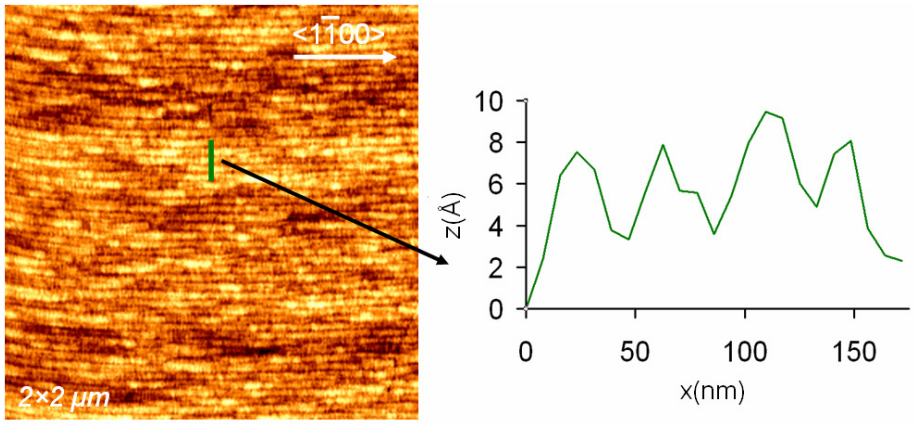

Figure 2.11. Morphology and line profile of H-etched off-axis 6H-SiC(0001) surfaces. Etch parameters were: T = 1550 °C, H_f = 10 SLM, p = 760 Torr and t_{etch} = 30 min. AFM micrograph taken in contact mode.

The typical morphology observed for H-etched on-axis 6H-SiC(0001) samples is reported in Fig. 2.12. As is evident, the steps are half a unit cell high and terraces are 150 nm wide. The same values have been reported by Owman [64] for H-etched on-axis 6H-SiC(0001) surfaces. The two particles observed in Fig. 2.12 are probably caused by the 'growth-dedicated' carbon insulating foam used during the etching process to support the clean graphite susceptor. It has to be mentioned that particulate is often found on the surface of samples etched with the CVD reactor described in this section even after baking of the system. This finding strongly confirms the need of an 'etch-process dedicated' foam insert for the aforementioned CVD reactor.

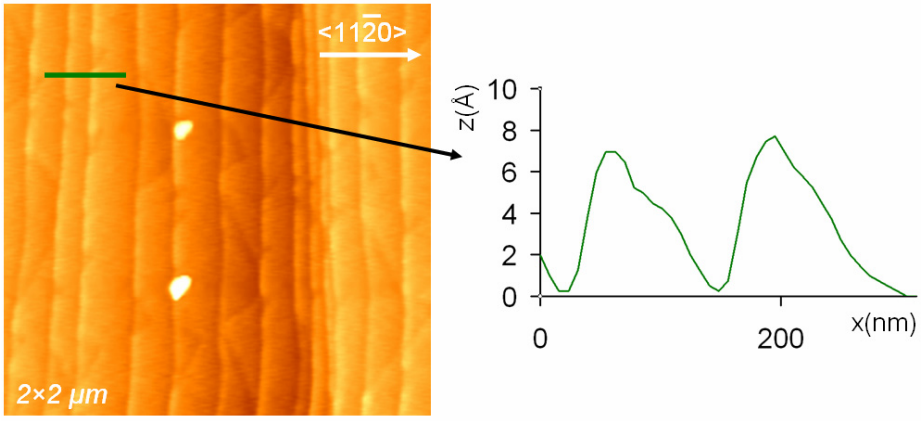

Figure 2.12. AFM micrograph and line profile showing the atomically flat on-axis 6H-SiC(0001) surfaces obtained after H-etching. The presence of particulate is due to the use of a 'growth-dedicated' foam in the CVD reactor. Etch parameters were: T = 1550 °C, H_f = 10 SLM, p = 760 Torr and t_{etch} = 30 min. AFM micrograph taken in tapping mode.

2.4. Summary

As discussed in Chapter 1, SiC is a promising candidate for biotechnological applications. A successful implementation of these applications puts specific demands on the quality and surface properties of SiC. In particular the CPD measurements proposed later in this work, which may help uncover cell-semiconductor electronic interactions, require well-ordered, chemically passivated and fully characterized surfaces. For this reason, this chapter reports on the control and understanding of the major polytypes of SiC via H-etching and surface characterization techniques. H-etching is shown to be a successful technique able to produce atomically flat and repeatable SiC surfaces. Exciting possibilities such as functionalization and nano-patterning of SiC surfaces with bio-molecules become more feasible thanks to the morphological atomic order revealed by H-etching treatment. Also, for those applications which require a direct interface between the biological cell and the semiconducting material, as the CPD measurements described

in this work, a comprehensive chemical and crystallographic characterization of the semiconducting surface, as reported in § 2.2.3, becomes of primary importance. In conclusion, the preparation and complete characterization of atomically ordered SiC surfaces may lead to the successful implementation of a large variety of biotechnological applications and, in particular, of the CPD studies proposed in this work and presented later in Chapters 4 and 5.

Chapter 3. SiC Biocompatibility Studies

In Chapter 2 we have discussed how suitable surface preparation and accurate surface characterization are of fundamental importance for semiconducting materials used in bio-sensing applications. However, besides properties such as low surface roughness and surface state densities there is another requirement that a semiconductor that is going to interface cells needs to fulfill: biocompatibility.

As we already mentioned in Chapter 1, despite the promising potentiality for bio-sensing applications, no studies are found in the literature which investigate crystalline SiC biocompatibility. In this chapter, we study single-crystal SiC biocompatibility by culturing mammalian cells directly on SiC substrates and by evaluating the resulting cell adhesion quality and proliferation. We also compare SiC biocompatibility to the one of the leading crystalline semiconductor in biotechnology, Si, whose cytotoxicity has been reported by several studies [84-86]. Nonetheless, Si continues to be widely used because of the ease of electronic integration with biological systems (e.g., arrays for retina implant, micro resonator probes for cortical recording, etc.). The results of this biocompatibility study show that crystalline SiC is indeed a very promising material for bio-applications, with better bio-performance than crystalline Si. This result opens up exciting perspectives for the use of SiC for bio-technological applications. In particular 3C-SiC, which can be directly grown on Si substrates, appears to be an especially promising bio-material: the Si substrate used for the epi-growth would in fact allow for

cost-effective and straightforward electronic integration, while the SiC surface would constitute a more biocompatible and versatile interface between the electronic and biological world. Also, the excellent capability of SiC in directly interfacing with biological cells without the need of any surface functionalization is of primary importance for the successful implementation of the CPD measurements proposed later in this work and an optimum starting point for the investigation of cell-semiconductor electronic interactions. Since a material's biocompatibility is influenced by chemical, morphological and electrostatic factors we also explore, in this chapter, the effect that different surface chemistries, morphologies and wettabilities have on cell adhesion and proliferation. The importance of using an appropriate cleaning procedure for the SiC samples before their use as substrates for cell cultures is also discussed.

3.1. Cell culture on 3C-, 4H-, 6H-SiC surfaces

A reliable and relatively easy way to define a material's cytotoxic level, biostability, possible bioactivity and overall biocompatibility is by culturing cells directly on it while monitoring the cell adhesion quality and proliferation. In this section we evaluate the biocompatibility of different SiC polytypes by culturing three lines of mammalian cells directly on 3C-, 4H and 6H-SiC surfaces and by using MTT [3-(4,5-dimethylthiazol-2-yl)-2,5-diphenyltetrazolium bromide] assays and optical imaging to monitor cell proliferation and adhesion quality, respectively. In § 3.1.1 we describe sample characteristics and cleaning prior to cell seeding. Section 3.1.2 reports on the experimental procedure adopted for culturing cells and evaluating the material biocompatibility while § 3.1.3 discusses the MTT assay and fluorescent microscopy results. Additional studies investigating differences in cell adhesion morphology for Si

and SiC samples were performed via optical microscopy and atomic force microscopy (AFM) and are discussed in § 3.1.4.

3.1.1. Sample characteristics and cleaning

The samples used as substrates for cell culture were as follows: three 3C-SiC(001) epilayers grown on Si(001) in the CVD reactor described in § 2.2; three 4H-SiC(0001) off-axis bulk crystals H-etched with the process reported in § 2.3.1 and originally purchased from Cree, Inc.; three 6H-SiC(0001) bulk crystals and Si(001) bulk crystals also purchased from Cree, Inc. All samples were diced to have a dimension of 8x10 mm. The doping was n-type for all the samples and in the range of: 10^{15} atoms/cm^3 for 3C-SiC; 10^{18} atoms/cm^3 for 4H-SiC; and 10^{19} atoms/cm^3 for 6H-SiC and Si. The surface characteristics of the 3C-SiC epilayers were those of the as-grown samples described in § 2.2.1. The 4H- and the 6H-SiC samples presented surfaces as described in § 2.3.1 for etched 4H- and un-etched 6H-SiC samples, respectively. The morphologies of these surfaces are depicted in Fig. 3.1 while their root mean square roughness (R_q), measured via AFM for an area of 25 μm^2, are listed in Table 3.1.

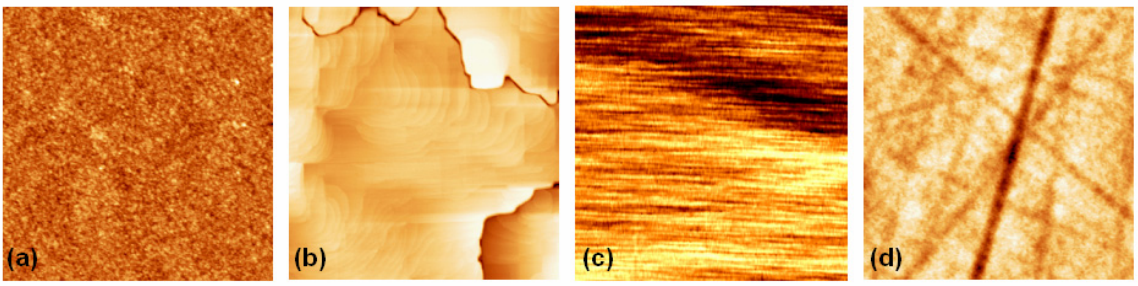

Figure 3.1. AFM micrographs of (a) Si, (b) 3C-SiC grown on (100)Si, (c) 4H-SiC and (d) 6H-SiC surfaces. All the micrographs are 2×2 μm in dimension. AFM data taken in tapping mode.

Table 3.1. Surface roughness of semiconductor surfaces used in the biocompatibility study. Surface roughness estimated from AFM measurements taken in tapping mode.

Substrate material	Si(001)	3C-SiC(001)	4H-SiC(0001)	6H-SiC(0001)
$\overline{R_q}$ (5×5 μm)	0.8 nm	1.4 nm	0.5 nm	1.2 nm

As is evident from Table 3.1, all the samples presented similar roughness values (0.5 nm < R_q (25 μm^2) < 1.4 nm) and, therefore, eventual differences in measured cell adhesion quality and proliferation cannot be explained in terms of differences in surface topology. Some minor experiments whose results are reported in the following sections also involved gallium arsenide (GaAs) and 4H- and 6H-SiC(000$\bar{1}$) (nominally C-face) samples. For reference, these samples presented surface roughness values comparable to the ones reported in Table 3.1 but since the majority of data presented here does not involve these samples they have not been included in the table to avoid confusion.

All the samples which were repeatedly used as substrates for cell culture were cleaned of any organic residue by immersion in a piranha solution (2:1 H_2SO_4:H_2O_2) for 5 minutes. After a rinse in de-ionized (DI) water, the surface oxide generated by the immersion in Piranha was removed by dipping the samples in a hydrofluoric acid solution (50:1 H_2O:HF) for 2 minutes. The samples were then thoroughly rinsed in DI water, dipped in ethanol, rinsed again and finally dried with dry nitrogen. All H_2O was deionized (DI) with a resistivity of at least 16 MΩ·cm.

3.1.2. Cell culture and experimental procedure

The mammalian cells used were as follows: 1) B16-F10 mouse melanoma cells (ATCC CRL6475); 2) BJ human fibroblasts (ATCC CRL2522) and 3) human

keratinocytes cells (HaCaT). The B16 and BJ cells were purchased from ATCC. Different media were used in the culture of the different cell lines: Eagle's Minimum Essential Medium (EMEM) supplemented with 10% fetal bovine serum (FBS) for the BJ cells; McCoy's Modified Medium supplemented with 10% FBS for the B16 cells; and Dulbecco's Modified Eagle's Medium (DMEM) supplemented with 10% FBS for the HaCaT. Prior to cell plating on the semiconductor surfaces, all the cells were cultured in 25 cm^2 culture flasks (Corning), incubated at 37 ºC in an air atmosphere containing 5% CO_2 and 95% relative humidity, and split and/or used at confluence.

Immediately before cell plating, three samples for each substrate material / polytype examined in the assay (e.g Si, 3C-, 4H- and 6H-SiC) were cleaned as described in the previous section and then placed in a 15.6 mm diameter cell culture well within a multi-well ultra-low cell-attachment plate (Corning). A schematic representation of the sample positioning in the multi-well plate is sketched in Fig. 3.2. Three empty wells, like the one represented in Fig.3.2. only belonging to a multi-well culturing plate (Corning), were used as controls for each MTT assay performed. It is evident that the plating areas are different for the semiconducting samples and the control wells. As a point of reference of the 200 mm^2 well area less than 2/5 were covered by the 80 mm^2 semiconductor samples. Therefore, the seeding density values were scaled accordingly for the plating area as described in [87]. Cells were seeded in the wells with the semiconducting samples at the following densities: $40x10^3$ cells/cm^2 for the BJ cells; $15x10^3$ cells/cm^2 for the B16 cells; and $20x10^3$ cells/cm^2 for the HaCaT. Obviously, separate experiments were conducted for the three different cell lines. After seeding, all the plated cells were incubated at 37 ºC for 1 to 8 days in an air atmosphere containing 5% CO_2 and 95% relative humidity.

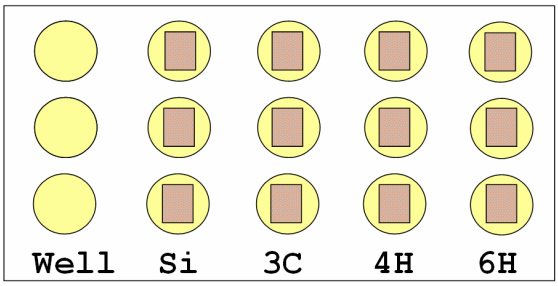

Figure 3.2. Schematic representation of the sample positioning in the multi-well plate for cell plating. A multi-well ultra-low cell-attachment plate was used during all experiments reported in this dissertation with a well area of 200 mm^2. Seeding was performed in triplicate to allow statistical analysis of the resulting cell viability and adhesion. A separate multi-well plate was seeded with cells and used as control. In the schematic all the seeded wells are drawn within the same multi-well plate for ease of representation.

Cell proliferation was typically evaluated on the third day via MTT assay. MTT assays were also performed on the first, second, fifth and eighth day to better investigate possible cytotoxic effects of the substrate materials used. In each MTT assay the media was reduced from the original value of 2 ml to 0.5 ml and 75 µl of MTT reagent were added to each well. After the yellow tetrazolium MTT reagent was completely converted into intracellular purple formazan by the metabolically active cells (required time ~ 2 hours), all the media was removed from each well and the semiconducting substrates were transferred to new wells. In order to solubilize the formazan, 0.3 ml of dimethyl sulfoxide (DMSO) were added to each well and the absorbance of the solutions was determined spectrophotometrically with a plate reader (Bio Kinetics Microplate Reader EL 340, Bio-Tek Instruments) operating at a wavelength of 595 nm. Readings were corrected for the formazan formation due to the semiconducting surfaces alone. It should be pointed out that all the numeric values reported in the text above are for the wells containing semiconducting samples; values for the control wells were appropriately

scaled. The MTT assays were repeated three times for all the cell lines and, as explained above, performed in triplicate for the controls and for each different substrate. The obtained results are reported in the next section as sampling distribution of the mean ($\bar{x}$) ± standard error of the mean (σ_m) and normalized with respect to the control readings.

The adherent cell morphology was studied using fluorescence microscopy. Semiconducting samples and control wells were plated as described above and the cell morphology was inspected after 4, 24, 48, 72, 96, 120 and 216 hours (the latter only for BJ and HaCaT cells). Two hours before the optical inspection was performed using a Leica DM IL inverted microscope, the cells were fluorescently labeled with 2 μL of CMFDA (5-chloromethylfluorescein diacetate) cell tracker dye.

3.1.3. SiC superior biocompatibility: MTT and fluorescent microscopy results

MTT assays and fluorescent microscopy were used to evaluate the biocompatibility of the different SiC polytypes. Cell proliferation and adhesion quality of cells cultured on SiC surfaces were compared to the ones of cells cultured on control wells (which represent an ideal surface for cell growth). Adopting the same procedure, SiC biocompatibility was compared to that of Si, which is at present the leading crystalline semiconductor for biotechnological applications. The histogram in Fig. 3.3 reports the results of MTT assays performed on the third day for three different mammalian cell lines and clearly shows that SiC is, in all its phases, a high-quality surface for cell culture with significantly better performance than Si. No statistically significant differences were found among the cell proliferation on different SiC polytypes. An extremely satisfying proliferation was observed for BJ cells on SiC, in average the same obtained for the

culture-well readings. In this case, a slight bioactivity of the SiC substrate could even be hypothesized. The smaller difference in B16 cell proliferation observed between Si and SiC substrates can be easily justified by the cell line nature. B16 melanoma cells are in fact extremely aggressive cancer cells capable of indifferently adhering to substrates of diverse biocompatibility: therefore a reduced selectivity was expected.

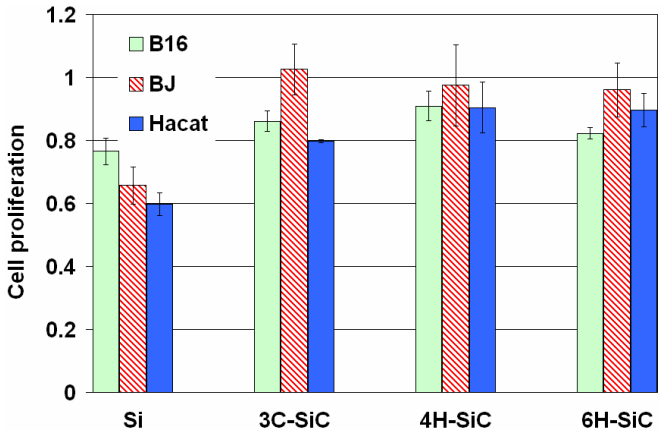

Figure 3.3. Cell proliferation of B16, BJ and HaCaT cells expressed as $\bar{x} \pm \sigma_m$ measured via MTT assays at the third day. Note that cell proliferation is greater on SiC than on Si surfaces for all the cell lines studied.

As mentioned in the previous section, MTT assays were also performed at the first, second, fifth and eighth day of culture. Cell seeding values for this particular set of assays were lower than the ones reported in § 3.1.2 to avoid cell confluence before the eighth day of culture. The results obtained for MTT assays performed on the first and eighth day of culture of HaCaT cells are reported in Fig. 3.4.

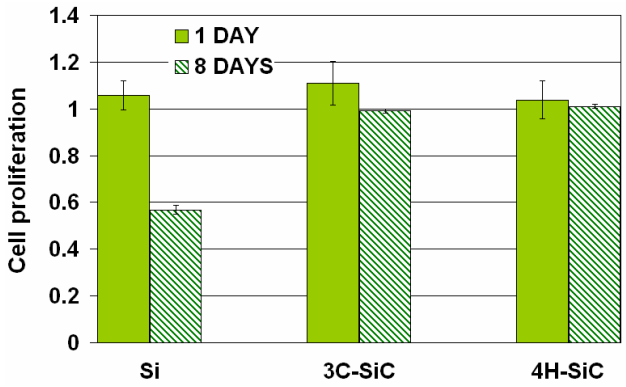

Figure 3.4. HaCaT cell proliferation on Si and SiC substrates measured via MTT at the first and eighth day of culture expressed as $\bar{x} \pm \sigma_m$. Note that cell proliferation is greater on SiC than on Si surfaces after eight days of culture.

The MTT readings were approximately the same for all the samples studied (Si, SiC, and control wells) after 24 hours from seeding. This result suggests that no preferential initial adhesion is observed on SiC samples compared to Si and that, apparently, all the seeded cells adhered to the semiconducting substrates. On the other hand, the cell proliferation at the eight day of culture was significantly lower on Si substrates than on SiC: calculations showed the reduction to be, with respect to SiC, as high as 56%. It should be noted that at the eighth day the cells reached confluence on the SiC substrates and control wells.

The optical inspection results obtained using fluorescence microscopy supported the MTT quantitative results while providing additional useful information regarding cell morphology and adhesion quality. Fluorescent microscopy revealed that all the seeded cells were well distributed on SiC surfaces after 4 hours of incubation, elongated and flattened against the surface after 24 hours, and confluent (for the seeding density reported in § 3.1.2) after 4 days (B16 and HaCaT), and 5 days (BJ). On the other hand, a lower density and generally inferior morphology were observed for cells cultured on Si

substrates. Fluorescence microscopy images of adherent cells on Si and SiC substrates at the third day of culture are reported in Figures 3.5 and 3.6 at lower and higher magnification, respectively.

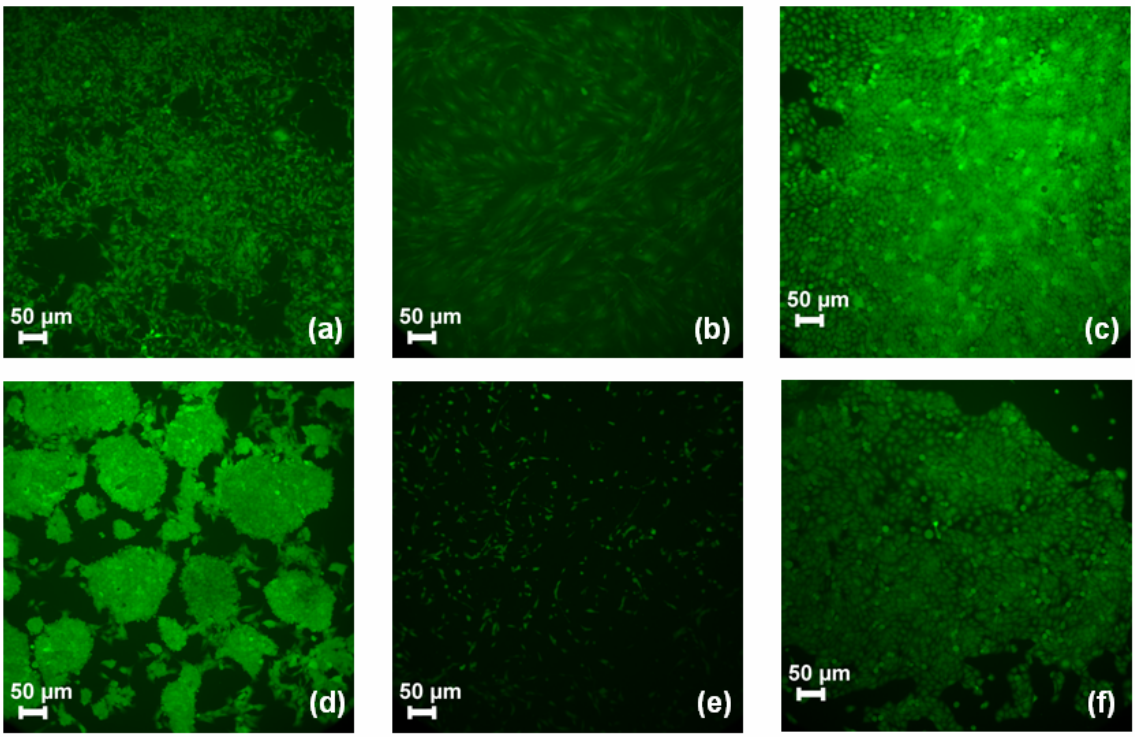

Figure 3.5. Morphology of B16 ((a), (d)), BJ ((b), (e)) and HaCaT ((c), (f)) cells at the third day of culture on SiC and Si substrates, respectively. Images by flourescence microscopy [88].

As is evident from images (a), (b), and (c) in Figures 3.5 and 3.6, cells on SiC substrates were well-distributed and flattened (the maximization of the contact area with the substrate is always an indicator of good biocompatibility) at the third day of culture. Moreover, their morphology was found to be identical to that of the cells in the control wells: stellate for B16, elongated for BJ fibroblasts and cuboidal for HaCaT cells. Even when imaged on the fifth or eighth day of culture (in experiments with lower cell seeding density), all the cells cultured on SiC substrates displayed an excellent morphology. This

finding, together with the fact that the cells could be cultured to confluence on all the SiC samples, confirms the lack of cytotoxicity of SiC substrates at least within the first eight days of culture.

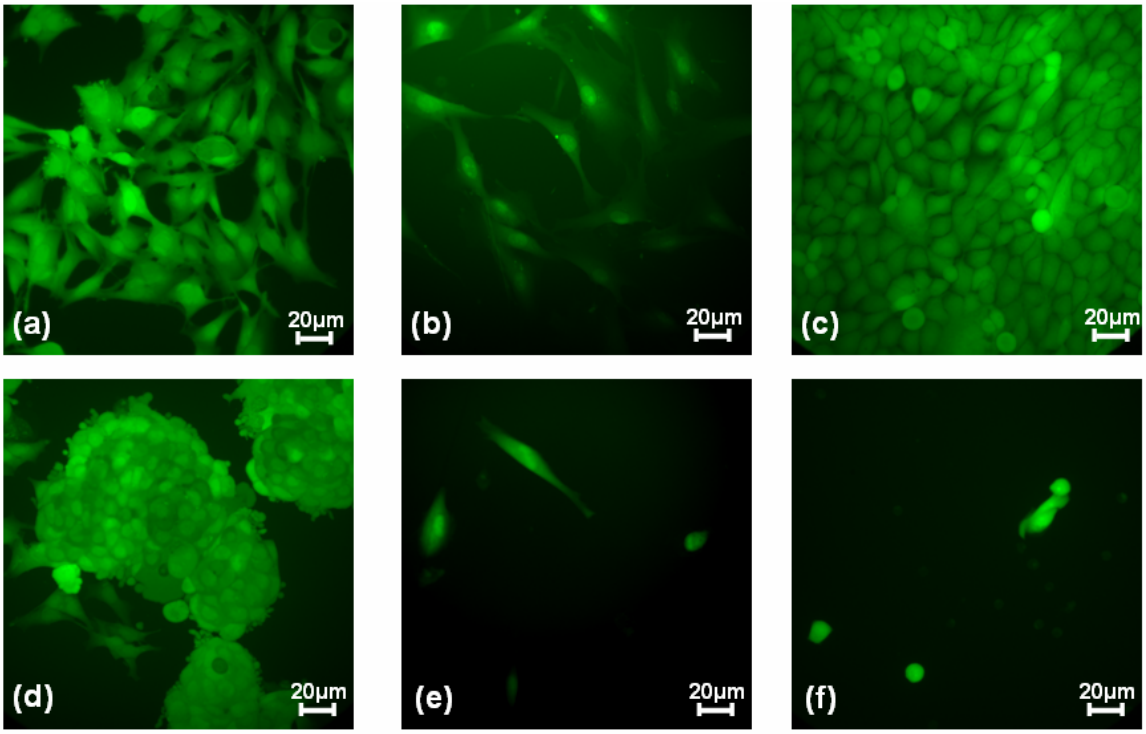

Figure 3.6. Higher magnification images of the morphology of B16 ((a), (d)), BJ ((b), (e)) and HaCaT ((c), (f)) cells at the third day of culture on SiC and Si substrates, respectively. Images by flourescence microscopy.

On the other hand, the morphology of the cells cultured on Si substrates appeared to be inferior: typically a reduction in the cell dimension was observed for all three cell lines. The reduced contact area of the adherent cells (low adhesion force) confirms the lower biocompatibility of the Si substrates. Specifically, B16 cells appeared rounded with a tendency to form clusters when cultured on Si (image (d) in Figures 3.5, 6). HaCaT and BJ cells were, at least during the first three days of culture, morphologically similar to the control cells but smaller and of a lower density (images (f) and (e) in Figures 3.5, 6). In

particular, the morphology of BJ cells cultured on Si degenerated at the fifth day of culture (Fig. 3.7(b)), while high-quality cell morphology was observed on all of the SiC surfaces (Fig. 3.7(a)). The observed morphological degeneration on Si surfaces was most probably caused by a not-null level of cytotoxicity of the Si substrates.

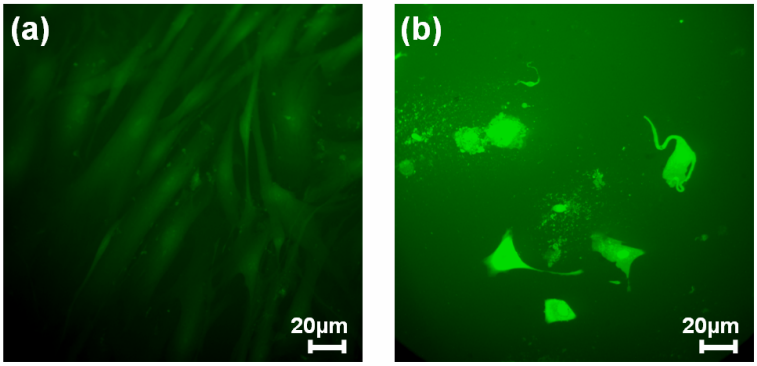

Figure 3.7. Cell morphology of BJ fibroblasts at the fifth day of culture on a (a) SiC and (b) Si substrates as measured with flourescence microscopy. Clearly the optimal morphology was observed on SiC substrates due to the uniform distribution and elongate shape of the adherent cells.

Another semiconducting material whose cytotoxic effect is well known is gallium arsenide (GaAs) [89, 90]. Since its deleterious effects on cells are well-known, we used it as a negative control to demonstrate the validity of our measurements. MTT assays were performed on GaAs and 6H-SiC samples after two days of B16 cell culture and the obtained results, reported in Fig. 3.8, clearly show the toxicity of this substrate material while again confirming the superior performances of SiC.

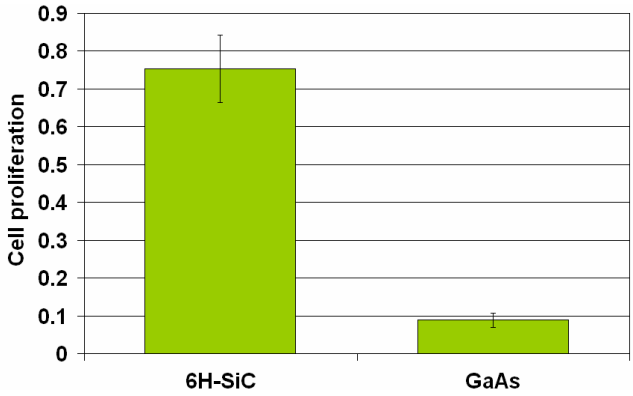

Figure 3.8. B16 cell proliferation measured via MTT at the second day of culture on 6H-SiC and GaAs substrates and expressed as $\bar{x} \pm \sigma_m$. Note that cell proliferation is greater on SiC than on GaAs which is known to be cytotoxic (GaAs used as a negative control in this experiment).

The fact that even the aggressive B16 melanoma cells did not proliferate and stay viable when cultured on GaAs substrates confirmed the high toxicity of this material and the validity of the procedure used to assess the biocompatibility of SiC and Si. Fluorescent images of cells cultured on GaAs substrates showed a morphological degeneration of the cells (see Fig. 3.9(b)). Like in the case of Si, cytotoxicity provokes cytostructural changes and eventually leads to cell death.

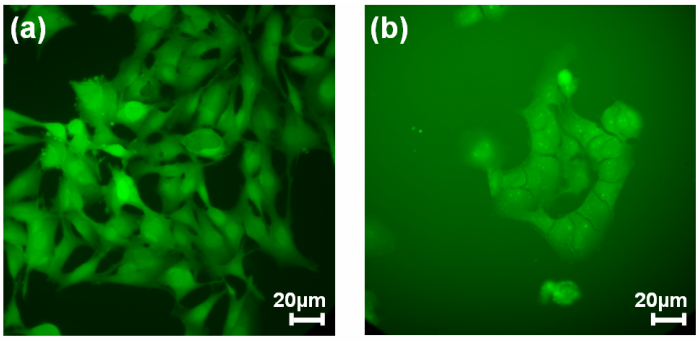

Figure 3.9. Morphology of healthy B16 cells cultured on 6H-SiC (a) vs. cytostructural degeneration of B16 cells cultured on GaAs as measured with fluorescence microscopy.

In conclusion, the MTT and fluorescence microscopy results show the superiority of SiC as a bio-surface for cell-culture while confirming a not-null level of cytotoxicity for Si. Also, the fact that different SiC polytypes, which display different band gaps and different doping levels (i.e., free charge density), performed in a similar way as substrates for cell culture suggests that the influence of the electronic properties of the material on cell adhesion and proliferation is not relevant in this case (at least for the SiC material system). However in Chapter 4 we will discuss more carefully the electronic interface between cells and semiconductor surfaces and final judgment of the influence of material electronic properties on cell viability should be reserved till then.

3.1.4. SiC vs. Si: evaluation of cell protrusions via AFM and optical microscopy

Additional studies were performed on cells cultured on SiC and Si surfaces using AFM and optical microscopy to quantitatively describe the presence of any cell extensions such as filopodia and lamellipodia. Lamellipodia are broad flat cell protrusions which surge forward and adhere to surfaces, allowing cells to gain traction and move on surfaces. Filopodia are rod-like cell surface projections extending several micrometers ahead of the cells where they explore the extracellular surface. The presence and extension of filopodia and lamellipodia indicate the quality of the cell response to a substrate material. Typically, numerous and extended filopodia and lamellipodia are indicative of good substrate biocompatibility. Therefore their measurement and quantification is an additional way to assess a material's degree of biocompatibility.

For these experiments B16 melanoma cells were seeded at a density of $40x10^3$ cells/cm^2 on 6H-SiC(0001) and Si(001) samples as described in § 3.1.2. After 24 hours the cells were fixed in 4% PFA (Paraformaldehyde) for 20 minutes at room temperature

(RT) and successively in a series of ethanol solutions with increasing concentration (17%, 35%, 70%, and 95%) for 2 minutes each. After the fixation, platinum-gold was sputtered on the cell / surfaces in a gold deposition chamber as is typically done to prepare cells for scanning electron microscopy (SEM) analysis. The cells were then imaged using the XE-100 AFM system and its resident optical microscope at the PSIA facility in Santa Clara (CA).

The optical inspection revealed, confirming what was described in § 3.1.3, a greater cell spreading and proliferation on the SiC substrates. Cells on SiC appeared to be stellate in shape and interconnected through a bridging network (Fig. 3.10(a)). Cell bridges were found to be typically 5-10 μm wide and 500 nm high (Fig. 3.10(b)). Typically, cells appeared to have reduced dimensions on Si substrates (as evident by comparison between Figures 3.10(c) and (e)). In general, extended lamellipodia, which indicate the formation of stable adhesion contacts, were observed on SiC surfaces (Fig. 3.10(d)). Instead, cells on Si had typically smaller or no lamellipodia present on their surfaces (Fig. 3.10(f)). Filipodia were present on cells cultured on both substrates and were typically 2-4 μm wide and 5-15 nm high as reported by the line profile in Fig. 3.10(f). Note that the two holes present in the cell in Fig. 3.10(f) are most likely nuclei in the mitotic phase which exploded during the gold sputtering process, which is done under vacuum. The missing nuclei allow one to see some beaded features 1 to 2 μm in diameter which are probably, because of their central location, fibrillar adhesions of the cells to the substrate.

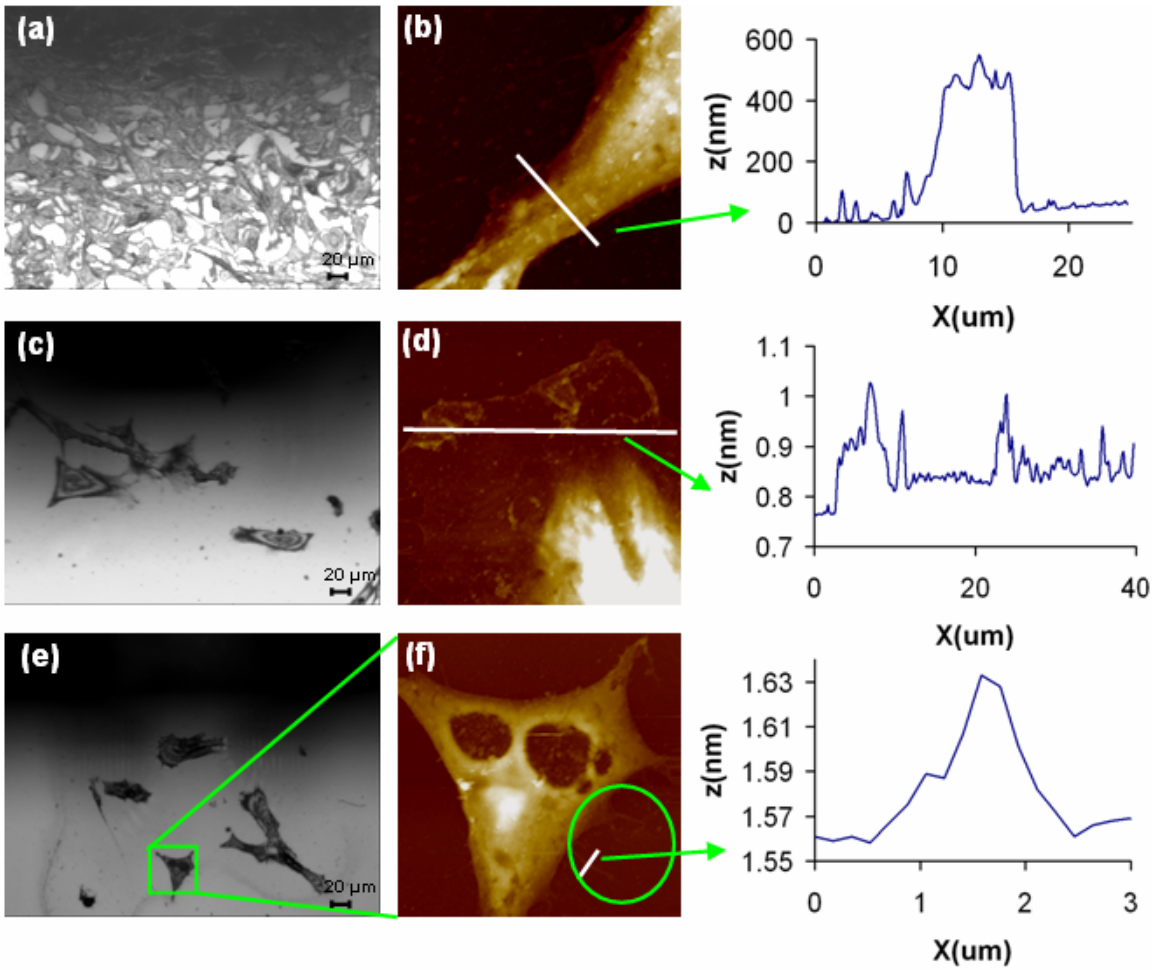

Figure 3.10. Optical (left) and AFM (right) micrographs of (a-d) B16 cells on SiC and (e, f) Si surfaces. In particular: (a) the observed bridging network of cells with (b) 'bridge' dimensions; cells presenting (c) extended lamellopodia on SiC and (d) single lamellopodia with relative dimensions; (e) cells presenting filopodia on Si and (f) a single cell with relative filopodia dimensions. AFM micrographs (b), (d) and (f) are 30×30 µm, 40×40 µm and 45×45 µm, respectively.

3.2. Influence of surface properties on cell adhesion and proliferation

The previous section reports an evident greater biocompatibility of SiC with respect to Si. In § 3.2.1 we search for the reasons at the basis of the observed greater biocompatibility by investigating the chemistry and the wettability of SiC and Si

substrates. Sections 3.2.2 and 3.2.3 focus on the effect that the topography and chemistry of SiC surfaces have on cell proliferation, respectively.

3.2.1. Surface chemistry and wettability as possible explanations of SiC greater biocompatibility

It has been already pointed out that the SiC and Si samples used in § 3.1 present similar topographical characteristics: therefore substrate topography can be excluded as a cause of the reported SiC superior biocompatibility with respect to Si. We identify three main remaining reasons that could be the basis of the enhanced cell proliferation observed on SiC substrates: 1) influence of the different surface chemistry on cell adhesion / proliferation; 2) differences between Si and SiC surface wettability. 3) reduced electronic interaction (e.g., charge exchange) between cell adhesion proteins and SiC surfaces (SiC has a larger energy bandgap, E_g, than Si and therefore a lower density of unoccupied states in the energy range of the transfer level, i.e. $E_g > 1.8$ eV [30]). Since (3) is a rather complicated issue which may find an answer only after the electronic interaction between semiconducting substrates and biological cells will be exhaustively understood (and therefore goes beyond the purpose of this work), we investigate (1) and (2) here with preliminary studies pertaining to (3) presented in Chapter 4.

For this purpose, XPS and contact angle studies were performed on the same Si and SiC surfaces used in the MTT assay described in § 3.1.3 after they were cleaned as described in § 3.1.1. Representative XPS surveys of as-introduced Si and SiC samples are shown in Fig. 3.11.

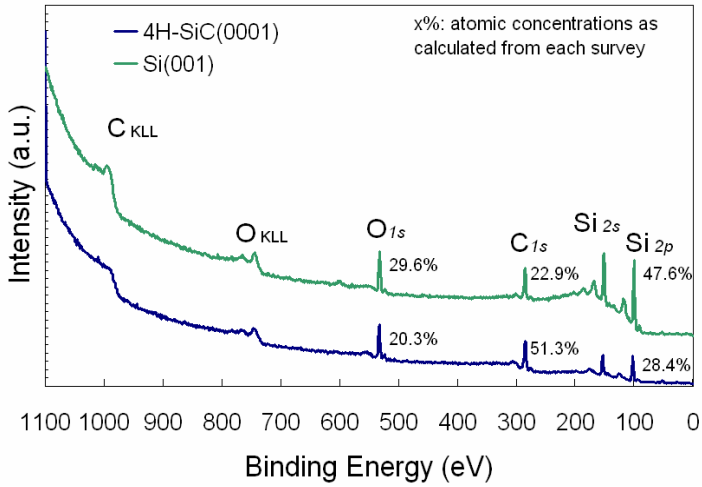

Figure 3.11. XPS surveys of two of the Si and SiC samples used in § 3.1.3. No comparison has to be made between the peak magnitudes of the two samples; only elemental percents within an individual sample are significant. Note the expected greater C-concentration on the SiC surface.

From the chemical analysis of the near surface region it appears that both Si and SiC present the same elements at the surface, namely Si, C, and O. However, the (graphitic) carbon present on Si is in lower concentration (typically < 25%) than the carbon on SiC (typically > 50%). The higher C-concentration on SiC surfaces is a likely explanation for the greater biocompatibility of SiC. It is in fact well-known that surfaces with a normal electrochemical potential close to the one of the cells are more biocompatible [11]. Since the electrochemical potential of carbon is comparable to that of living tissue, the higher carbon concentration of the SiC surfaces most likely justifies SiC greater biocompatibility.

Wettability of Si and SiC samples was evaluated using the sessile drop method at the IFN-CNR of Trento, IT [91]. A 1 μL droplet of DI water was deposited on the surface of each analyzed sample by using a biological pipette. The droplet contact angle (θ) was imaged using a contact angle goniometer and estimated by measuring the angles between

the baseline of the drop and the tangent at the drop boundary using the ImageJ 1.37v software. At least two droplets were deposited on different areas of each sample. The analysis of each droplet produced two contact angle values (e.g., left and right). Therefore the contact angle value was calculated for each sample as the mean of four values. Contact angle images for the SiC and Si samples analyzed are reported in Fig. 3.12. The contact angle values reported in Table 3.2 are expressed as the sampling distribution of the mean ($\bar{\theta}$) ± the standard error of the mean (σ_m) from a three samples distribution for each substrate material / polytype.

Figure 3.12. Measured water contact angles on Si, 3C-, 4H-, and 6H-SiC surfaces. Note the higher hydrophobicity of Si. In this experiment surface roughness does not influence the contact angle values since all the samples display similar values of R_q.

Table 3.2. Wettability of SiC and Si surfaces as measured via sessile drop method.

Substrate Material	Si(001)	3C-SiC(001)	4H-SiC(0001)	6H-SiC(0001)
$\bar{\theta}$ (º) ± σ (º)	88.28 ± 1.92	28.32 ± 2.27	20.27 ± 3.00	25.2 ± 2.13

From the images and the values reported we can infer that Si surfaces are considerably more hydrophobic than SiC surfaces. No relevant differences were found in the wettability level of the different SiC polytypes studied. As demonstrated by the tight standard deviation values, the surface wettability properties of the different samples used in the MTT assays in § 3.1 were similar for each substrate material / polytype. The high level of hydrophilicity exhibited by the SiC surfaces may also be a likely explanation for

its better performance as a substrate for cell culture. In fact, even though cell adhesion proteins adhere better to hydrophobic surfaces, mammalian cells are known to preferentially adhere to hydrophilic surfaces [92].

In conclusion, the lower biocompatibility of Si could be due to a competitive mechanism where both the electrochemical potential (e.g., absence of carbon from the surface) and the surface energy (e.g., higher hydrophobicity) play an important role. It has also to be pointed out that Si exhibits much poorer tribological properties than SiC, which means a higher density of debris formation. Cell phagocytosis of the toxic debris may likely lead to the cytostructural degeneracy reported for cells cultured on Si for more than 4 days (see Fig. 3.7).

3.2.2. Influence of SiC surface topography on cell adhesion and proliferation

Several studies report that surface roughness influences cell adhesion and migration. Typically, higher values of root mean square roughness yield higher osteoblast proliferation [93, 94], while flatter surfaces have been shown to enhance fibroblast proliferation and adhesion quality [95]. For this reason we investigated the influence that varying surface roughness of SiC may have on cell morphology and proliferation. For this purpose we selected SiC samples with different surface characteristics: three as-grown (Fig. 3.13(a)) and three over-etched (Fig. 3.13(b)) 3C-SiC samples whose surface features were exhaustively described in § 2.2.1. As a point of reference R_q was roughly 1.4 nm for a 25 μm^2 area of the as-grown samples and 35 nm for the same area of the over-etched samples. The substrates were cleaned as described in § 3.1.1, which excludes any possibility of H-termination due to the etching process on the over-etched surfaces. Both B16 melanoma cells and BJ fibroblasts were cultured on those substrates. MTT and

optical inspection were performed at the third day as described in § 3.1.2. The results of both analyses showed no difference in cell proliferation and adhesion quality on the two different sets of samples.

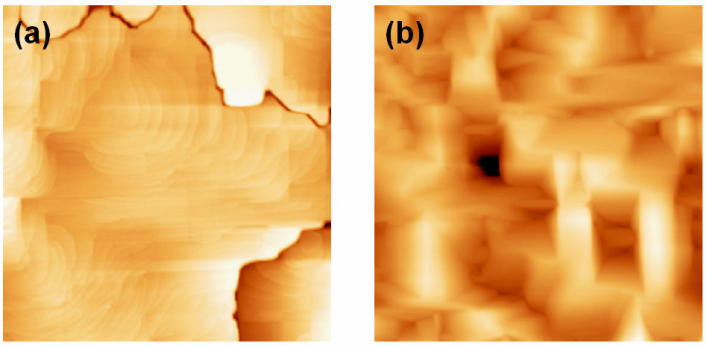

Figure 3.13. AFM micrographs showing the morphology of the 3C-SiC samples used to evaluate the effect of surface roughness on cell adhesion and proliferation. As-grown (a) and over-etched (b) 3C-SiC with R_q values of 1.4 nm and 35 nm, respectively. AFM data taken in tapping mode.

This result may be explained by the fact that the roughness variation between the two types of 3C-SiC surfaces studied was one to two orders of magnitude smaller than the cell adhesion plaques which are responsible for cell adhesion (34 nm of surface roughness variation against the 500-3200 nm of the adhesion complexes [96]). A study of Zhu *et al*. reports that patterned substrates need to have features ranging between 100 and 3000 nm in order to influence the plaque dynamic and therefore the cell adhesion pattern [96].

To verify this finding, BJ fibroblast cells were cultured on a 3C-SiC sample whose edge, after it was accidentally slivered, displayed macroterraces which were 2000 to 4000 nm wide. Optical inspection was performed after 24 hours and showed that the cells had spread in a patterned fashion within the slivered edge. The majority of the fibroblasts were well-spread and elongated along the macrosteps as shown in Fig. 3.14.

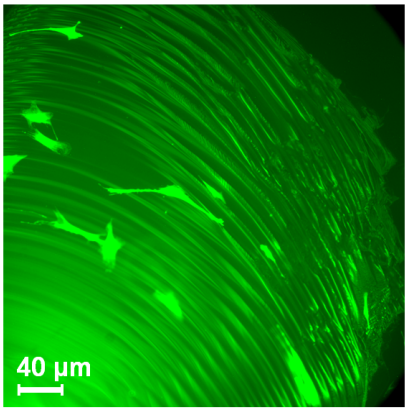

Figure 3.14. Patterned fibroblasts adhesion on the slivered edge of a 3C-SiC sample which displays macroterraces 2000 to 4000 nm wide. Image by fluorescence microscopy.

Summarizing, surface micropatterning seems to have a bigger effect on the morphology of fibroblast adhesion than surface nanopatterning. Variations of roughness in the nanometric scale seem to have little or no effect on the morphology and proliferation of B16 melanoma cells and BJ fibroblasts. This result is in agreement with what was reported by Richards [97]. Nonetheless, atomically flat surfaces like the ones produced via H-etching and described in Chapter 2, may be preferable to the commercially polished ones not only for biomolecular surface science studies but possibly also for implantable biosensors, since their smoothness reduces the chance of bacterial adhesion and therefore infection (e.g., common infectious bacteria diameter ~ 2µm).

3.2.3. Influence of SiC surface chemistry on cell adhesion and proliferation

Multiple studies have shown that the surface chemistry of biomaterials strongly influences cell adhesion and proliferation and may regulate the cellular behavior at the molecular level [98, 1, 18]. A previous work conducted on polyacrylamide surfaces has

shown a preferential adhesion of mammalian cells on hydroxylic group (-OH) and carboxylic acid (-COOH) terminations [99]. Curtis *et al*. report that hydroxylic groups considerably increase cell attachment on a large number of polymeric surfaces such as polypropylene and polystyrene [100]. We initially thought that H_2-etching of SiC samples may have terminated the surfaces in such a fashion. Since the AES studies reported in Chapter 2 were inadequate to detect hydrogen on the etched surfaces, we performed total attenuated reflectance Fourier transform infrared spectroscopy (ATR-FTIR) measurements, which we describe in Chapter 4, to probe whether –OH groups are present on H-etched 3C-SiC. Indeed, the ATR-FTIR results indicated the presence of C-H bonding at the surface while –OH groups where detected on regularly HF dipped surfaces. To probe whether the different surface terminations had an influence on cell proliferation we cultured HaCaT cells on H_2-etched and HF treated 3C-SiC samples and observed their behavior. Cell proliferation was evaluated through MTT assays while culture wells were used as controls. It has to be pointed out that both the H-etched and the HF treated samples were 8×10 mm diced from the same 2 inch wafer and therefore presented comparable surface characteristics. The etching was performed for 5 minutes at 1200 °C, at atmospheric pressure and with a hydrogen flow equal to 10 SLM in the CVD reactor described in § 2.2. H-etching did not produce any change of the surface morphology of the 3C-SiC samples while hydrogen was detected on the surface by ATR-FTIR analysis. The etched samples were not cleaned to preserve the H-termination while the un-etched samples were cleaned as described in § 3.1.1. The MTT assay was performed at the third day and in triplicate for the etched and HF treated 3C-SiC

substrates and the controls. The obtained results are reported in Fig. 3.15 and expressed as $\bar{x} \pm \sigma_m$.

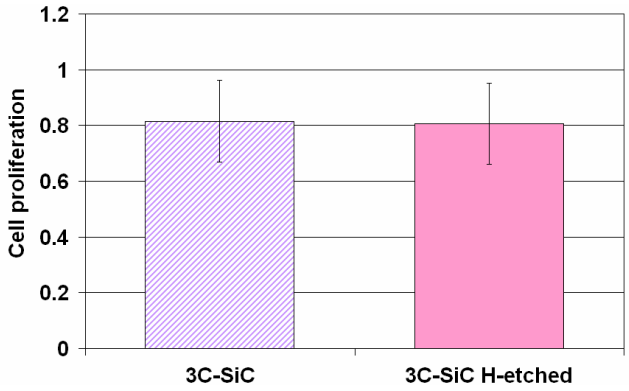

Figure 3.15. Comparison in HaCaT cell proliferation between etched and un-etched 3C-SiC substrates at the third day of culture expressed as $\bar{x} \pm \sigma_m$ measured via MTT assay. Note no difference in proliferation was observed despite the detection of hydrogen on the etched surface via ATR-FTIR.

As is evident from the histogram above, cells proliferated at the same rate on H-etched and un-etched 3C-SiC surfaces. Fluorescence microscopy confirmed this result which may be explained considering that the elapsed time between cell seeding and adhesion is roughly four hours and that during this time numerous chemical changes take place at the semiconductor surface. More probably the surface oxide layer, caused by the immersion in media, is formed before the cell attachment is finalized. At that point the un-etched and etched surfaces will present most likely similar chemical characteristics (i.e., any hydrogen effect on the surface is eliminated by the oxide).

We already discussed that a higher C-concentration on the SiC surfaces is a possible cause of the SiC greater biocompatibility and that, in general, a C-rich surface is believed to enhance cell adhesion. For this reason we decided to study the proliferation of HaCaT cells cultured on the C-face of SiC samples. In this experiment three 4H-

SiC(0001) and\ three 4H-SiC($000\bar{1}$) surfaces, nominally Si- and C-face, respectively, where used as substrates for cell culture after being cleaned as described in § 3.1.1. No differences in surface morphology were observed among the different samples. The MTT assay, performed at the third day of cell culture, showed a surprisingly reduced cell proliferation on the C-face samples (Fig. 3.16).

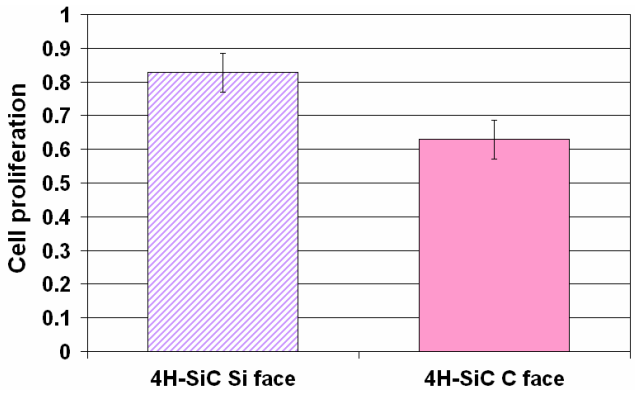

Figure 3.16. HaCaT cell proliferation at the third day on Si- and C-face 4H-SiC expressed as $\bar{x} \pm \sigma_m$ measured via MTT assay. Higher proliferation is observed on the Si-face.

However, light was shone on this puzzling result by XPS analysis performed on 4H-SiC(0001) and ($000\bar{1}$) substrates cut from the same wafer and cleaned at the same time as the samples used for the MTT assay. Surface elemental ratio values, as calculated from the surveys, are reported in the first three rows of Table 3.3. The percents of C and Si elemental concentration on the surfaces, reported on the last two rows, are calculated from the high resolution scans.

Table 3.3. Elemental concentrations and ratios for 4H-SiC(0001) and 4H-SiC($000\bar{1}$).

	4H-SiC(0001) Si face	4H-SiC($000\bar{1}$) C face
C/Si	1.62	1.71
O/Si	0.34	0.35
F/O	0.33	1.30
C % HR	60.05	63.14
Si % HR	39.95	36.86

While the values in Table 3.3 confirm the higher C-concentration of the C-face surfaces, the most striking result is the high concentration of fluorine (F) found on 4H-SiC($000\bar{1}$). It has to be noted that such a high concentration of F was never found on all the other SiC (always the Si-face was studied) surfaces examined in the past after being cleaned as in § 3.1.1. Low F concentrations were found rarely and were mostly caused by a shortened rinsing time after the HF dip. Since both fluorine and fluoride ions are toxic, a high F-concentration on the 4H-SiC($000\bar{1}$) is a likely explanation for the reduced cell proliferation observed on those surfaces. However, at this time it is unclear why the C-F bond should be more resistant to a DI water rinse than the Si-F bond. Fluorine is known as the most highly electronegative element on earth (e.g., 3.95 in the Pauling scale), and will therefore create stronger bonds with elements exhibiting a lower electronegativity. Si electronegativity is lower than that of C (1.90 versus 2.55 in the Pauling scale): therefore the silicon-fluorine bond, which presents an energy of 582 kJ mol^{-1}, is extremely stable and evidently stronger than the carbon-fluorine bond, whose energy is 452 kJ mol^{-1}. Therefore, a higher fluorine residue would not be expected on C-face samples after DI water rinse. However, Jacobsohn et al. [101] report that the incorporation of CF_n groups

on the surface of SiC make it much more hydrophobic while the presence of Si-F bonds doesn't change the material wettability. Therefore, the way the fluorine atoms are incorporated on the SiC surface may play an important role: the increased hydrophobicity on the C-face surfaces could likely reduce the effectiveness of the DI rinse step. Also, a lower fluorine concentration on Si faces immediately after HF exposure and prior to the DI rinse step could be another possible explanation for the reduced presence of fluorine in Si rather than in C faces. In fact, Si surfaces have been found to present mostly silicon hydride species and very little oxide or fluoride after HF treatment [102]: because of the high electronegativity of fluorine, Si-F bonds are prone to polarize Si atoms which may become much more susceptible to nucleophilic attack than Si-H bonds. In any case, the DI rinse step duration should be increased for 4H-SiC($000\bar{1}$).

3.3. Cleaning of SiC surfaces for bio-applications: RCA vs. Piranha

The previous section has drawn attention to the importance of choosing appropriate cleaning procedures when preparing surfaces for biological evaluation. In this section we compare the effectiveness of two standard cleaning procedures used to remove organic residue from SiC surfaces prior to cell growth: RCA (Radio Corporation of America) and Piranha cleaning. The efficacy of these two procedures was evaluated through optical and chemical analysis, and Piranha was shown to be the one capable of completely removing the organic contaminants (residue after cell exposure) and, therefore, best able to produce chemically reproducible surfaces. However, the ineffectiveness of RCA cleaning, which leaves bio-residue on the surface, may be useful for identifying the chemistry and shape

of the cell focal adhesions (§ 3.3.2). Thus in § 3.3.3 we report on the effects of repeated Piranha cleanings on surface chemistry and wettability, which affect cell proliferation.

3.3.1. Effect of RCA and Piranha cleans on semiconductor surface morphology and chemistry

A total of six 4H-SiC(0001) and four 3C-SiC(001) samples, all of them presenting atomically flat surfaces and constantly used as substrates for cell growth, were used to evaluate RCA and Piranha effectiveness in organic residue removal. The methodology adopted was the following: first, HaCaT cells were grown on the surfaces of those samples; second, half of the samples were cleaned with Piranha and half with RCA; last, their surface morphology and chemistry was evaluated. The Piranha procedure adopted was the one described in § 3.1.1. The steps of the RCA cleaning procedure were as follows: immersion in a 1:1:6 mixture of NH_4OH:H_2O_2:H_2O heated to 65 °C for 10 minutes; rinse with DI water; dip in a 50:1 H_2O:HF for 30 seconds; rinse in DI water; immersion in a 1:1:6 mixture of HCl:H_2O_2:H_2O heated to 65 °C for 10 minutes; rinse in DI water. The oxide generated by the oxidizing steps of RCA was removed and the samples were sterilized by using the same procedure adopted after Piranha clean and described in § 3.1.1. Which means, dip in hydrofluoric acid solution (50:1 H_2O:HF) for 2 minutes; thoroughly rinse in DI water; ethanol dip followed by DI water rinse; nitrogen dry.

The surface morphology of the samples was inspected using the optical camera of the XE-100S PSIA AFM system.

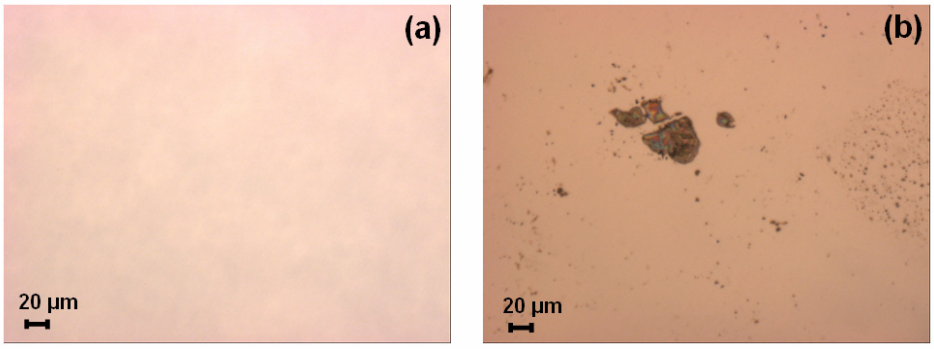

Figure 3.17. Optical images showing the surface morphology of 4H-SiC(0001) after cell growth and subsequent cleaning with (a) Piranha and (b) RCA cleans. Note the higher level of residue after RCA cleaning indicating that Piranha is superior in producing chemically repeatable surfaces.

Fig. 3.17(a) and Fig. 3.17(b) show the surface morphology of 4H-SiC(0001) cleaned with Piranha and with RCA, respectively. While the surface of the Piranha-cleaned sample appears completely spotless, the surface of the RCA-cleaned sample is heavily contaminated by organic residue. It surprisingly appears that even dead cells are present on the surface after RCA cleaning (see center of Fig 3.14(b)). Similar results were obtained for the 3C-SiC surfaces.

The surface chemistry of the samples was analyzed via XPS. XPS surveys and high resolution scans of the RCA cleaned samples displayed spectral lines whose kinetic energy was clearly associated to nitrogen (N) and sodium (Na) (Fig. 3.18), while elements other than C, Si and O were not detected in samples cleaned with Piranha. Since N is the key atom in the amines of the adhesion proteins, its presence indicates the existence of proteins on the surface.

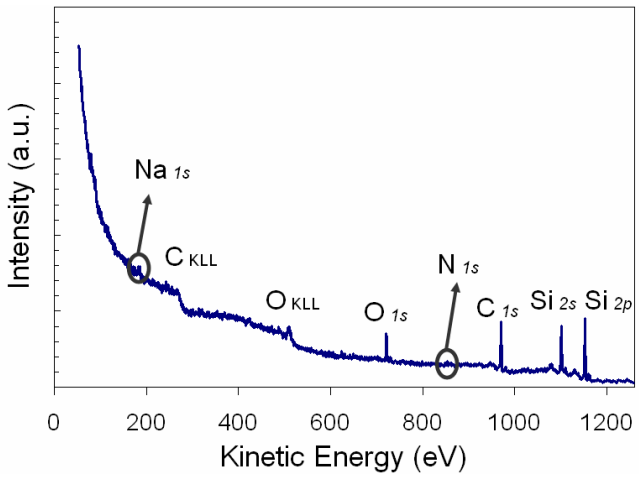

Figure 3.18. Presence of nitrogen (N) and sodium (Na) in the XPS survey of 3C-SiC(0001) after cell growth and subsequent RCA clean. These elements are indicators of residual biomatter on the surface and N, in particular, is a key component of adhesion proteins.

The reported results lead to the conclusion that Piranha clean is much more effective in removing organic residue than RCA clean. For this reason, Piranha solution was constantly used in the sample cleaning procedure prior to cell deposition (§ 3.1.2).

3.3.2. RCA clean as a promising surface pre-treatment for the study of cell-SiC adhesion sites

When an epithelial cell adheres to a surface three typical types of adhesions may take place: focal complexes, focal adhesions and fibrillar adhesions, which are characterized by different molecular constituents and dimensions. *In-vivo*, these adhesions exist between the cells and the extra-cellular-matrix (ECM), which is a fibrous mesh of proteins that serves as both structural scaffold and substrate for the display of signaling ligands. At present, many studies are focusing on rebuilding ECM surrogates in synthetic materials to engineer cell-surface interactions [96, 103, 104]. However, when cells come into contact with a substrate that naturally does not present ECM proteins,

they may or may not produce ECM depending on the substrate level of biocompatibility. Formation and secretion of ECM proteins, including fibronectin and type I collagen, are required for cell spreading and anchorage, so biocompatible material will enhance ECM production.

We used the presence of bio-residuals on the surface after RCA cleaning to study the nature of the HaCaT adhesion sites on SiC surfaces. The identification, by topographical exam, of the typology of adhesions could help identify the adhesion proteins that have an active role in SiC-HaCaT cells interaction.

Typical optical images of RCA-cleaned SiC surfaces were observed to be similar to the one of Fig. 3.19. Dead cells are present in the centre of the image, while dot-shaped particles, which are possible adhesion sites, are visible in the right hand side (RHS) of the figure. The height of the cell residue was measured to be 200-500 nm (Fig. 3.19(b)) by AFM. Also, elongated fibrillar elements, whose nature is explained further on in this section, were observed frequently (see upper LHS of Fig. 3.19(b)).

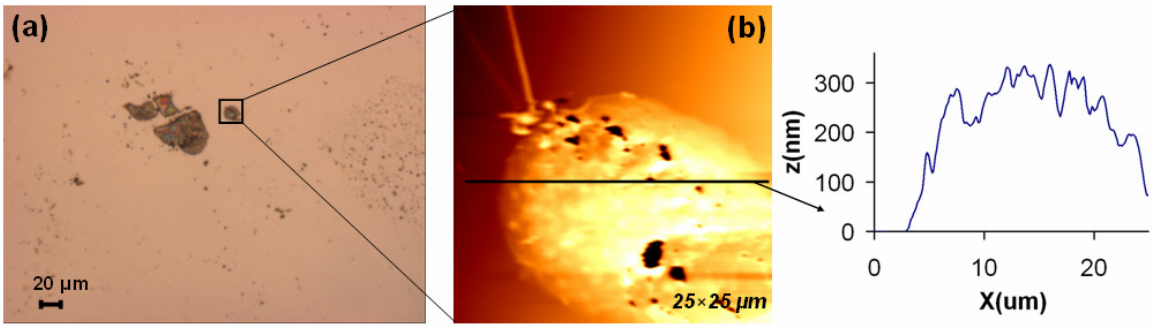

Figure 3.19. Analysis of RCA cleaned surface. (a) optical micrograph and (b) AFM micrograph of a cell observed in (a) with cell dimension shown via the relative line profile.

A better analysis of the dot-shaped features can be performed from Fig. 3.20(a) which probably represents (considering the scale bar and that the size of an extended HaCaT cell is ~ 20 µm) a site for multiple cell adhesion.

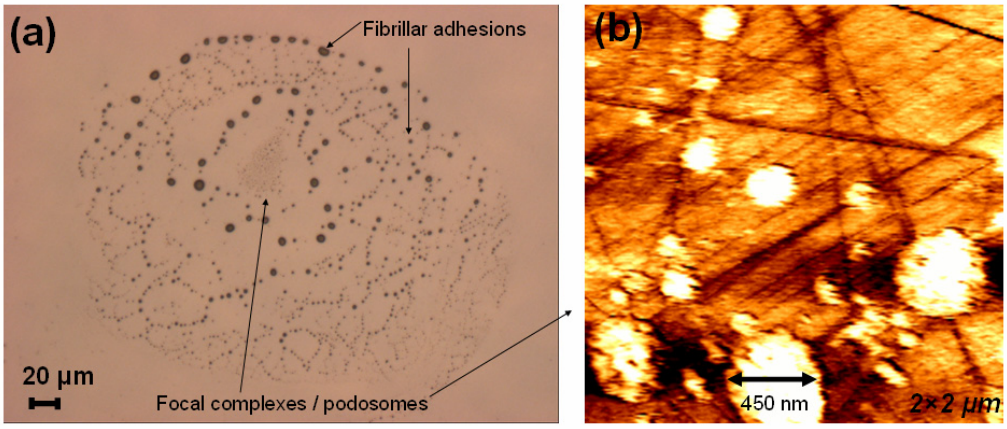

Figure 3.20. Analysis of different adhesion sites found on SiC surfaces after RCA clean. (a) optical micrograph and (b) AFM micrograph of a particular feature in (a) depicting what are believed to be podosomes on the surface.

We identified, by analyzing their dimensions, three different typologies of cell adhesions that may still be present on the SiC surface after RCA cleaning (see labeling in Fig. 3.20(a)). Fibrillar adhesions are beaded features of variable dimensions ranging from 1 to 10 µm. Smaller dot-like features are either focal complexes (~ 1 µm) or podosomes (<1 µm, Fig. 3.20(b)) [105, 106].

In many samples a fibrillar network like the one in Fig. 3.21 was observed. This suggests massive ECM production on SiC substrates, which also confirms the material's biocompatibility. In the ECM net were often observed circular shaped holes, which probably indicate the original presence of cells on those sites (see circle in Fig. 3.21(a)). In fact, if the ECM net-cell is a stronger bond than ECM net-SiC substrate, when the cell is detached by the chemical cleaning, the fibrillar net will also be removed. AFM

micrographs and related line profiles, like the ones in Fig. 3.21(b), reported the fibrillar elements to be up to 300 nm high and 0.5-1.5 µm wide.

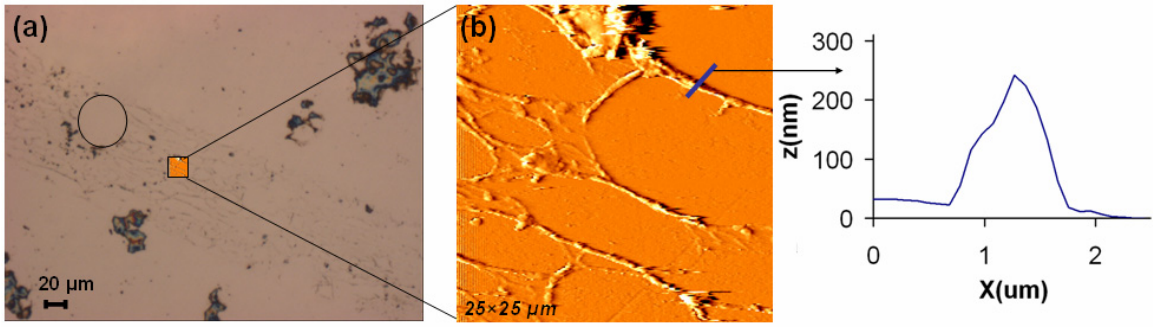

Figure 3.21. (a) Optical image and (b) AFM micrograph, with related line profile, showing a fibrillar network on the SiC surface after RCA cleaning. The circle in (a) indicates an area of missing fibers and therefore a possible cell site before RCA cleaning. Cellular residue are visible in the upper RHS and lower LHS of the optical image.

3.3.3. Effect of repeated Piranha cleanings on chemistry, wettability and cell proliferation

While performing the biocompatibility studies whose results are reported in § 3.1 and 3.2, we noticed that the cell proliferation was significantly lower on samples cleaned with Piranha several times (e.g., more than ten) than for samples cleaned only a few times. As a consequence, we decided to investigate if this difference in cell proliferation was caused by changes in surface properties induced by the Piranha clean chemistry. For this purpose, XPS studies and contact angle analysis were performed on a series of 3C-SiC(001) and 4H-SiC(0001) samples cleaned in Piranha from a minimum of zero to a maximum of twelve times. Fig. 3.22 reports the HaCaT cell proliferation on samples never treated with Piranha and treated ten times, respectively. The results, calculated from a series of three MTT assays, showed that the cell proliferation for samples never treated with Piranha was up to 23% higher than for the over-treated samples.

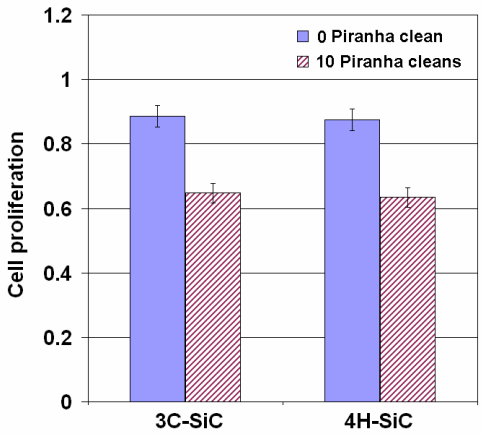

Figure 3.22. HaCaT cell proliferation at the third day on 3C- and 4H-SiC samples never cleaned with Piranha and cleaned with Piranha 10 times expressed as $\bar{x} \pm \sigma_m$ measured via MTT assay. [88]

Contact angle studies performed on the differently treated 3C- and 4H-SiC surfaces gave the results listed in Table 3.4.

Table 3.4. Piranha effect on surface wettability assessed by sessile drop method.

	# piranha treatments	3C-SiC(001)	4H-SiC(0001)
$\bar{\theta}$ (°) ± σ (°)	0	52.53 ± 1.83	53.78 ± 3.38
	3	35.2 ± 1.7	-
	>10	22.8 ± 2.1	20.65 ± 3.35

It appears that Piranha cleaning tends to increase the surface hydrophilicity. By comparing the results in Table 3.4 and Fig. 3.22, we can state that in this case, differently than in § 3.2.1, a higher hydrophilicity does not correspond to a greater cell proliferation. This apparently contradictory result (e.g., mammalian cells should preferentially adhere and proliferate on more hydrophilic surfaces) was explained by the results of XPS analysis. In Table 3.5 we report the data extracted from XPS survey and high resolution scans of 4H-SiC sample never treated with Piranha and treated 10 times.

Table 3.5. Si and C elemental concentration* and C/Si ratio** for 4H-SiC samples treated with Piranha zero and ten times.
* as calculated from the XPS high resolution scans
** as calculated from the XPS survey

	No Piranha	Piranha 10 times
C/Si **	1.62	1.56
C % *	60.05	56.28
Si % *	39.95	43.72

It must be noted that the 4H-SiC surfaces examined with XPS were of vicinal samples cut from the same two inch wafer and therefore presented similar chemical characteristics before the Piranha treatment. It is evident in Table 3.5 that repeated Piranha cleanings reduce the C-concentration on the near surface region in a sensitive way. This result suggests that, even though SiC is well-known to be chemically inert to the most widely used acids and liquid etchants, it is likely that repeated piranha cleans of SiC surfaces may decrease the carbon concentration in the near surface region. Piranha is, in fact, a strong oxidizer and highly effective in removing organic matter. Its extremely reactive atomic oxygen species, that form during H_2O_2 dehydration, allows the Piranha solution to dissolve elemental carbon, which is notoriously resistant to room temperature aqueous reactions. A decreased C-concentration in the Piranha over-treated surfaces is a likely explanation for the increased hydrophilicity observed on these surfaces. *Ab-initio* molecular dynamic simulations reported in [107] have, in fact, shown that carbon-terminated SiC surfaces have a hydrophobic character, while Si-terminated SiC surfaces are hydrophilic. Also, other sources report that a surface covered with a substantial amount of carbon bonded to oxygen is hydrophobic [13]. Therefore it is likely to assume

that a reduced C-concentration on the SiC surface may lead to a consequently increased hydrophilicity. Also, since surfaces richer in carbon are more biocompatible, the reduced C-concentration observed for Piranha over-treated samples is very likely the cause for the decreased cell proliferation reported in Fig. 3.22.

Summarizing, the repeated use of Piranha cleaning changes the SiC surface chemistry and subsequently its wettability and biocompatibilty. In order to obtain consistent results in biocompatibility studies the Piranha cleans of a specific sample have to be limited to a maximum of five. This particular precaution was used when performing all the MMT assays and optical inspections described in § 3.1.3.

3.4. Summary

The presented studies report the significant finding that SiC surfaces are a better substrate for mammalian cell culture than Si in terms of both cell adhesion and proliferation. In the past, the fact that cells could be directly cultured on Si crystalline substrates led to a widespread use of these materials for biosensing applications [108-110]. Therefore, the results reported in § 3.1 define SiC an even more promising substrate for future cell-semiconductor hybrid systems.

The main factors that have been shown to define SiC biocompatibility are its hydrophilicity and surface chemistry (§ 3.2.1). SiC surface morphology is shown to influence cell adhesion only when macropatterned (§ 3.2.2), while SiC polytypism and doping concentration seem to have no influence on cell proliferation (§ 3.2.3).

The importance of using an appropriate cleaning procedure to obtain repeatable and clean surfaces after each cell culture cycle is discussed in § 3.3.1 and in § 3.3.3. In § 3.3.2

we show how the finding that RCA cleaning leaves bio-residuals on the surface can be used to analyze the properties and morphology of the adhesion sites.

Many more analysis techniques may be used to analyze SiC biocompatibility. In particular, primary cell lines could be cultured on SiC surfaces in the future since their behavior would be a closer description of the *in-vivo* performance of the material. Also, since cell adhesion is known to be influenced by the electrostatic properties of the substrate in the specific media where cells are grown, zeta potential measurements of SiC particles in media could be attempted to define its charge. The adhesion sites of cells on SiC surfaces could be analyzed by using specific dies which would allow for a more accurate adhesion typology differentiation than the one presented in § 3.3.2. Once the adhesion sites are well characterized a more precise identification of the adhesion proteins would be possible using XPS and FTIR. The identification of the organic chemical groups that bind to the SiC surface, together with the calculation of SiC zeta potential in media, could be used to better understand the electronic interaction between cell and SiC surfaces.

Chapter 4. CPD Apparatus and Characterization of Surfaces for Cell-Semiconductor Electronic Interaction Studies

The surface characteristics and biocompatibility of silicon carbide (SiC) have been extensively studied in Chapters 2 and 3, respectively. Thanks to the knowledge acquired through these studies we can now move forward and characterize cell-semiconductor electronic interactions via contact potential difference (CPD) measurements. To date, dark/light CPD measurements have been proven to be a powerful technique which allows one to investigate the electronic band banding naturally present at the surface of a semiconductor or which occurs as a result of chemical or ionic charging [40, 42, 45]. The measurements that we aim to perform and that will be extensively described in Chapter 5 intend to investigate the band bending induced in a semiconductor by the charge associated with biological cells residing on the semiconductor surface. However, there is a potential complication that these measurements intrinsically present: the necessity of a liquid layer (i.e., culturing cell media) around the cells which implies immersion of the semiconductor in an electrolyte.

In order to perform successful CPD measurement of a semiconductor immersed in liquid, the CPD apparatus has to be carefully assembled and calibrated and the samples selected for the liquid measurements have to fulfill several requirements: (i) biocompatibility to allow cell adhesion during the experiment with adherent cells; (ii) low surface state density to impede pinning of the Fermi level in liquid; (iii) complete

electronic characterization in air via CPD. All the SiC surfaces fulfill requirement (i), as shown by Chapter 3, while we suggested in Chapter 2 that a low surface state density (ii) can be obtained on damaged SiC surfaces by processing them with suitable H-etching processes. In this chapter we therefore concentrate on requirement (iii).

After describing the CPD apparatus and its calibration, we present the experimental procedure designed to perform the CPD measurements which are used to electronically characterize semiconducting surfaces (§ 4.1). Suitable samples for cell-semiconductor electronic interaction studies are carefully selected (§ 4.2) and electronically characterized via CPD measurements (§ 4.3-5). In particular their electronic 'steady state' is studied in § 4.3, while the effect of H-etching and selected chemical treatments is described in § 4.4 and § 4.5, respectively.

4.1. CPD apparatus, calibration and experimental procedure for CPD measurements in air

The CPD apparatus was properly assembled to reduce stray capacitances and electromagnetic, mechanical and noise interference and calibrated to obtain the maximum possible accuracy of the instrument. § 4.1.1 describes the experimental apparatus and its assembly while § 4.1.2 particularly focuses on the apparatus calibration and suggests several precautions that may be taken while performing CPD measurements. In § 4.1.3, we describe the classical procedure adopted when measuring the surface potential (Φ_s) of a dry semiconductor.

4.1.1. Experimental apparatus

As explained in Chapter 1, the components of a basic CPD system are a vibrating Monroe probe connected to an electrostatic voltmeter for the detection of CPD voltages and a grounded chuck for sample backside grounding. To facilitate the reader in the understanding of the next sections we recall from § 1.4 the following concepts: (i) a Monroe probe measures a voltage that is defined as the CPD voltage (V_{cpd}); (ii) in dark-light measurements two different voltages are acquired by the CPD system, one in dark ($V_{cpd,dark}$) and one under deep illumination ($V_{cpd,light}$); (iii) the difference between these two values yields a semiconductor surface potential (e.g., $\Phi_s = V_{cpd,dark} - V_{cpd,light}$).

The Monroe probe used in our system is a 1017AEL-5 model from Monroe Electronics (ME) [111]. The 1017 AEL-5 probe presents a large diameter sensing aperture (i.e., 3.30 mm) which enables low noise measurements at a probe-to-surface spacing as large as 6 mm. Its output was connected to an SDI (Semiconductor Diagnostic, Inc.) PDM-40 electrostatic voltmeter which resolved the CPD voltage (V_{cpd}) sensed by the probe by applying the null-method suggested by Kelvin [44]. The same voltmeter provided the ground reference potential for the gold-coated vacuum chuck, which is the platform where the sample was positioned during the measurements. In order to exclude external electromagnetic field and possible noise sources the probe and the chuck were situated inside a Faraday cage which was properly grounded. An image of the basic experimental apparatus inside the Faraday cage is shown in Fig. 4.1.

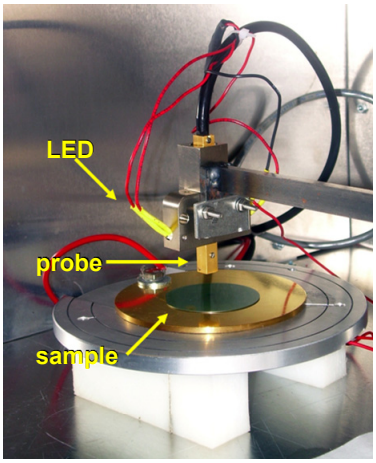

Figure 4.1. Experimental CPD apparatus housed inside a Faraday cage (probe, sample, chuck and LED shown). Note: probe is shown protruding out of the probe holder arm for display purposes only.

The output of the PDM-40, which displays, when properly calibrated, voltages with a maximum accuracy of 1 mV, was connected to a Keithley 2000 voltmeter which was interfaced to a computer for automated data collection through an IEEE GPIB interface card. A suitable program was coded in the measurement control software Labview for data collection and storage. The CPD voltage as output from the Labview program after each measurement was calculated from an average of 25 samples taken with a sampling period of 10 ms. A Tektronix TDS 1002B oscilloscope was used as a diagnostic aid for the PDM-40 calibration.

In order to perform the dark/light measurements necessary for the determination of the semiconductor surface potential two ultraviolet (UV) light emitting diodes (LEDs) with a 370 nm primary emission wavelength were positioned within the terminal part of the probe holder with an angle that allowed proper illumination of the semiconductor surface for a fixed range of probe-sample distances (Fig. 4.1). To allow proper illumination of the sample the Monroe probe was used while retracted in the probe holder

(e.g., a different arrangement than that shown in Fig. 4.1). UV light was chosen because the photon energy of the light needs to be greater than the SiC energy band gap (i.e. E_{uv} > 3.23 eV) in order to generate enough electron hole pairs (EHP) for the semiconductor surface to approach flatband.

4.1.2. CPD system calibration and measurement precautions

Since surface potential is highly dependent on the semiconductor material morphological and electronic properties, CPD measurements are sample variable and definitely non-trivial to make with a high enough level of precision to gain useful information. Therefore several precautions have to be used when performing these types of measurements. In this section we describe the calibration procedure and precautions which allowed us to perform good-quality CPD measurements in air and that, in the end, made possible a successful characterization of the cell-semiconductor electronic interaction.

Measuring distance selection. Even though the AEL1017-5 Monroe probe model allows measuring distances as large as 6 mm, the choice of operating at small probe-to-sample distances was made based on the fact that larger distances make the measurement more susceptible to external noise and decrease the electrostatic voltmeter response speed. The PDM-40 voltmeter was periodically calibrated to ensure spacing-independent measurements for a probe-to-sample distance ranging from 0 to 2.5 mm. Even though this precaution was constantly taken we opted to work at a constant probe-to-sample distance to avoid the effect of stray capacitances, which are known to be distance dependent [42]. The optimal operating probe-to-sample distance was selected to maximize both the sample illumination (e.g., maximization of the light intensity on the

area below the measuring electrode) and the measurement accuracy (e.g., minimization of the standard deviation of a series of readings from the same surface). While the maximization of the sample illumination was straightforward (we selected the range of distances for which the two discs of light originating from the UV diodes would intersect on the sample surface), the determination of the measurement accuracy required us to take several V_{cpd} readings of the grounded chuck at different probe heights and to calculate the measurement standard deviation at each specific distance. Mean ($\overline{V}_{cpd}$) and standard deviation (σ) for a three measurement distribution at each analyzed distance are listed in Table 4.1. The probe-to-sample distances analyzed are the ones which allowed the maximization of the light coverage on the sample surface.

Table 4.1 CPD voltage mean ($\overline{V}_{cpd}$) and standard deviation (σ) measured for the grounded chuck in the dark and at different probe-to-sample distances.

Probe-to-sample distance (mm)	1 mm	1.6 mm	2.3 mm
$\overline{V}_{cpd}$ ± σ (mV)	0.42 ± 0.24	1.08 ± 1.34	0.28 ± 1.96

As expected, the smallest standard deviation was obtained for the smallest probe-to-sample distance which was therefore selected as the optimal measuring distance. Hence, all the measurements described in this chapter were performed with the probe 1 mm above the sample surface.

Verification of the signal transient detection capability. Besides reading the CPD voltage of a semiconductor in equilibrium (e.g., V_{cpd} is constant since no photo-excitation, electric field , or chemical charging of the surface is applied), the CPD system has to be able to detect quick variations in the CPD voltage without significant delay.

This is because when light shines on the semiconductor surface the voltage quickly shifts from $V_{cpd,dark}$ to $V_{cpd,light}$. The capability of the apparatus to detect fast signal transients was checked by applying a square waveform to the metallic chuck using a Clarke-Hess 748 function generator and by comparing, using the Tektronix oscilloscope, the original applied waveform and the Vcpd signal detected by the system (Fig. 4.2). The period of the applied waveform was 10 ms while its amplitude was 220 mV (the amplitude of the signal reported in Fig. 4.2 is 100 times attenuated).

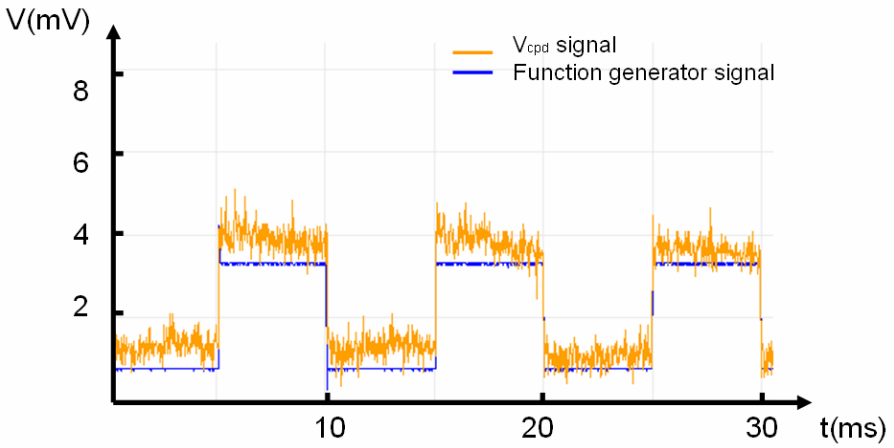

Figure 4.2. Comparison between the V_{cpd} signal detected by the CPD system and the original voltage signal as observed via oscilloscope. This result confirms the possibility to measure fast (sub-ms range) transients with our CPD apparatus.

As is evident from Fig. 4.2, the CPD system was able to perfectly detect the square waveform applied to the metal chuck. Rise and fall times of the detected signal were below 15 µs.

Stray capacitance. During preliminary measurements performed with the CPD apparatus we observed the capacitive coupling of metallic cable connectors to the Monroe probe plates. After this finding, most of the metallic connections in the apparatus were properly insulated to reduce stray capacitances.

Sample charging operated by the vibrating Monroe probe. Leaving a semiconducting sample under the CPD probe for long times may cause an evident charging effect on the semiconductor surface. This charging effect is probably generated by the chemical species deposited by the vibrating shutters of the probe on the semiconductor surface. Hence, in all the experiments described in this and the next chapter, samples were never left under the vibrating probe for long time spans. For the case of long recovery times (e.g., typically required by hexagonal SiC) samples were removed from the apparatus and repositioned later. If vibrating probes are to be used for time-continuous CPD measurements we strongly recommend the active use of the nitrogen purge insert which many of them incorporate. A plot of a significant charging effect caused by the probe on a 3C-SiC sample is reported in Fig. 4.3.

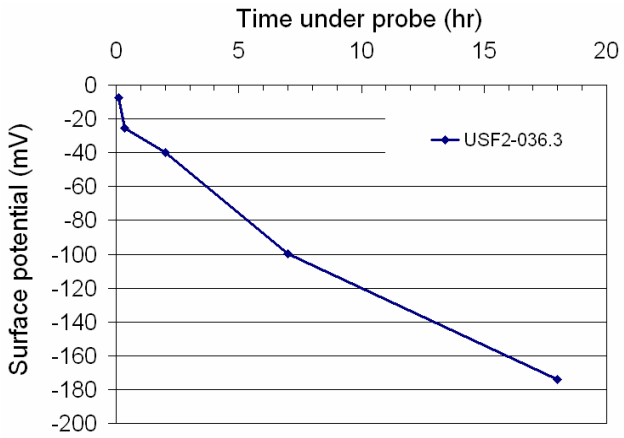

Figure 4.3. Probe charging effect on the surface of a 3C-SiC epilayer within the first 18 hours. Note the decay in the observed CPD voltage caused by continuous measurement over the sample surface.

Instrument performance verification. As a final step in the calibration procedure, the instrument performance was compared to that of a similar commercial CPD apparatus from SDI. A comparison between the readings obtained at USF and SDI for 4H-SiC

epitaxial samples are listed in Table 4.2. Considering that surface potentials may vary significantly (up to tens of millivolts) on different areas of the same semiconductor because of small topographical differences, crystal defects and impurities the results reported in Table 4.2 can be considered highly satisfactory. In conclusion, the USF CPD apparatus used in this work was well calibrated and, therefore, measurements made with this tool are reliable.

Table 4.2 Comparison of CPD measurements of 4H-SiC epilayers using two CPD tools. Values obtained with the USF CPD system are compared to those obtained with a similar system at SDI.

Sample ID	Doping type	SDI CPDM apparatus	USF CPDM apparatus
		Φ_s (mV)	Φ_s (mV)
USF-b-003	n	-330	-340
USF-b-005	p	380	370

4.1.3. Procedure for CPD measurements of semiconductors in air ambient

A specific procedure was developed to perform CPD measurements of semiconductors in air ambient. The procedure, described below, was used to perform all the CPD measurements that were used to characterize the electronic behavior in 'steady state' and upon charging of the samples selected for the semiconductor-cell-electrolyte measurements.

1) Sample positioning over the vacuum chuck

2) Vacuum pump activation

3) Probe lowering at 1 mm from the sample surface

4) Faraday cage closure

5) Measurement in dark → $V_{cpd,dark}$

6) Switch on UV light

7) 10 second wait

8) Measurement in light → $V_{cpd,light}$

9) Switch off UV light

10) Calculation of surface potential: $\Phi_s = V_{cpd,dark} - V_{cpd,light}$

11) Repetition of steps (5) to (10) for a second time

In step (1) we always used metallic tweezers because charging effects were observed when handling the samples with Teflon or plastic tweezers. Since the $V_{cpd,light}$ value was reached with different time intervals for different samples and it mostly depends on the quality of the crystal material (e.g., trapping effects may increase the time necessary to get to $V_{cpd,light}$), we selected the 10 second time interval between measurements after preliminary experiments indicated it as the ideal illumination time. The surface potential values reported in the next sections are expressed as mean ($\overline{\phi_S}$) ± standard deviation (σ) and are calculated from a two measurements distribution.

4.2. SiC and Si for cell-semiconductor interaction studies: sample selection and description

The final objective of this work is to study the electronic interactions between biological cells and SiC samples via CPD. In order to perform successful CPD measurements of the complex semiconductor-cell-electrolyte system the CPD apparatus

has been properly assembled and calibrated (§ 4.1). In this section we first discuss how we selected suitable samples for cell-semiconductor CPD investigations (§ 4.2.1) and then describe their characteristics (§ 4.2.2). Besides SiC samples, Si samples were also selected for cell-semiconductor interaction studies and are therefore electronically characterized via CPD in this chapter. Si samples are mostly used as controls to ensure the validity of the performed CPD measurements, since the surface potential of this material in response to different chemical processes has been characterized by past studies [112-114].

4.2.1. Sample requirements for dry and wet CPD measurements

The choice of suitable samples for the cell-semiconductor electronic interaction studies we aim to perform is of primary importance. In this section we describe which sample characteristics may negatively affect the dry (sample in air) and wet (sample in liquid) CPD measurements and how they influenced our sample selection.

Doping concentration. High doping concentration in a semiconductor reduces the possible band bending range and, therefore, the sensing potentiality when a charge is deposited on its surface. Therefore, we chose to work only with samples that presented doping concentrations $N_{A,D} < 10^{17}$ atoms/ cm^3.

Epilayer thickness. The penetration depth of the UV light used in our apparatus to generate the SiC flatband condition ($h\nu$ = 3.4 eV) is approximately 8 μm for the cubic and 11 μm for the hexagonal polytype [115]. If the epilayer thickness is lower than these values the possibility of having interference in the CPD measurements caused by the generation of EHPs in the substrate underlying the epilayer is significant. We found that for hexagonal p-type SiC epilayers grown on n+ bulk crystals the presence of a p-n

junction relatively close (typically < 20 μm) to the sample surface affected the dark-light CPD measurements by causing $V_{cpd,light}$ oscillation and a typical n-type behavior which was probably generated by majority carrier injection from the substrate into the epilayer. To avoid this problem, all the p-type samples selected for the CPD studies reported in the rest of this work were bulk crystals. On the other hand, the presence and depth of SiC-Si heterojunctions in the 3C-SiC epilayers grown on Si seemed not to constitute a problem for CPD measurements. A specific experiment was designed to evaluate the effect of the heterojunction depth on the V_{cpd} readings: 3C-SiC epilayers whose Si substrates were removed and a series of 3C-SiC epilayers on Si with thickness varying from 3 to 20 μm were chemically charged and their surface potentials then measured. No significant differences were found among the magnitudes of their surface barriers which indicated an irrelevant effect of the heterojunction on the final CPD readings. Therefore the 3C-SiC epilayers used in the rest of this work present variable thickness.

Sample dimensions. In several instances we noticed that measurements of samples with areas smaller than 1 cm^2 were less accurate and repeatable than measurements of samples with larger areas. This result can be easily justified by the existence of fringing effects arising from the fact that the sample dimensions are close to the measuring electrode dimensions. Therefore, samples with areas larger than 1 cm^2 were used for all the experiments described in this chapter.

4.2.2. Selected SiC and Si samples for cell-semiconductor CPD investigations

The samples selected to perform the cell-semiconductor electronic interaction studies, and which therefore will be electronically characterized in the next sections with different chemical charging procedures, were as follows: 3º off-axis n-type 6H-SiC(0001)

epilayers grown on 6H-SiC and doped in the low 10^{16} cm^{-3} range; 3.5º off-axis pure grade p-type bulk 6H-SiC(0001) doped in the low 10^{15} cm^{-3} range; 3C-SiC(001) epilayers grown on Si(001) and unintentionally doped n-type in the 10^{15} cm^{-3} range; n-type bulk Si(001) doped in the low 10^{15} cm^{-3} range; p-type bulk Si(111) doped 2×10^{15} cm^{-3}. The samples were at least five for each category reported. All the samples had dimensions of at least 4.9 cm^2 (e.g., a quarter of a two inch wafer) and presented extremely flat surfaces (see Fig. 4.4). In particular, all the SiC surfaces presented atomic steps: the ones that originally presented polishing scratches were H-etched with processes suitable for the specific polytype (Chapter 2) to generate atomically flat surfaces and subsequently reduce the surface state density.

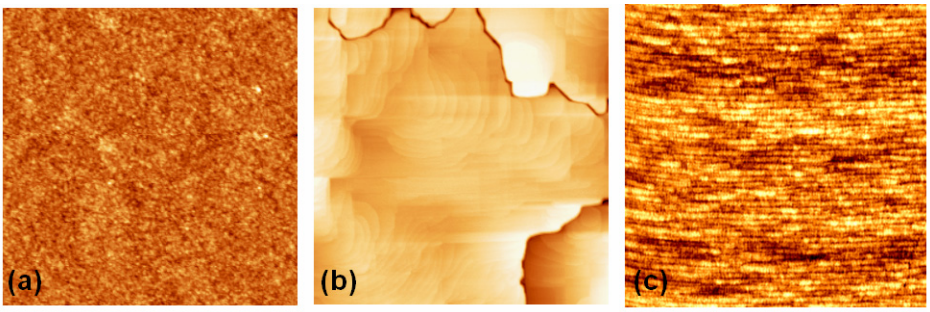

Figure 4.4. AFM micrographs (2×2 μm scans taken in tapping mode) reporting the morphologies of the samples selected for CPD measurements: (a) n-type Si(111), (b) 3C-SiC(001), (c) n-type 6H-SiC(0001). P-type Si(111) and 6H-SiC(0001) (not shown) presented surface morphologies similar to (a) and (c), respectively.

4.3. Surface potential of SiC and Si in 'steady state'

As we already pointed out in the introductory section, it is of primary importance to electronically characterize, via CPD, the samples selected for cell-semiconductor electronic interaction studies. If the pattern of the typical electronic behavior of these

samples in response to different chemical charging processes is defined, it should be easier to understand the more complex electronic response that they may have in relation to electrolytes or cells. It is therefore of primary importance to define the initial band bending of these surfaces before any kind of surface charging or hydrogen etching process is applied. Since, in many instances after chemical treatment, the initial states (i.e. band bending) were also the ones to which each specific sample had the tendency to come back to, we defined them as 'steady states'. The samples analyzed in this section and in the rest of the chapter reached their 'steady state' after being treated with RCA cleaning in the past.

To facilitate the reader in the analysis of the CPD results reported further in the text we recall that when a surface is charged positively the bands bend down ($\Phi_s > 0$) and when is charged negatively the bands bend up ($\Phi_s < 0$). Hence, for an n-type semiconductor the surface potential Φ_s is zero for flatband, negative for depletion and positive for accumulation. The opposite is true for p-type. Table 4.3 contains an elucidation of these concepts.

Table 4.3 Semiconductor surface potential versus the overall surface charge.

	Surface charge > 0	Surface charge < 0
n-type	$\Phi_s > 0$, accumulation	$\Phi_s < 0$, depletion
p-type	$\Phi_s > 0$, depletion	$\Phi_s < 0$, accumulation

The 'steady state' conditions for the samples studied were the following: accumulation for p-type Si(111); depletion for n-type Si(111) as well as for p- and n-type SiC(001). The observed conditions were in agreement with what has been reported in the

literature [114, 116] and suggest that all the samples were depleted of their majority carriers at the surface with the exception of p-type Si(111). The results obtained for Si and n-type SiC may be explained by the predominance of filled acceptor states near the surface. Instead, we suggest the presence of unoccupied donor states on p-type SiC surfaces. Fig. 4.5 is a band diagram representation of the 'steady state' condition for both Si and SiC surfaces. Obviously, the fact that the surface appeared to be negatively (positively) charged for n- and p-type Si and for n-type SiC (p-type SiC) does not mean that only filled acceptor (unfilled donor) states were present on the surface of these semiconductors, but that probably their effect was the predominant one.

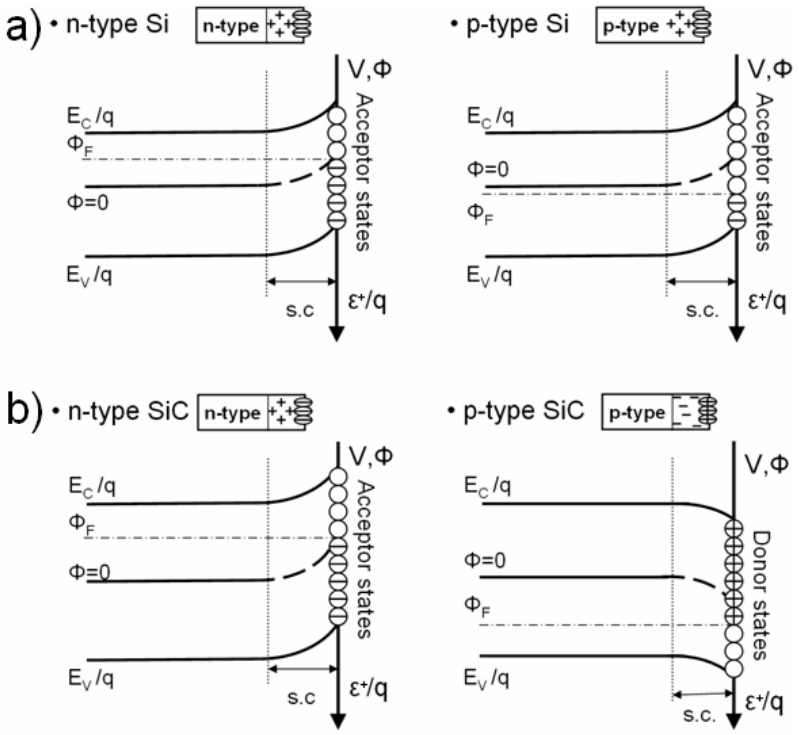

Figure 4.5. Band diagram representation of the 'Steady state' condition for n- and p-type (a) Si and (b) SiC surfaces, respectively.

4.4. Effect of hydrogen etching on the surface potential of SiC surfaces

Besides producing atomically flat surfaces, H-etching should also terminate most of the dangling bonds of SiC surfaces with H atoms [117, 118], which should cause significant changes in the measured value of Φ_s. Moreover, if a complete chemical passivation of the SiC surface is achieved with H-atoms, the resulting measured surface potential should be null [119]. From an electronic point of view this happens because hydrogenation replaces the surface states with Si-H bonding and antibonding states, which are positioned below the valence-band maximum and above the conduction band minimum, respectively. Hence, no charge is transferred, which results in flatband (Φ_s=0) [117, 118]. Therefore H-etching represents an additional technique, besides wet chemical treatment (§ 4.5), that can be used to modify the electronic properties of a surface and therefore to define its electronic behavioral pattern. The H-etching processes used to modify the surface potentials of 3C- and 6H-SiC samples were similar to the ones specifically developed in Chapter 2 for these polytypes, with the only difference that the etching times were reduced in a way that would ensure maximum H-termination but minimum surface morphology modification. Since all the SiC samples, selected for this experiment from the groups reported in § 4.2.2, were already atomically flat at the moment of etching we did not want to risk surface over-etching which would increase surface state density. In fact, we are only interested in the chemical effect that processes have on the electronic state of the selected surfaces, and not on the influence of other variables such as surface morphology. We therefore reduced the etching time of 3C-SiC to 10 minutes and of 6H-SiC to 5 minutes.

After H-etching, we found that 3C-SiC(001) was in a flatband condition. This is a promising result because it shows the possibility of a complete electronic passivation of 3C-SiC surfaces which was never reported before. Complete passivation of hexagonal SiC surfaces was reported by Seyller for n-type 6H-SiC($000\bar{1}$) and p-type 6H-SiC(0001) [118]. In this section we first report the results obtained by time-monitoring, via CPD, the H-etched 3C-SiC(001) surfaces (§ 4.4.1) and we then investigate, via XPS and ATR-FTIR, the possible causes of the observed electronic passivation (§ 4.4.2). We also studied via CPD the effect of H-etching on n-type and p-type 6H-SiC(0001) (§ 4.4.3). However, in this case, electronic passivation was not observed.

4.4.1. Electronic passivation by H-etching of n-type 3C-SiC epilayers

N-type 3C-SiC(001) epilayers were treated with 10 SLM of ultra-pure (grade 8.0) hydrogen for 10 minutes at 1200 ºC and AP. They were kept under hydrogen flow until a few minutes before their extraction from the CVD reactor, which took place at 400 ºC . Just before the sample extraction the CVD reactor was purged with Ar to avoid dangerous combustion which otherwise may take place when opening the reactor door. The surface potential of these samples was measured before hydrogen treatment, immediately after and then monitored periodically over time. All the samples used in this experiment presented 'steady state' depletion values of Φ_s between -160 and -180 mV. All of them displayed, immediately after H-etching, values of Φ_s between 0 and -7 mV which is indicative of complete electronic passivation. Fig. 4.6 reports the surface potential monitoring for different 3C-SiC epilayers up to 1000 hours after the etching process.

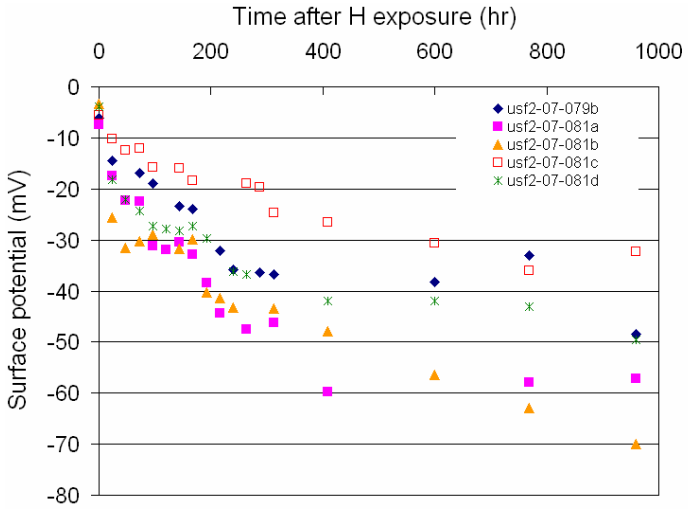

Figure 4.6. Surface potential vs. time of several H-etched 3C-SiC(001) epilayers presenting similar characteristics. A quasi-null surface potential was observed immediately after etching on all the surfaces.

It is evident that the surface potential changed quite rapidly during the first few days after H-etching. In average, after 10 days (i.e., 240 hours), the surface potentials of these samples were within 10 mV from their final values, which have larger magnitudes than the initially measured quasi-null Φ_s. We confirmed these results over a large number of samples.

Other experiments were performed to study the effect of the final hydrogen cooling temperature on the magnitude and time variation of Φ_s. Besides 400 ºC, the final hydrogen cooling temperatures studied were 550, 1000 and 1200 ºC. The basic etching process applied was identical to the one described above with the only difference that after the hydrogen flow was interrupted (at 550, 1000 and 1200 ºC, respectively) all the samples were cooled down in Ar until their extraction from the CVD reactor which was performed at 400 ºC. We found that the surface potential time dependence of samples cooled down in hydrogen to a final temperature of 550 ºC was completely similar to what

was reported in Fig. 4.6. In fact, immediately after H-etching, those samples displayed quasi-null Φ_s values and reached, in roughly 10 days, the final Φ_s value. On the other hand, although all the samples cooled down in hydrogen to higher final temperatures presented quasi-null Φ_s values immediately after H-etching, they very quickly abandoned this condition. The ones cooled under hydrogen to 1000 ºC displayed surface potential values of roughly 20 mV after 2 hours of air exposure (Fig. 4.7, filled squares). In a more dramatic way, samples cooled down under hydrogen only to 1200 ºC presented surface potentials of roughly 20 mV after only 20 minutes in air ambient (Fig. 4.7, filled triangles).

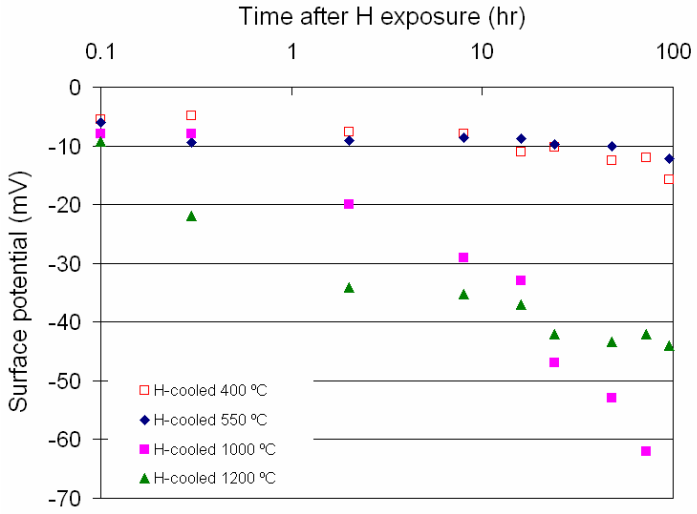

Figure 4.7. Surface potential vs. time of H-etched 3C-SiC(001) epilayers with final hydrogen cooling temperatures of 400 ºC (unfilled squares), 550 ºC (filled diamonds), 1000 ºC (filled squares) and 1200 ºC (filled triangles). Note that the time axis is logarithmic.

From these results we can conclude that the stability of the electronic passivation of 3C-SiC(001) epilayers strongly depends on the final hydrogen exposure temperature. In another instance we also demonstrated that etching processes which cause drastic surface

morphology variations will not lead to electronic passivation. Specifically, an atomically flat 3C-SiC epilayer treated with 10 SLM of hydrogen for 1 minute at low pressure and 1200 ºC and which presented, after the process, a much rougher and less ordered surface, did not display a quasi-null surface potential.

The effect of Ar annealing on 3C-SiC(001) epilayers was also investigated. Several samples with 'steady state' surface potentials of roughly -180 mV were Ar-annealed in the same CVD reactor used for H-etching at 1200 ºC and atmospheric pressure for 10 minutes. The results obtained are reported in Fig. 4.8.

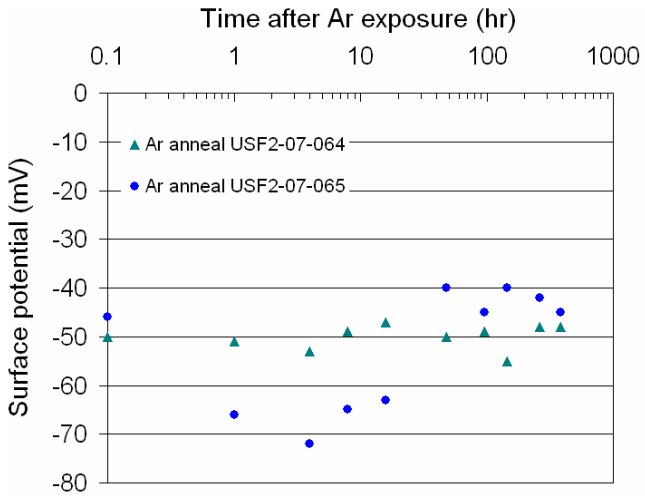

Figure 4.8. Surface potential time monitoring, via CPD, of two Ar-annealed 3C-SiC(001) samples with similar characteristics. Note that the time axis is logarithmic.

It is evident from Fig. 4.8 that Ar-annealing did not provoke a quasi-null surface potential. However, the potential measured immediately after annealing was significantly lower than the one presented by the same surfaces before the process and was totally comparable to the final Φ_s reported above for H-etched surfaces (which was in average -50 mV). We also observed that all the as-grown 3C-SiC epilayers (e.g., never treated chemically after the growth process) displayed the same Φ_s values and time dependence

than those reported in Fig. 4.8. This evidently indicates that the oxide layer that forms as soon as the sample is extracted from the CVD reactor is very stable and provides a much better electronic passivation than the oxide formed on the same surfaces after chemical treatment (e.g., after chemical treatment Φ_s < -100 mV for 3C-SiC always, as shown by Tables 4.6 and 4.7). This is also confirmed by the fact that some of the H-etched samples, which where HF dipped while they still presented a very low Φ_s, displayed, after HF treatment, less electronically passivated and more negatively charged surfaces (results reported in Table 4.4).

Table 4.4 Charging effect of HF dip on H-etched n-type 3C-SiC epilayers. Before HF dip the surfaces displayed a small $|\Phi_s|$ and an almost flatband condition. After HF dip the surfaces were evidently in a depleted condition.

	USF2-07-063b	USF2-07-054.2
Φ_s before HF dip (mV)	-29.6	-27.0
Φ_s after HF dip (mV)	-140.9	-151.1

4.4.2. Characterization of passivated 3C-SiC surfaces via XPS and ATR-FTIR

Since electronic passivation typically implies complete H-termination [118, 120], we decided to investigate the surface chemistry of the etched samples to probe if this was the case for our surfaces. Moreover, chemical studies can be used to motivate the differences in electronic behavior observed between H-etched and HF treated samples. The chemical characterization techniques used for this purpose were X-ray photoelectron spectroscopy (XPS) and attenuated total reflectance Fourier transform infrared spectroscopy (ATR-FTIR). We performed XPS studies, whose results are reported below, on an n-type 3C-SiC(001) sample before and after H-etching. The data obtained from the

analysis performed before H-etching refer to an HF dipped surface which presented Φ_s = -202.8 mV, while after H-etching the sample presented Φ_s = -7.1 mV. Surprisingly, a relatively high amount of oxygen was found on the etched surface (Fig. 4.9), which was comparable to the amount observed before etching (not reported). The magnitude of the O peak excludes the possibility that the oxygen observed is a minor contamination.

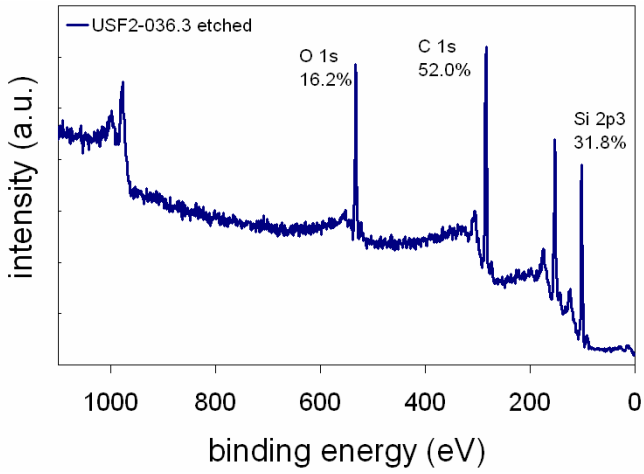

Figure 4.9. XPS spectrum of a H-etched 3C-SiC(001) epilayer and relative elemental concentrations as calculated from the survey. A relatively high concentration of O was observed on the surface.

However, the high resolution (HR) XPS scans showed the existence of differences on the surface before and after etching. In particular, the graphitic carbon concentration appeared to be lower for the etched surface (as is shown by the smaller shoulder in the HR C_{1s} peak of the etched sample in Fig. 4.10(b)).

Since it is quite easy to determine differences in band bending by photoelectron spectroscopy, we used the obtained HR spectra to confirm what was measured via CPD. Shifts in band bending can be measured via XPS because core level binding energies (e.g., E_b^{C1s}) referenced to the Fermi level (E_F) vary with surface band bending and

because the sampling depth of XPS (2 nm) is much smaller than the width of the space-charge layer. As is evident from Figure 4.10(a) and (b) which report, respectively, the Si_{2p} and C_{1s} HR spectra obtained for etched and un-etched 3C-SiC, the core level binding energies of the two samples are shifted by roughly 0.315 eV. The Si_{2p} and C_{1s} core level spectra of the H-etched sample shifted to higher binding energies, which is consistent with what was reported by Seyller [118] for n-type hydrogenated 6H-SiC($000\bar{1}$) surfaces. From the energy band shifts observed with XPS we could deduce that the magnitude of the surface potential change between HF dipped and H-etched samples was around 300 mV, which is ~100 mV higher than the one measured via CPD. This is possibly because the value was roughly calculated from XPS spectra which were not performed with the aim of detecting band bending energy shifts. However, the shifts observed in the XPS spectra strongly confirm the existence of a different electronic behavior caused by different treatments on the same sample.

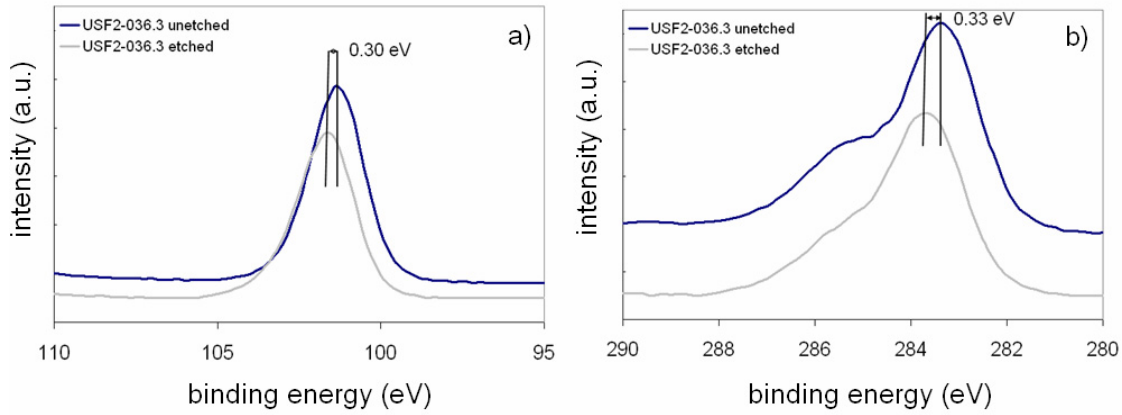

Figure 4.10. Si_{2p} and C_{1s} core level spectra obtained for the same 3C-SiC epilayer before etching (bold line) and after etching (light line). The core level spectra are shifted to higher binding energies after H-etching treatment indicating a modification in surface potential.

We should mention that even though the quasi-null surface potential measured for H-etched 3C-SiC epilayers may have strongly suggested the presence of a complete chemical passivation operated by H atoms in a similar fashion to Si surfaces [120], the LEED data presented in § 2.2.3 for 3C-SiC epilayers treated with the same etching process provide evidence of a different situation. In fact, if the etching process applied on 3C-SiC had produced a completely H-terminated surface, the resulting LEED pattern should have been an unreconstructed (1×1), where instead we observed a (5×1) (§ 2.2.3).

To better understand the causes of the peculiar electronic behavior observed for the etched epilayers, we performed ATR-FTIR studies which, differently than XPS, can provide interesting information regarding the presence and bonding of hydrogen on the surface. In these studies, performed under a constant nitrogen purge using a 45º beveled ZnSe crystal, we analyzed etched and HF dipped 3C-SiC samples with characteristics similar to those of the sample analyzed via XPS. The major differences that were observed by comparing the FTIR spectra of the etched and un-etched, HF treated, samples were the following: the spectra of the etched sample exhibited peaks due to C-H bonds (Fig. 4.11), while the spectra of the un-etched sample presented a signal at wavenumbers corresponding to Si-OH bonds (Fig. 4.12). No peaks in the wavelength range of 2000-2100 cm^{-1} that could be associated to Si-H bonds were observed on either sample. However, the absence of Si-H peaks from the FTIR spectra of the H-etched sample, where they would be mostly expected, does not imply that Si-H bonds were not present on the sample surface. In fact, since the ATR-FTIR apparatus used was not equipped with a polarizer, we could not perform p-polarized analysis, which can reveal bonds perpendicularly oriented to the surface as Si-H on SiC surfaces may be [121].

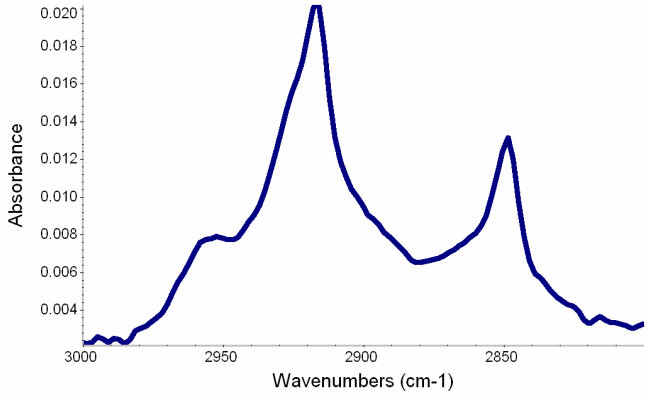

Figure 4.11. ATR-FTIR spectra of H-etched 3C-SiC in a C-H stretch region indicating the existence of different typologies of C-H bonds.

The major peak frequencies of the H-etched 3C-SiC epilayer in the C-H stretch region were located at 2849, 2917 and 2952 cm^{-1} and assigned to CH_3 asymmetric, CH_2 asymmetric, and CH_3 symmetric bonds, respectively (Fig. 4.11). However, we also observed, by deconvoluting the spectra, sp^3CH and CH_2 symmetric stretching modes. From a joint analysis of the XPS and FTIR data, it appears that the 3C epilayer surface contains, after H-etching, both oxygen and hydrogen, the latter being directly bonded to C. Amy *et al*. reported that hydrogenation of 3C-SiC(001) surfaces with a (3×2) LEED pattern leads to passivation of the topmost dangling bonds but creates and stabilizes others below the top surface. Once the hydrogenated surface was exposed to molecular oxygen they observed oxygen incorporation below the top surface without any loss in the H coverage [120]. Even though our 3C-SiC(001) surfaces presented a different surface reconstruction (i.e. (5×1)), it is still likely that, upon molecular oxygen exposure, O atoms were incorporated below the top surface without affecting the H-terminated topmost dangling bonds. Further studies are needed to investigate these interesting findings. However, the fact that H-etched 3C-SiC presented a high density of C-H

bonding, sustains the suggestion made in § 2.2.3 that the H-etched 3C-SiC epilayers may be C-terminated underneath the oxidic layer.

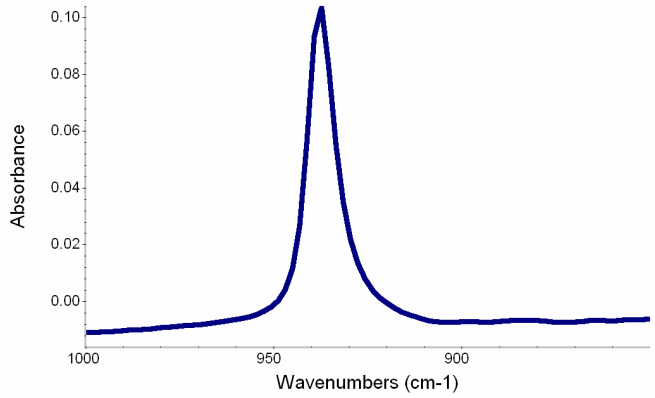

Figure 4.12. ATR-FTIR spectra of un-etched, HF treated 3C-SiC in a Si-OH stretch region displaying the existence of Si-OH bonds.

The Si-OH peak observed for the HF dipped samples (Fig. 4.12) confirms that this chemical treatment leaves the SiC surface essentially covered with -OH groups [118]. The hydroxylic groups are probably the cause of the depletion (i.e., $\Phi_s < 0$) observed on the n-type surfaces after HF dip.

Summarizing, the results presented in the last two sections indicate that the 3C-SiC surfaces are, after an appropriate H-etching process, electronically passivated. However, at a chemical level the surface does not present only hydrogen atoms, which is the case for Si [120], but also significant amounts of oxygen. The electronic passivation tends to deteriorate over time and under ambient conditions. However, the final Φ_s value at which the H-etched epilayers tend to stabilize is much lower in magnitude than the one measured for the same surfaces after HF treatment, which evidently tends to add negative charges to the sample surfaces.

4.4.3. Surface potential of H-etched 6H-SiC

In this section we describe the effect of H-etching on n- and p-type 6H-SiC(0001) surfaces. H-etching was performed at 1550 ºC for 5 minutes at atmospheric pressure and with a hydrogen flow of 10 SLM. Before the etching process both the n-and p-type samples were found to be in depletion, which is a typical condition for SiC surfaces (§ 4.3). After etching, however, n-type 6H-SiC(0001) became more depleted while p-type 6H-SiC(0001) was characterized by a strong accumulation. Hence, H-etching seems to charge the surface of 6H-SiC samples negatively by probably filling acceptor states. The surface potential observed after etching did not vary significantly within the first 1000 hours (Fig. 4.13), which indicates that, even if the surface of these hexagonal SiC samples was not electronically passivated, it was stable over time.

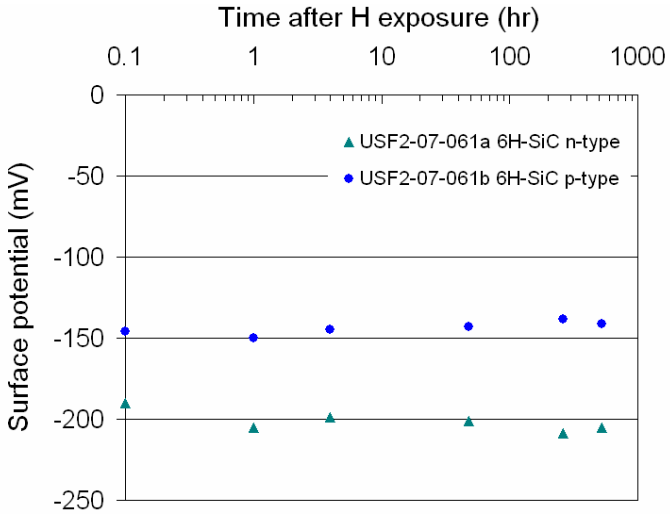

Figure 4.13. Surface potential time monitoring, via CPD, of H-etched n-type (triangles) and p-type (circles) 6H-SiC surfaces. Note that the x axis is logarithmic.

4.5. Effect of chemical treatments on SiC and Si substrates

Different chemical treatments were used to study the electronic behavior of Si and SiC samples upon charging. Specifically, Si and SiC surfaces were treated with HF and potassium permanganate ($KMnO_4$) solutions and the magnitude of the band bending generated by the specific treatment on these samples was evaluated. Since HF dip is the last cleaning step performed before cell deposition (§ 5.1.3), determination of its effect on the band energy level is significant. The information obtained in this section is used to model the general surface potential behavior of the samples selected for the semiconductor-electrolyte/semiconductor-cell-electrolyte systems and as a possible aid for understanding the results presented in Chapter 5. Si substrates were used not only to study the surface potential of smaller bandgap materials after chemical treatment but also to verify the validity of the obtained results since the electronic status of Si surfaces upon chemical treatment is partially already known [112-114]. § 4.5.1 describes the experimental procedure used for charging the Si and SiC surfaces while § 4.5.2 reports and discusses the results.

4.5.1. Chemical charging experimental procedure

The HF treatment was executed in the following manner: sample dip in a 50:1 $HF:H_2O$ solution for 1 minute; thoroughly rinse in DI water; nitrogen dry. To charge the surface by using potassium permanganate the samples were immersed, after the oxide was removed, in a 2:3 $KMnO_4:H_2O$ solution warmed at ~ 35 ºC for 10 minutes, rinsed in DI water, and nitrogen dried. The charging processes and the subsequent CPD measurements, whose results are reported below, were repeated for at least three samples of each typology listed in § 4.2.2.

4.5.2. Band bending operated by chemical charging of the surface: results and discussion

Before chemical treatment all the samples were in the 'steady state' condition described in § 4.3. Upon HF treatment, the p-type Si surfaces abandoned the accumulation condition and became depleted while the depletion of the n-type Si surfaces became less significant (Table 4.5). These results definitely show that HF treatment adds positive charges on Si surfaces which agrees with what was reported in [114]. This also indicates that the surface passivation is not complete and that, even if the surface is very likely largely H-terminated (which is confirmed by the higher hydrophobicity of these surfaces), oxygen is still present (as confirmed by XPS analysis). However, it has to be mentioned that the significant Φ_s reduction observed for n-type Si(111) is likely an effect of the better passivation operated by a partial H-termination of the surface.

Upon HF treatment, n-type and p-type SiC samples were still found to be depleted as they were before. However, as can be seen in Table 4.5, n-type SiC showed a greater depletion (e.g., more negative Φ_s value $\rightarrow$ larger depletion width) while p-type SiC tended towards a less depleted state. This is indicative of a higher negative charge on SiC surfaces after the HF dip. It is known that HF treatment on SiC surfaces does not produce the passivating results that it does for Si: thin native oxides (~10 Å) are typically present on the surfaces of each SiC polytype immediately after HF exposure [116]. This was confirmed by the ATR-FTIR and XPS analysis performed on HF treated 3C-SiC samples and whose results are reported in § 4.4.2. The presence of hydroxilic groups -OH, detected on 3C-SiC surfaces via ATR-FTIR (Fig. 4.13), is a likely explanation for the increase in negative charge observed after HF treatment.

In conclusion, all of the SiC and Si samples displayed different degrees of surface depletion after an HF dip: the overall effect at the surface was probably the one of occupied acceptor states for n-type samples and of unoccupied donor states for p-type samples.

Table 4.5 Effect of HF dip on Si and SiC surface potential as measured via CPD.

Sample	Si n-type	Si p-type	3C-SiC n-type	6H-SiC n-type	6H-SiC p-type
$(\overline{\phi_S}) \pm (\sigma)$ (mV) before HF	-219.9 ± 0.6	-60.3 ± 2.8	-119.5 ± 1.1	-207.8 ± 3.2	250.1 ± 7.1
$(\overline{\phi_S}) \pm (\sigma)$ (mV) after HF	-78.2 ± 2.5	114.9 ± 5.9	-168.3 ± 0.1	-240.7 ± 1.9	108.3 ± 3.8

Upon potassium permanganate treatment, which was performed after an HF dip, the Si(111) surfaces appeared to have acquired a more negative charge: n-type surfaces showed a greater depletion while p-type surfaces displayed a decrease in depletion (Table 4.6). On the other hand, the SiC response to potassium permanganate was conflicting: both n-type and p-type surfaces tended to a more depleted state (Table 4.6).

Table 4.6 Effect of potassium permanganate on Si and SiC surface potential as measured via CPD.

Sample	Si n-type	Si p-type	3C-SiC n-type	6H-SiC n-type	6H-SiC p-type
$(\overline{\phi_S}) \pm (\sigma)$ (mV) before $KMnO_4$	-78.2 ± 2.5	114.9 ± 5.9	-300.9 ± 7.1	-339.9 ± 11.8	189.5 ± 14.8
$(\overline{\phi_S}) \pm (\sigma)$ (mV) after $KMnO_4$	-188 ± 4	70.3 ± 0.9	-345 ± 12.8	-1405.6	257.3 ± 13.8

Because of the oxidizing nature of potassium permanganate, an oxide is present on both Si and SiC after the treatment. This oxide introduces additional surface states, and therefore additional charge, Q_{it}, at the interface with the semiconductors. Thus, the surface potential measured after permanganate treatment is probably largely influenced by the charge associated with Q_{it}. Also in this case we can conclude that filled acceptor states were predominant at the oxide-semiconductor interface of n-type Si and SiC while unoccupied donor states defined the response of p-type Si and SiC surfaces.

Although the results reported above could be repeated at different times, it has to be considered that the effect of chemical charging on both Si and SiC samples is extremely dependent on the topographical and electronic characteristics of the particular substrate used. It is possible that two samples presenting the same doping and orientation may still have a different response to a specific chemical treatment. Still, the results presented were confirmed over a sufficiently large selection of samples (especially for 3C-SiC), which makes them statistically relevant. Table 4.7 summarizes what is reported in this section.

Table 4.7 Summary of the effect of HF and $KMnO_4$ on Si and SiC surfaces: charge added by the chemical treatment with respect to the initial state and sign of the surface potential measured.

	Si n-type	Si p-type	3C-SiC n-type	6H-SiC n-type	6H-SiC p-type
HF	Add + charge. $\Phi_s < 0$. depl	Add + charge. $\Phi_s > 0$. depl	Add - charge. $\Phi_s < 0$. depl	Add - charge. $\Phi_s < 0$. depl	Add - charge $\Phi_s > 0$. depl
$KMnO_4$	Add - charge. $\Phi_s < 0$. depl	Add - charge. $\Phi_s > 0$. depl	Add - charge. $\Phi_s < 0$. depl	Add - charge. $\Phi_s < 0$. depl	Add + charge. $\Phi_s > 0$. depl

Both the HF treatment, which is performed before cell deposition, and the potassium permanganate treatment, which helps to reproduce the case when an oxide is present (e.g., immersion in cell culture media), depleted the Si and SiC surfaces of majority carriers. The presence of a depletion layer is ideal for sensing charges added on the surface and therefore is a good starting surface condition for performing semiconductor-cell-electrolyte measurements. In fact, the addition of a fixed amount of charge on the semiconductor surface would cause a much larger signal variation in surface potential when starting from a depletion condition as opposed to accumulation of the semiconductor.

4.6. Summary

This chapter forms the basis for the semiconductor-cell-electrolyte CPD investigations that will be presented next in Chapter 5. The CPD apparatus has been properly assembled and calibrated while several preliminary measurements have allowed one to define the possible challenges that may be encountered when performing CPD measurements and to find suitable solutions. Samples for the cell-semiconductor interaction studies have been selected, described, and their electronic behavior upon chemical charging has been analyzed via CPD measurement. Thanks to the results presented in this and in previous chapters we are now ready to implement semiconductor-cell-electrolyte CPD measurements for the investigation of electronic interactions between the biological world and semiconducting materials.

Chapter 5. CPD Studies of the Semiconductor-Cell-Electrolyte System

At this stage of the research SiC crystals with atomically-flat surfaces have been prepared and selected (Chapter 2, § 4.2.2), their surfaces have been characterized morphologically (2.2.1, 2.3.1), crystallographically (2.2.3), chemically (2.2.3, 3.2), and electronically (4.3-5), while their biocompatibility has been largely assessed (Chapter 3). Since all of the requirements listed in Chapter 1 for the successful investigation of hybrid systems have been discussed and fulfilled, we can now describe the results obtained in the final part of this research.

Understanding how the presence of charges on the surface of a biological cell may affect the electronic band bending in a semiconductor would open a wide range of possibilities in the bio-sensing application area and is therefore one of the primary objectives of this work. In fact, up to date, even though the possibility of electronic communication between electrogenically active cells and semiconductors has been proved by cell electrical recordings operated by transistors [122-125], the mechanisms underlying the electronic communication have not been studied. In this chapter we report the methodology and results that we used in the attempt to describe the effect of the cell charge on the energy bands of a semiconductor. For this purpose, we selected dark/light non-contacting CPD measurement as a suitable technique capable of detecting the band bending at a semiconductor surface without discharging it (§ 1.4). However, as we already pointed out in the introductory section of Chapter 4, the necessary presence of

liquid in the CPD measurements we aim to perform highly complicates these measurements. Nonetheless, thanks to the accurate calibration of our CPD system, we report how we were able to obtain valid and repeatable CPD readings from semiconductor surfaces immersed in an electrolyte. Unfortunately, the results obtained from the CPD investigations of cell-semiconductor systems reported in this chapter did not display any measurable influence of the cell charge on the semiconductor band bending. However, the models and explanations used to describe the obtained results are of primary importance for the future implementation of successful techniques for the investigations of cell-semiconductor electronic interactions. Indeed in Chapter 6 we will discuss the possibilities to continue this work, based largely on the knowledge gained from the results presented hereafter.

Specifically, in this section we first describe the experimental procedures developed for performing CPD measurements of semiconductor-cell-electrolyte systems (§ 5.1). Subsequently, we report the CPD characterization results obtained during investigations of semiconductor-electrolyte interactions (§ 5.2). In this section, in addition to SiC, which was selected at the beginning of this research as the ideal substrate material for our CPD studies (§ 1.2), Si substrates were also used (i.e., the ones selected and electronically characterized in Chapter 4). The results presented confirm that SiC is preferred over Si for the CPD measurements we intend to perform. In § 5.3 we explain the reasons that brought us to choose the cell lines used in this chapter for cell-semiconductor electronic interaction studies. Subsequently, in § 5.4 we present the results obtained studying, via CPD, the effect of adherent cells on semiconductor surfaces. Interestingly, no electronic effect operated by the cells on the energy bands of the semiconductor was observed. For

this reason we modified the approach and used, in the CPD investigations, non-adherent cells that are well known for their electronic charge: red blood cells (RBC or erythrocytes). In this instance, an evident cell-concentration-dependent band bending was observed on SiC surfaces (§ 5.5). Unfortunately, the apparent positive result obtained using RBCs was most likely caused by an optical effect associated with the nature of the erythrocytes rather than by their electronic charge. Theoretical models and possible explanations for the results reported in sections 5.2, 5.4 and 5.5 are presented in § 5.6.

5.1. Experimental procedure for CPD measurements of the semiconductor-cell-electrolyte system

There are several steps that have to be performed to prepare the complex semiconductor-cell-electrolyte system which is going to be measured via CPD. First, each selected semiconducting sample has to be cleaned with an optimized procedure which eliminates any organic residue from its surface and which leaves the semiconductor in a depleted condition (§ 5.1.1). Second, the sample has to be processed in a way that allows one to culture/deposit cells on its surface and that, at the same time, ensures good electrical contact of the sample backside with the metallic chuck (§ 5.1.2). Third, cells have to be seeded/cultured on the semiconductor surface (§ 5.1.3). Finally, the CPD measurements can be performed (§ 5.1.4). In this section we describe all the procedures developed for each part of this experiment.

5.1.1. Chemical preparation

Each sample that was used for cell-semiconductor interaction studies presented bio-residue on its surface at the end of the experiment. Since throughout this work we re-use

the same samples over and over to ensure result repeatability and to lower experimental cost, it is of fundamental importance to use a cleaning technique which ensures complete bio-residue removal. Moreover, the chemistry used in the cleaning procedure has to leave the semiconductor in a depleted condition since a depleted electronic status increases the sensing potentiality of the semiconductor. The cleaning procedure that was selected for this purpose was Piranha followed by HF. In fact, as we demonstrated in § 3.3, Piranha is the only chemical procedure that was found effective in complete bio-residue removal. The HF dip is used as a final step to ensure oxide removal (§ 3.1.1) and to generate a depletion region in the semiconductor surface (§ 4.5.2). Specifically, the applied procedure was constituted by the following steps: immersion in Piranha (2:1 H_2SO_4:H_2O_2) for 5 minutes; de-ionized (DI) water rinse; dip in hydrofluoric acid solution (50:1 H_2O:HF) for 2 minutes; thorough DI water rinse. Sterilization of the samples via ethanol dip was considered unnecessary for two main reasons: 1) in many experiments cells were only deposited on the semiconductor surface and not cultured, the CPD measurements being immediately performed; 2) the strength of the Piranha and HF cleaning applied before cell deposition were found to be enough to avert the danger of bacterial contamination even for the longest culturing time which was fixed at 24 hours. It should be mentioned that in all of the experiments performed and that will be reported in the next sections we never encountered contamination problems.

5.1.2. Sample processing

In the final CPD measurement that we aim to perform a Monroe probe will be lowered on a semiconductor (typically SiC) whose surface, wet by an electrolyte, presents deposited/cultured cells and whose backside forms a quasi-ohmic contact with

the metallic chuck of the CPD apparatus (§ 1.4.2). Therefore, the sample should be processed to ensure good electrical backside contact and a clean platform for cell culture/deposition. Obviously, since cells survive in aqueous environments and since aqueous environments oxidize semiconductors, a first requirement is to physically separate the platform for cell culture (e.g., sample surface) from the sample backside so that the electrolyte (e.g., cell media) will not come into contact with it. Moreover, a way has to be found to avoid the sample backside oxidation which would surely take place for experiments where incubation of the samples in an atmosphere with 95% of humidity was required. For this purpose, prior to cell deposition, the samples were processed in two different ways. This gave rise to two different experimental approaches that we have defined as the 'free-standing' sample approach and the 'PEEK' approach. In the free standing sample approach the liquid was confined in the top part of the sample by bordering the semiconductor edges with epoxy (i.e., crystal glue, see Fig. 5.1(a)) while Cu-Au contacts, evaporated on the backside of the sample, provided a stable electrical contact with the chuck. In the PEEK approach a machinable, autoclavable and biocompatible sample holder, made with Polyetheretherketone (PEEK), was designed and fabricated. The backside of the sample was epoxied to the PEEK container while a hole with threads machined in the holder allowed electrical back-side contact via a brass screw (Fig. 5.1(b)). The seal provided by the epoxy around the backside contact significantly slowed down the semiconductor oxidation process that took place every time the sample and the sample holder were stored in the incubator for cell culturing.

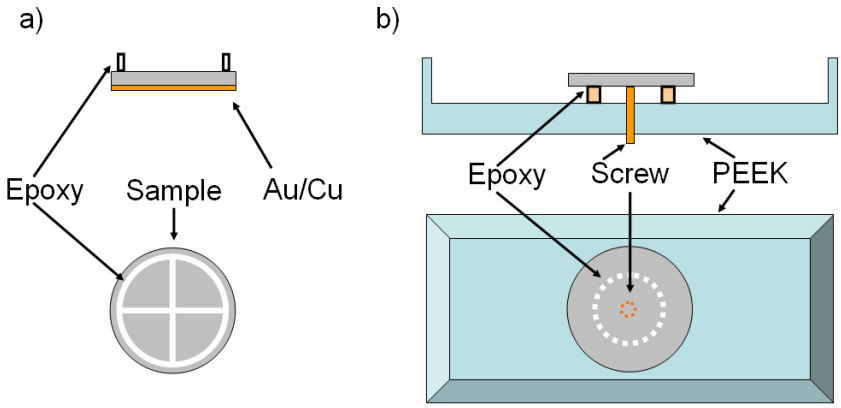

Figure 5.1. Sample configuration for cell-CPD experiments showing (a) the free-standing sample approach and (b) the PEEK approach. In (a) the subdivision of the samples in parts with smaller area is represented.

For experimental consistency cells and media (and media only for the experiments with electrolytes reported in § 5.2), were deposited on a sample with an area of 4.9 cm^2. For the PEEK experiments samples with this area were used while for the free-standing experiments samples with larger areas were partitioned using epoxy as described earlier (Fig. 5.1(a)).

The two methods presented different advantages and drawbacks. In the free-standing sample approach the disadvantage was the toxicity of the epoxy which was in close contact with the cells while the advantage was quick sample processing. The drawbacks of the PEEK approach were longer processing times and higher costs while the positive point was the biocompatibility of the sample holder. The morphology of B16 cells cultured on 3C-SiC samples processed in the two different ways is shown in Fig. 5.2. As expected, a higher quality cell morphology was found for the sample mounted on the PEEK sample holder (Fig. 5.2(a)). Cells cultured on the free-standing samples and located at sufficient distance from the epoxy displayed morphologies totally comparable

to the ones of Fig. 5.2(a). However, we observed a poor morphology (i.e., minimization of the adhesion area) for cells cultured in the vicinity of the epoxy, as expected (Fig. 5.2(b)). For this reason, CPD measurements of free-standing samples were performed far away from the epoxy, in areas where the cell morphology was equivalent to that observed on samples mounted in the PEEK holder.

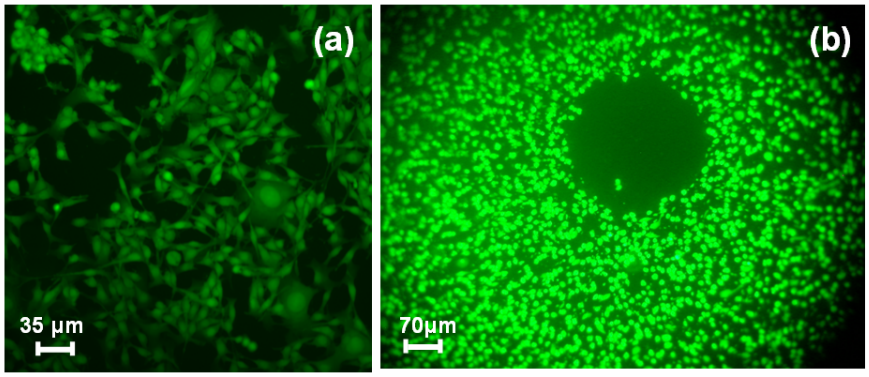

Figure 5.2. Cell morphology on (a) a sample mounted within the PEEK sample holder, (b) a free-standing sample in the vicinity of an epoxy drop (b). Note the different scale bar in the two fluorescence microscopy images. In (b) an epoxy drop with a rounded area was present in the centre resulting in non-adherent cells in this region.

The choice of using two different experimental approaches eliminated the possibility that systematic errors in the approach chosen would affect the final results. Both the approaches were successfully used and yielded the same results as will be shown in the next sections.

5.1.3. Cell deposition / culture

After the samples were cleaned and processed (e.g., mounted in the PEEK container or bordered with epoxy), cells were either deposited (i.e., short-time experiments) or cultured (e.g., 24 hour experiments) on the semiconductor surface. The mammalian cells used in our studies were: B16-F10 mouse melanoma, HaCaT human keratinocytes and

pig red blood cells (RBC or erythrocytes). While the first two listed cell lines are epithelial cells that need to adhere to the substrate to survive, RBC will not adhere to the SiC substrate. Therefore, two different experimental procedures were designed for the two cell categories. In the adherent cell experiment cells were deposited on each sample at a density that allowed complete coverage of the sample within the first 24 hours. McCoy's Modified Medium and Dulbecco's Modified Eagle's Medium (DMEM), both supplemented with 10% FBS, were the culture media used for the B16 and the HaCaT cells, respectively. Typical seeding densities were of 10×10^4 cells / cm^2. After seeding, cells and samples (either epoxied to the PEEK container or free standing) were incubated at 37 ºC from a minimum of 4 hours (minimum time to ensure cell adhesion to the substrate) to a maximum of 24 hours in an atmosphere containing 5% CO_2 and 95% relative humidity. In preliminary experiments, CPD measurements were also performed after incubation times longer than 24 hours but they were found to be highly unrepeatable and hence will not be reported. In the RBC experiments, erythrocytes were collected from pig blood after centrifugation at 200 ×g and subsequent plasma pellet extraction. Subsequently, they were re-suspended at a high concentration in phosphate buffered saline (PBS). The estimated density in PBS was 6.4×10^9 cells/ml. In this case the CPD measurements were performed immediately after cell deposition on the semiconductor surface. As mentioned in § 5.1.2, all the seeding densities reported in this section refer to a sample area of 4.9 cm^2.

5.1.4. Experimental procedure for CPD measurements of semiconductor-cell-electrolyte systems

The procedure used to measure the surface potential (Φ_s) of a semiconductor immersed in an electrolyte and with adherent cells cultured on top was identical to the one reported in § 4.1.3. Steps (1)-(10) were performed immediately after the sample (either free-standing or within the PEEK container) was removed from the incubator and the media was reduced to a minimum amount. To ensure that differences in media pH (e.g., media becomes acidic over time because of cell byproducts) would not influence the surface potential of the sample under study, the culturing media was changed frequently and in particular 1 hour before the execution of the CPD measurements. In this occasion the new media that was added did not contain fetal bovine serum (FBS) since it has been shown in electrophoretic measurements that the presence of FBS may modify the charge associated with cells [25].

For RBC studies the free-standing approach was adopted because of its short processing time. The drawback of this approach, which was represented by the toxicity of the crystal glue, was not an issue in this case since cell culturing on the semiconductor surface was not required and because of the very short duration of the experiment. For CPD measurements of the semiconductor-RBC-electrolyte system a different procedure, which is reported below, was designed.

1_{rbc}) Perform steps (1)-(10) reported in § 4.1.3 for the free-standing sample

2_{rbc}) Add 100 μL of PBS on the sample surface

3_{rbc}) Perform steps (1)-(10) reported in § 4.1.3 for the sample-electrolyte system (taking care not to immerse the Monroe probe in the liquid)

4_{rbc}) Add 1% of RBC concentrated solution

5_{rbc}) Perform steps (1)-(10) reported in § 4.1.3 for the sample-RBC-electrolyte system (taking care not to immerse the Monroe probe in the liquid)

6_{rbc}) Repeat steps (4_{rbc}) and (5_{rbc}) for higher concentrations of RBCs

The surface potential values reported in the next sections are expressed as mean ($\overline{\phi_S}$) and calculated from a two measurement distribution. The standard deviation values for measurements in liquid were similar to those of measurements in air, typically below 15 mV.

5.2. Electrolyte semiconductor systems

Before studying the effect of cells on semiconductor band bending, we investigated the modification in surface potential that the presence of an electrolyte would cause on SiC and Si surfaces. The chemical behavior of Si in aqueous solution has already been investigated by several past studies [13, 14, 48, 102], which facilitates the understanding of the results that will be reported. All the semiconductor-electrolyte interaction studies were performed using the free-standing sample approach, repeated several times (i.e., the results reported below within the tables are representative values), and depositing 100 μL of liquid on the sample surface (unless otherwise specified). Almost in every instance the electrolyte spread in a hydrophilic fashion over the sample surface. If not, a pipette tip was used to obtain a uniform coverage of liquid below the measuring electrode. In the

presence of non-flat, high contact angle media drops on the surface (i.e., only obtained for one semiconductor-electrolyte combination, reported below), no valid CPD measurements could be performed.

First, we evaluated the behavior of n-type Si(111) and 3C-SiC(001) in water and in sucrose solution by adding 100 μL of these liquids over the sample surfaces using a pipette. Before being in contact with the electrolyte, both the samples presented the typical depletion 'steady state' described in § 4.3. CPD measurements were taken at several time intervals: immediately after the liquid deposition, after 5 minutes, after 10 minutes and finally after liquid removal. We observed a different time-dependent behavior for Si and SiC CPD values. In both cases aqueous solutions tended to reduce the initial depletion state, obtained after HF treatment, and caused the bands to shift towards a flat-band condition. On Si this was more evident being that the initial depletion region is thinner (e.g., in general smaller band bending amplitudes were observed for Si after HF treatment probably because of the better H-passivation, see § 4.5.2). However, we observed that longer times were required for the Si sample to reach its final Φ_s value while for SiC the transient was immediate (see Table 5.1). Also, after water removal, the Φ_s of SiC tended to come back towards the initial depletion value while Si remained in a basically flatband condition.

Table 5.1 Effect of water on the surface potential of Si(111) and 3C-SiC(001) as measured via CPD.

	Φ_s (mV) of bare sample	Φ_s (mV) after H_2O at 0''	Φ_s (mV) after H_2O at 5'	Φ_s (mV) after H_2O at 10'	Φ_s (mV) after H_2O removal
n-type Si(111)	-135.5	-50.2	-35.1	-7.7	-10.1
n-type 3C-SiC(001)	-253.3	-117.2	-101.1	-108.3	-184

Even though Table 5.1 reports only the results obtained with water, completely similar results were obtained for the sucrose solutions. The flatband condition observed on Si is probably justified by the smaller initial $|\Phi_s|$ value. However, the fact that Si surfaces did not tend to recover to the initial Φ_s value after liquid removal indicates that whatever caused the quasi-null observed Φ_s was still affecting the dry surface. It is known that when Si is immersed in water a passivating oxide forms within the first 5-10 minutes [13]. Therefore, rather than an effect associated with the redox couples present in the liquid, the flatband condition observed is most probably related to the presence of the oxide that grows on the surface during the sample immersion in liquid. Very likely surface states which develop at the Si-oxide interface cause Fermi level pinning and yield to the observed behavior. The same quasi-null Φ_s was observed also when different electrolytes (e.g., culturing media, phosphate buffer saline (PBS)) were contacting the Si surface. Therefore, whether the final Φ_s observed for Si was due to Fermi level pinning or to a complete surface passivation, it is impossible to use Si as a substrate for cell-semiconductor electronic interaction studies.

On the other hand, the existence of a still measurable depletion region on SiC surfaces contacting aqueous solutions encouraged us to proceed with these studies. The

electrolytes that were used in the experiments with cells, namely McCoy, DMEM and PBS (§ 3.1.2), were deposited on the selected SiC samples with different polytypism and different majority carrier types (e.g., n- or p-type) (§ 4.2.2). CPD measurements of the semiconductor-electrolyte systems were taken a few seconds after the liquid came into contact with the semiconductor and repeated within the first 10 minutes. Also in this case, no time dependent behavior was observed for the surface potential of SiC samples contacting electrolytes. Typical results obtained for 100 μL of deposited McCoy culturing media and PBS are reported in Tables 5.2 and 5.3, respectively. However, preliminary studies demonstrated that the amount of liquid per surface area was irrelevant within reasonable concentrations (e.g., 50-150 μL over an area of 4.9 cm^2, see Table 5.4). The results obtained for DMEM culturing media were totally comparable to those in Table 5.2.

Table 5.2 Effect of McCoy culturing media on surface potential of SiC and Si surfaces as measured via CPD. Values for Si reported for comparison purposes only.

Sample	Si(111) n-type	Si(111) p-type	3C-SiC(001) n-type	6H-SiC(0001) n-type	6H-SiC(0001) p-type
Φ_s (mV) of bare sample	-228.4	113.1	-301.9	-337.6	287.7
Φ_s (mV) with 100 μL of McCoy	-16.1	26.1	-169.7	-131.4	180.8

Table 5.3 Effect of phosphate buffer saline (PBS) on surface potential of SiC and Si surfaces as measured via CPD. Values for Si reported for comparison purposes only.
* not measured
£ double values reported due to conflicting behavior in repeated measurements

Sample	Si(111) n-type	Si(111) p-type	3C-SiC(001) n-type	6H-SiC(0001) n-type	6H-SiC(0001) p-type
Φ_s (mV) of bare sample	-129.8	100.5	-244.7	-354.2	222.7 / 214.2£
Φ_s (mV) with 100 μL of PBS	-14.9	0.8	-174.1	– *	221.6 / 364.7£

Table 5.4 Effect of different amounts of McCoy culturing media on surface potential of 3C-SiC(001) as measured via CPD.

	Φ_s (mV) of bare sample	Φ_s (mV) with 50 μL of McCoy	Φ_s (mV) with 100 μL of McCoy	Φ_s (mV) with 150 μL of McCoy
3C-SiC(001)	-301.9	-169.7	-165.7	-171

In Tables 5.2 and 5.3 surface potentials of n- and p-type Si before and after electrolyte deposition are reported for comparison purposes and also to confirm what was reported in Table 5.1. It is evident that the final quasi-null Φ_s value displayed by Si surfaces after electrolyte deposition is independent of the amplitude of the initial Φ_s value (e.g., even an initial Φ_s value as large as -228.4 mV approaches 0 mV when the surface is in contact with water). This indipendency strongly supports the hypothesis of a Fermi level pinning operated by surface states developing at the oxide-semiconductor interface. The presence of surface states at such a high density to cause Fermi level pinning on Si rather than on SiC surfaces could be due to the fact that Si samples were not prepared via H-etching and that they were not flat at an atomic level (see § 4.2.2).

It appears, that both McCoy and PBS tend to have the same effect of reducing the value of $|\Phi_s|$ (i.e., bands shifting away from depletion) for all the SiC polytypes studied, with the exception of PBS on p-type 6H-SiC(0001). For n-type 6H-SiC(0001), Φ_s values could not be calculated because of the hydrophobic reaction that these substrates had with PBS: all the attempts to deposit any amount of PBS on the surface resulted in the formation of a high contact angle drop that made it impossible to perform CPD measurements. On the other hand the result obtained for p-type 6H-SiC were conflicting: either no effect on band bending or a shift of bands toward depletion upon PBS exposure was observed. These results will be modeled in § 5.5.

5.3. Cell line selection and properties

For the cell-semiconductor electronic interaction studies three different cell lines with different characteristics were chosen. Unfortunately, to date, no clear estimation of the cell charge of adherent mammalian cells has been reported, with the exception of RBCs. This is one of the main reasons why our investigations are truly pioneering and, at the same time, particularly challenging. The only technique that currently reports the evidence of the existence of a net cell surface charge is electrophoresis, which determines the mobility of cells in aqueous solution upon application of an electric field between two electrodes. Thanks to these studies it is nowadays accepted that mammalian cells display a negative surface charge. Once the electrophoretic mobility is defined, it is possible to calculate the potential at the cell shear plane (i.e., zeta potential (ζ)) by using the von Smoluchowski equation $\zeta = 4\pi\eta\nu/D$ where η is the fluid viscosity, ν is the electrophoretic mobility of the particle (i.e., cell) and D is the dielectric constant of the fluid [6, 24]. Clearly, the value of ζ by itself is meaningless if not associated with a pH and an

electrolyte. The von Smoluchowski equation has been long debated in the past and presents major interpretative difficulties [126]. The first issue in the adoption of this equation, for the determination of the zeta potential, resides in the fact that the relation was created for spherical particles whereas cells generally deviate from this assumption [6]. Also, this equation seems to be reliable only for zeta potential values < 120 mV and electrolytes containing more than 10^{-3} molar salt [127]. However, since it has been reported that erythrocytes made spherical by saponin have electric mobility, within the limit of experimental error, identical to the ones of the disc-shaped cells suspended in the same buffer, the von Smoluchowski equation has been largely adopted in the past for the determination of ζ of erythrocytes [6, 24, 128]. Typical values of ζ for erythrocytes vary between -15 mV and -30 mV, depending on the electrolyte of suspension [6, 24, 128, 129]. In general, for small values of ν, the Debye approximation for the calculation of an erythrocyte charge density (σ) can be used and the relation between ζ and σ is straightforward: $\sigma = D\zeta/4\pi$. As is intuitive, high electrophoretic mobilities lead to high zeta potentials and, therefore, are indicative of a high cell surface charge. Thanks to electrophoretic experiments and theoretical calculations performed using the aforementioned equations, the surface charge density of mammalian RBCs has been estimated to range between 63 and 188.8×10^{-8} C/cm^2 [6, 128].

On the other hand, values of ζ for other mammalian cells have not been calculated due to their incompatibility with the von Smoluchowski equation. Therefore, all knowledge about the possible charge associated with a specific cell comes from chemical studies. From a chemical point of view, it is well known that the negative charge of mammalian cells is mainly caused by sialic acid, hyaluronic acid and chondroitin sulfate

which are all present in the external part of the cellular membrane [130]. In particular, sialic acid is the only major constituent with negative charge in RBCs. Also, medical reviews in the past have reported results that tend to display higher electrophoretic mobilities for malignant cells [7]. The reduction of electrophoretic mobility observed for different malignant cell lines upon X-irradiation tends to confirm this belief [5]. Known charge-related characteristics of the cells used in this work, together with a motivation for their use, are summarized below.

1) *HaCaT human keratyinocytes*. No known surface charge density. Estimated mobility comparable to those of healthy mammalian cells and therefore largely lower than erythrocytes mobility in saline solutions [7]. Fast growing cell line, good for preliminary experiments.

2) *B16-F10 mouse melanoma cells*. No known surface charge density. Electrophoresis experiments performed for another B16 sub-line (B16-C2W) report mobility values comparable to those measured for human erythrocytes (e.g., $\mu = -1.05 \mu s^{-1} V^{-1} cm$) [5]. This could lead to the assumption that the σ is similar for the two cell lines. However, an approximately 7 times larger diameter for the mouse melanoma cells (i.e., 40 μm for B16 vs. 6 μm for RBC) complicates the matter. Moreover, aggregation of B16 in clusters is often observed which may lead to the conclusion of limited electrostatic cell-to-cell repulsion and therefore a lower σ than the one measured for RBCs. Malignant cell line, possible higher negative surface charge with respect to HaCaT. Fast growing cell line.

3) *Pig RBCs*. Zeta potential and surface charge density in saline estimated to be roughly -13 mV and 11.2×10^{-7} C/cm^2, respectively [6, 128]. Possibility of obtaining

significant electronic effect on the energy bands of SiC semiconductors. In fact, the total charge necessary to significantly deplete a 4H-SiC epilayer is on the order of 10^{-7}-10^{-8} C/cm^2. Depositing a monolayer of RBCs above the semiconductor surface would generate a uniform charge density well above the minimum value necessary to generate a measurable band bending on SiC (e.g. 11.2×10^{-7} C/cm^2 > 10^{-7} C/cm^2, which is required to completely deplete a 4H-SiC epilayer) [45]. Easy to obtain in large quantities.

5.4. CPD investigations of adherent mammalian cells-SiC systems

§5.1 perfectly described the protocols used in the different stages that characterize CPD investigations of cell-semiconductor systems. In this section, before reporting the results obtained in the case of mammalian adherent cells, we will first describe the adopted experimental approach. In these experiments, when using the PEEK approach, we first evaluated the surface potentials of two identical samples after the cleaning process ($\Phi_{s1,2}$ in Fig. 5.3), and then we probed whether the adopted sample processing technique (e.g., epoxy to PEEK in this case, § 5.1.2) had an effect on these values ($\Phi_{s1',2'}$ in Fig. 5.3). We always observed that the sample processing technique did not modify the surface potential values measured before processing ($\Phi_{s1,2} = \Phi_{s1',2'}$). Subsequently, B16-F10 mouse melanoma and HaCaT cells were deposited, as described in § 5.1.3, on only one SiC substrate and cultured for different times ranging from 4 to 24 hours. The other sample was incubated only with culturing media (e.g., no cells) for the same amount of time. The CPD measurements were performed at regular intervals within this time range and the readings obtained for the substrate with cultured cells ($\Phi_{s1''}$) were compared to the one obtained for the identical substrate (always cut from the same original wafer and treated in an identical fashion) which was exposed to the electrolyte but no cells ($\Phi_{s2''}$).

In particular, the difference between the surface potentials measured when cells+media (or media only) were present and immediately before cell seeding (e.g., after processing) was calculated for each sample ($\Delta_{1,2} = \Phi_{s1'',2''} - \Phi_{s1',2'}$) and compared. Fig. 5.3 contains a flow chart describing the experimental procedure used when adopting the PEEK approach. For the free-standing approach the only difference was that typically half of a two inch sample (i.e., area A = 9.8 cm^2) was partitioned in two subdivisions (similarly to Fig. 5.1(a) but only for a half wafer) displaying an area of 4.9 cm^2 each: one half was seeded with cells and media and the other only with media. Therefore, we used one sample divided in two parts instead of two identical samples. The latter approach eliminated the possibility that two different samples would undergo other surface modifications than the ones caused by cells when stored separately in the incubator.

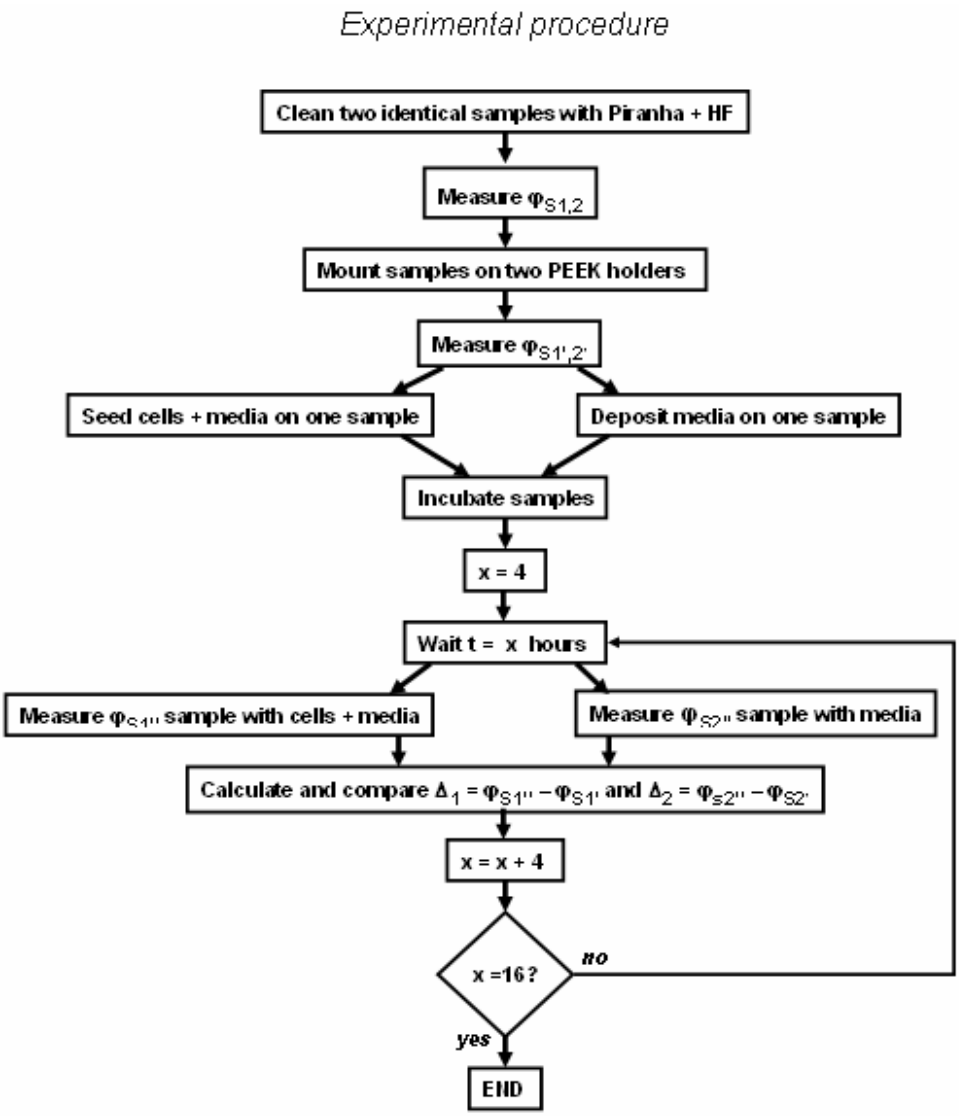

Figure 5.3. Flow chart describing the experimental procedure adopted to investigate the effect of cell charge on semiconductor band bending. $\Phi_{s1,1',1''}$ ($\Phi_{s2,2',2''}$) are the surface potentials for the sample with cells+media (media only); Δ_1 (Δ_2) is the surface potential difference between the sample with cells+media (media only) and after processing. The procedure reported is for the PEEK approach. For the free-standing approach all the steps are the same only, instead of using two identical samples, we operate on two parts of the same sample partitioned by epoxy.

Typical surface potential values obtained for B16 and HaCaT cells are reported in Tables 5.5 and 5.6, respectively. In Table 5.5 results are reported for 24 hour inspection of 3C-SiC(001) samples mounted on PEEK. However, they were also confirmed for n-

and p-type 6H-SiC(0001), using the free-standing sample approach, and for different incubation times. The experiment was repeated at least 10 times yielding always the same results. The media used for this cell line was DMEM throughout the experiment. Fresh DMEM (without FBS) was replaced for both the samples, with seeded cells and without, one hour before the CPD measurements as described in § 5.1.4. The results reported in Tables 5.5 and 5.6 clearly show that no measurable differences in surface potentials were observed between the samples with cells+media and the samples with only media.

Table 5.5 Non-detected electronic interaction between HaCaT cells and 3C-SiC(001) after 24 hours from seeding (standard deviation $\sigma < 15$ mV).

Sample ID	Φ_s (mV) after cleaning + sample processing	Φ_s (mV) of sample w/ media only	Φ_s (mV) of sample w/ media and cells	Δ (mV)
n-type 3C-SiC USF-06-271.1: media + cells	-211.4 ($\Phi_{s1'}$)	–	-109.6 ($\Phi_{s1''}$)	101.8 (Δ_1)
n-type 3C-SiC USF-06-271.2: media only	-207.6 ($\Phi_{s2'}$)	-111.5 ($\Phi_{s2''}$)	–	96.1 (Δ_2)

It appears evident from Table 5.5 that no significant differences were observed between the Δ values calculated for the two samples. In fact, $\Delta_1 - \Delta_2 = 5.7$ mV which is within the standard deviation range for these measurements (e.g., 0 mV $< \sigma <$ 15 mV, as reported in § 5.1.4).

Table 5.6 illustrates the typical values obtained on different polytypes of SiC processed with the free-standing sample approach after 4 hours from B16-F10 cells seeding. The same results were obtained also when using the PEEK approach and after different incubation times.

Table 5.6 Non-detected electronic interaction between B16-F10 cells and n-type 3C-SiC, n-type 6H-SiC and p-type 6H-SiC 4 hours after seeding ($\sigma < 15$ mV).

	Φ_s (mV) after cleaning + sample processing	Φ_s (mV) of sample w/ media only	Φ_s (mV) of sample w/ media and cells	Δ (mV)
n-type 3C-SiC USF-07-039a: media + cells	-276.1 ($\Phi_{s1'}$)	–	-175.4 ($\Phi_{s1''}$)	100.7 (Δ_1)
USF-07-039b: media only	-284.4 ($\Phi_{s2'}$)	-178 ($\Phi_{s2''}$)	–	106.4 (Δ_2)
n-type 6H-SiC CO24a: media + cells	-323.5 ($\Phi_{s1'}$)	–	-594.6 ($\Phi_{s1''}$)	-271.1 (Δ_1)
n-type 6H-SiC CO24b: media only	-349.8 ($\Phi_{s2'}$)	-614 ($\Phi_{s2''}$)	–	-264.2 (Δ_2)
p-type 6H-SiC BQ02a: media + cells	215.6 ($\Phi_{s1'}$)	–	252.6 ($\Phi_{s1''}$)	37 (Δ_1)
p-type 6H-SiC BQ02b: media only	232.2 ($\Phi_{s2'}$)	281.7 ($\Phi_{s2''}$)	–	49.5 (Δ_2)

Also in this case, no statistically significant differences were observed between the Δs calculated for each pair of samples of the same polytype. Therefore, no electronic interaction of adherent B16-F10 mouse melanoma cells with the SiC samples was observed.

In every experiment, after the 24 hour CPD measurements were taken, all samples with seeded cells were inspected via fluorescence microscopy to evaluate cell morphology and coverage. We observed satisfying morphologies and a coverage of at least one monolayer in all cases. The obtained results are justified and modeled in § 5.6.

5.5. CPD investigations of RBC-SiC systems

The CPD studies performed for B16-F10 melanoma and HaCaT cells on SiC surfaces did not display an evidence of band bending on the semiconductor surface. As we already mentioned in § 5.3, the surface charge density associated with these adherent cells may not be sufficient to induce a measurable effect on the electronic status of the semiconductor. On the other hand, the presence of a significant, and therefore easily measurable, electronic charge on RBCs and the fact that these cells are obtainable in large numbers brought us to choose them as an alternative, and hopefully more successful, cell line for the CPD experiments.

We started the RBC experiments by depositing, on bare free-standing SiC samples already fully characterized via CPD, only the electrolyte for our experiments (PBS), repeating what was done in § 5.2, only this time not for modeling purposes but to obtain a specific surface potential value for each sample to compare with the ones obtained after cell deposition. After this, we proceeded by adding gradually increasing densities of RBCs and by measuring, after each addition of cells, at least two surface potential values to ensure statistical relevance of the data (as done in the rest of this chapter, e.g. § 5.1.4). The amount of RBC concentrated solution (estimated cell density: 6.4×10^9 cells/ml, (§ 5.1.3)) deposited via pipette each time were 1, 10, 20 and 50% of the PBS solution. The experiment was performed on at least three selected samples for each polytype and was repeated two times.

The results obtained apparently showed a strong dependence of the surface potential on the amount of cells present in solution and, in all cases, the bands of the semiconductor appeared to shift away from depletion and towards flatband. The observed

surface potential behavior is plotted in Figures 5.4, 5.5 and 5.6 for n-type 3C-SiC, n-type 6H-SiC and p-type 6H-SiC, respectively.

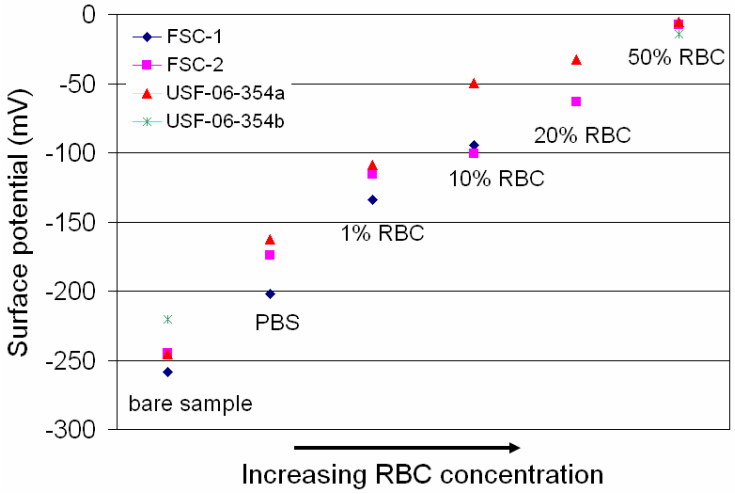

Figure 5.4. Measured CPD surface potential for increasing amounts of RBCs for different 3C-SiC(001) samples. The surface potential values of the bare samples and of the samples with PBS are also reported for comparison.

As is evident from Fig. 5.4, the behavior of the band bending upon PBS deposition was consistent with what was reported in § 5.2. A significant variation in the measured surface potential was observed even after addition of only 1% of RBC concentrated solution in PBS. However, this major effect could be easily justified by the fact that the total amount of cells deposited in this case was significantly high: approximately 6.4×10^{6} cells were present in the saline at the moment of the measurement. When adding an amount of cells equivalent to roughly 3.2×10^{8} cells (50% RBC in Fig. 5.4) the calculated surface potential value approached zero.

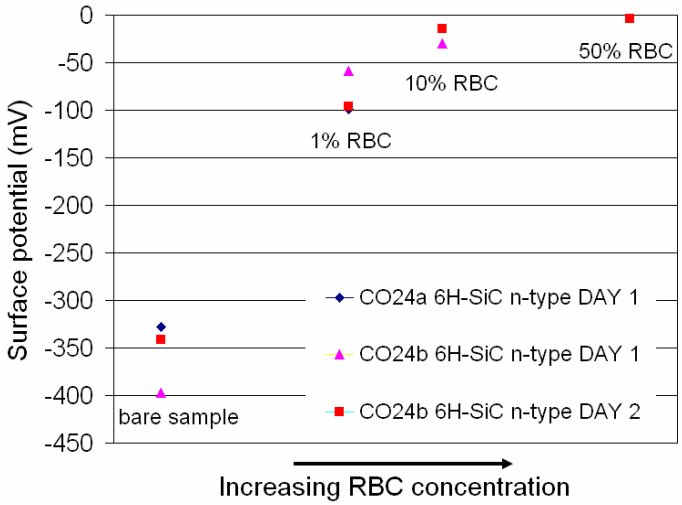

Figure 5.5. Measured CPD surface potential for increasing amounts of RBCs for two n-type 6H-SiC(0001) samples and data repeatability in two different experiments (DAY 1 and DAY 2) as calculated for one sample. The surface potential values of the bare samples are reported for comparison.

Very similar results were observed for n-type 6H-SiC (Fig. 5.5). However, in this case, as explained in § 5.2, we could not monitor the effect of PBS on the electronic status of the semiconductor because of the high contact angle of the PBS drop with n-type 6H-SiC and the impossibility to flatten it. However, once the RBCs were added in the solution, we observed a significant change in the electrolyte behavior that, this time, flattened on the semiconductor surface without resistance (i.e., lower contact angle). This was probably due to a modification in the electrostatic interactions between the n-type 6H-SiC surface and the saline buffer once RBCs were added, implying that RBCs were the main cause of the observed modification. In Fig. 5.5 the repeatability of the surface potential values obtained for the same n-type 6H-SiC sample in two different experiments can be also observed.

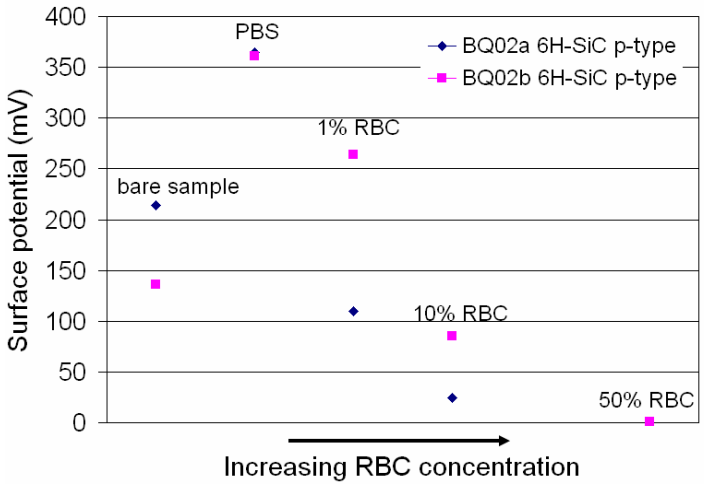

Figure 5.6. Measured CPD surface potential for increasing amounts of RBCs for two p-type 6H-SiC(0001) samples. The surface potential values of the bare samples and of the samples with PBS are also reported for comparison.

As is evident from Fig. 5.6, PBS alone tended to shift the bands of p-type 6H-SiC towards depletion while even the smallest amount of cells drastically changed the trend and apparently shifted the bands away from depletion and towards flatband.

It has to be mentioned that the cause of the quasi-null surface potential observed for SiC samples in the presence of a high number of RBC's (i.e., ~ 3.2×10^{8}) was surely different than the one that generated the quasi-null surface potential on Si surfaces wetted by electrolytes (§ 5.2). In fact, for the SiC-RBC system, we observed that, immediately after PBS-RBC solution removal, the SiC energy bands shifted back towards the initial values that they presented prior to liquid deposition: this indicates that the effect observed via CPD is strictly related to the presence of cells over the surface and not on absorbates or passivating layers forming on the semiconductor surface.

The results reported were repeatable and always consistent. An example of the data repeatability is shown in Fig. 5.7 for two samples of 3C-SiC(001).

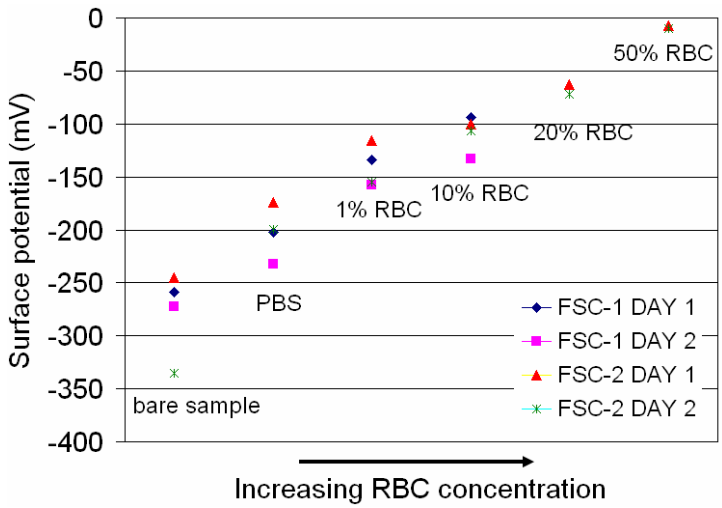

Figure 5.7. Repeatability of the surface potential values calculated for two different 3C-SiC(001) samples from two different experiments (DAY 1 and DAY2).

Although appealing at first glance, the results obtained in the RBC-SiC CPD investigations presented some basic incongruencies. The most striking resides in the fact that RBCs are well known to display a negative total charge: the CPD readings obtained for p-type surfaces agree with this (shift towards accumulation indicates negative charge on the surface), while the results obtained for n-type surfaces suggests the presence of positive charges. Also, the fact that the surface potential values calculated from the readings tended to zero both for p-type and n-type seemed somewhat suspicious. For these reasons, different hypotheses were evaluated to yield satisfactory answers to the observed conflicting behavior. As will be discussed shortly, the results reported in this section do not, unfortunately, describe the effect of cell charge on semiconductors, but are caused by optical issues induced by the erythrocytes.

5.6. Discussion and modeling of the obtained results

In this section we will discuss the results presented in § 5.2, 5.4 and 5.5 and we will also introduce and develop theoretical models which may help to better understand what was observed while performing CPD measurements of the SiC-electrolyte-cell system.

First, we will find reasonable explanations for the results obtained in § 5.2. In order to understand what is reported further in the text the reader should refer to § 1.4. As already discussed in Chapter 1, the semiconductor-electrolyte interface is extremely complex and can be modeled by using the electric double layer model. Maintaining the approximation of negligibility of the Helmholtz capacitance and of the surface state capacitance, which is reasonable in the studied case ($C_{sc} << C_H$ and $C_{sc} >> C_{ss} \rightarrow C_{cpd} = C_{sc}$, § 1.4.5), we can attribute the CPD voltages measured entirely to the excess of charge present in the space charge layer (e.g., $V_{cpd} = V_{sc}$). Recalling the basic principles from § 1.4.4, there are two diffuse layers present at the semiconductor/electrolyte interface: the Gouy layer in the liquid and the space charge layer in the solid. On the solution side, ions distribute over the semiconductor surface at a minimum distance of ~ 3Å (e.g., outer Helmholtz plane) as opposed to the excess charge present in the space charge layer, and then diffuse within the Gouy layer until charge neutrality is reached at a distance $OHP+W_{Gouy}$. It has been estimated that the maximum distance at which charge equilibrium is reached within an aqueous solution, and therefore where the potential drop entirely occurs, is roughly 30 nm [13]. Using the electrical double layer model, the result obtained in § 5.2, where depletion was observed in all instances upon electrolyte deposition on the semiconductor surface, can be schematically represented by an overall negative (positive) charge present on the ionic side for the depleted n-type (p-type).

Schematic representations of the charge distribution in the electrical double layer for n-type SiC and of the associated potential variation in the electrolyte are reported in Fig. 5.8.

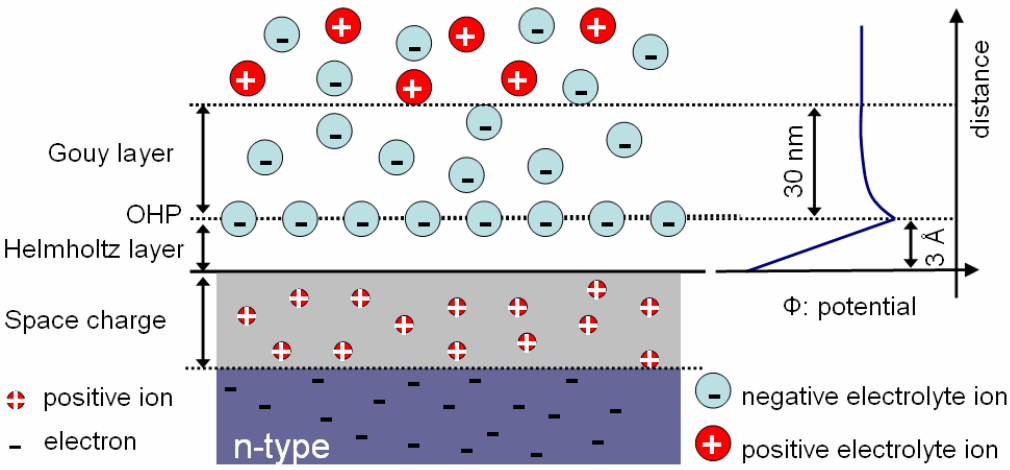

Figure 5.8. Schematic illustration of the electronic status at the n-type SiC/electrolyte interface and relative potential variation in the fluid.

From an energy band diagram perspective, the obtained results indicate that the redox energy levels (E_{RedOx}) of the media used were below the Fermi levels of the n-type semiconductors and above the ones of p-type samples, which is likely (see Fig. 5.9). However, this explanation is not sufficient to describe the obtained results. This is because the Fermi level of n- and p-type SiC samples typically lie only within 200 meV from the conduction band minimum (CBM) and the valence band maximum (VBM), respectively. Therefore, if we assume that the redox energy level of the specific electrolyte lies in the middle of the SiC bandgap this would cause, once the electrolyte and the semiconductor are brought into contact, a shift of the bands of roughly 1 V of magnitude towards depletion both for n-type and p-type samples. The energy band shifts reported in § 5.2 upon electrolyte deposition on the sample surfaces were of much

smaller magnitude (~ 100 mV) and, most important, in almost all the instances (with exception of the p-type SiC-PBS combination) away from depletion, which suggest that other factors, besides the positioning of E_{RedOx}, influence the final CPD readings. Adsorbed ions and charges trapped by surface states at the surface are possible explanations for the decrease in the positive excess charge in the space charge region that otherwise should be observed.

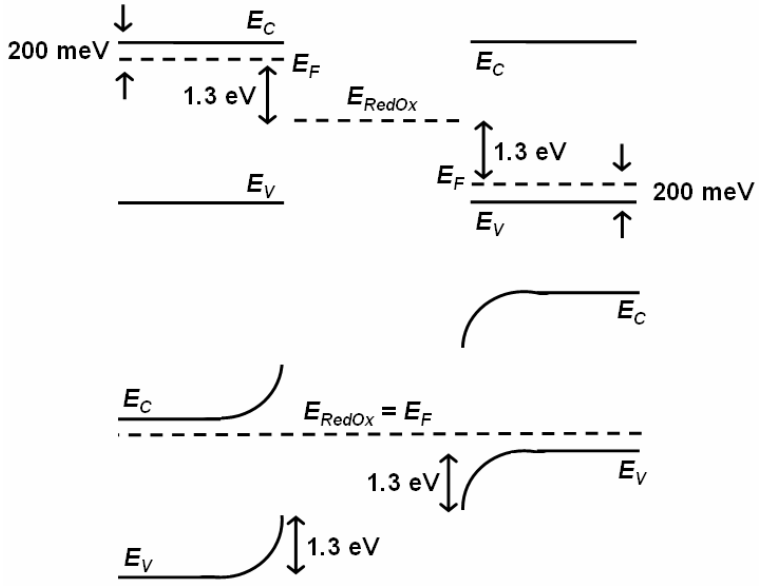

Figure 5.9. Energy band diagram for n-type (LHS) and p-type (RHS) 6H-SiC/electrolyte interface assuming that the Fermi level position in the semiconductor is 200 meV from the conduction and the valence band edges, respectively. Top: band diagrams before contact. Bottom: band diagrams after contact.

Let us now develop a valid model to explain the results obtained in § 5.4. First consider the situation where only the electrolyte is present above the media which will cause a limited surface depletion like the one depicted in Fig. 5.8.

Let us now perturb this situation by introducing a cell. As we already reported in § 5.3, the surface charge of mammalian cells is negative. The cell membrane is highly

insulating [131, 132], which allows us to neglect the influence of the internal charge and to model the cell as a solid body with a charge density, σ, concentrated on its surface. First we will consider the cell floating in the liquid, before cell adhesion to the substrate starts (e.g., time required for a mammalian cell of the lines used to adhere to a substrate is roughly 4 hours). Again, for a solid/liquid interface (cell membrane/electrolyte) we will observe an electrical double layer with an associated potential decreasing with increasing distance from the cell outer membrane. The potential at the cell shear plane is known in the literature as the particle's zeta potential (ζ) as shown in Fig. 5.10.

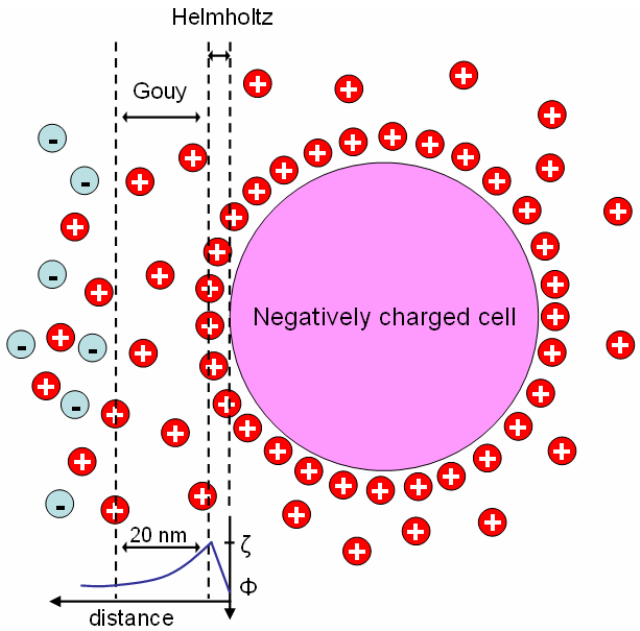

Figure 5.10. Schematic representation of a negatively charged cell suspended in liquid and the system relative potential diagram. Note an electrical double layer forms on the cell surface.

Next we will provide the best case estimation of the zeta potential and of the potential decay (e.g., best case = higher values), which will allow us to develop a model capable of explaining the results presented in § 5.3. For this purpose we will use the data

found in the existent literature relative to red blood cells which, as explained in § 5.3, are most likely the cells with the higher charge density and therefore the ones presenting higher zeta potentials and electrostatic effects in the outer region. Several studies agree in reporting that the zeta potential of RBCs in saline solution is approximately -15 mV and that this potential decays within the first 20 nm from the cell surface [6, 24, 129]. The negatively charged cell surface immersed in media and surrounded by counter-ions and the potential variation associated with it are schematically represented in Fig. 5.10.

Let us now consider the case where the cell adheres to our semiconducting surface. As explained in Chapter 3, mammalian cells adhere to substrates via adhesion plaques which are approximately 15-20% of the cell contact area [131]. With an optimistic assumption we can approximate the contact area of a cell to be 50% of its whole area (see Fig. 5.11), which makes the adhesion plaque 7.5-10% of the total cell area. Apart from the contacts, the average gap between the cell and the substrate surface has been reported to be in the range of 50-150 nm [131]. The situation is schematized in Fig. 5.11.

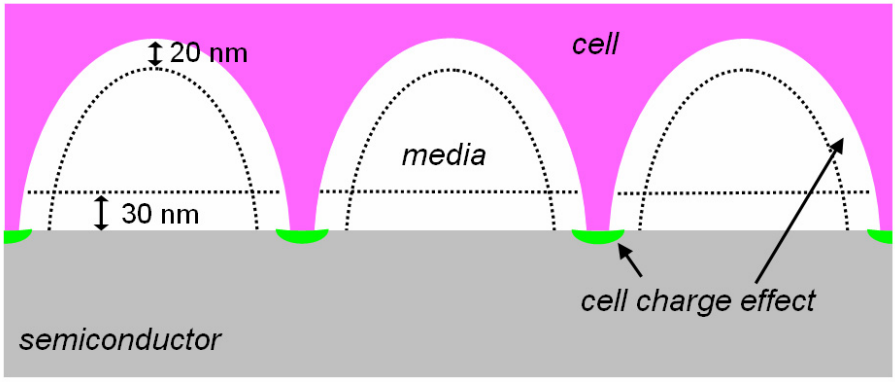

Figure 5.11. Schematic illustrating the limited electronic effect of the cell charge on the semiconductor. The Gouy layers for the cell-media (~ 20 nm) and for the semiconductor-media (30 nm) systems are indicated.

It appears that, for the assumptions previously made and in the most optimistic case, only 10% of the total cell charge has a direct effect on the semiconducting substrate. The remaining charge is too far away from the semiconductor surface to possibly have any effect on its electronic status. As explained in § 5.3, it is reasonable to assume that the charge associated with the adherent cells used is significantly lower than the one that erythrocytes display. This causes even lower zeta potentials and shorter potential decays which, combined with the reduced cell-substrate contact area, may lead to the non-detected electronic interaction between adherent mammalian cells and SiC surfaces.

Last in this section we will discuss the results presented in § 5.5. As we already mentioned, the results obtained from CPD investigations of RBC-SiC systems differ from the ones we would theoretically expect because the surface potentials observed for n- and p-type samples upon addition of RBC did not behave in a fashion consistent with the addition of negative charges. Moreover, the tendency of the measured potentials to converge to a null value upon addition of increasing RBC concentrations both for n- and p-type samples did suggest that the obtained results were probably caused by a measurement-related deficiency rather than by the electrical charge associated with RBCs. We identified two possible causes of the observed behavior: 1) a pH related decrease of the Helmholtz capacitance contribution; 2) a decreased light penetration within the erythrocyte solution. Since the Helmoholtz capacitance (C_H) is strongly dependent on the pH of the electrolyte solution [13], a decrease in its value influenced by an increase in the pH, which could have been caused by the addition of erythrocytes in PBS, may have affected the final measured V_{cpd} by making the Helmholtz layer contribution non-negligible. However, this possibility was soon eliminated after the pH

of erythrocytes was found to be extremely close to the one of the PBS solution (e.g, 7.33 for the erythrocytes compared to 7.4 for PBS) [133]. Since the Helmholtz potential varies by 60 mV per pH unit, such a small pH variation would not cause the significant effects observed in § 5.5. On the other hand, the reduction of light penetration within the erythrocyte solution immediately appeared as a valid explanation for the obtained results. In fact, it has been reported in optical studies of intravascular structures that the refractive index (η) mismatch between erythrocyte cytoplasm and blood plasma causes strong light scattering [134, 135]. Specifically, the refractive index of the erythrocyte is $\eta = 1.4$ vs. $\eta = 1.337$ presented by the blood plasma. The main component in the erythrocyte that influences the final refractive index of the cell is hemoglobin, which presents $\eta = 1.615$ and makes up roughly 97% of the entire erythrocyte dry content [136]. The same scattering mechanism exists for erythrocytes suspended in saline solution, which presents a refractive index equal to that of water ($\eta = 1.33$). Since all the experiments with RBCs were performed using PBS and since the calculation of the CPD voltage under deep illumination was made by shining light through the erythrocyte containing solution, it appears very likely that part of the light shone did not reach the semiconductor surface due to photon scattering by the RBCs. Moreover, another light related phenomenon, that probably has an even stronger effect on the final CPD results reported in § 5.5, takes place upon illumination of erythrocytes: light absorption. Also in this case, hemoglobin is mainly responsible, causing major absorption at lower wavelengths (λ), specifically for $\lambda < 400$ nm [137]. Since the wavelength of the LEDs used in our CPD system was $\lambda = 370$ nm, and the hemoglobin penetration depth at these wavelengths is at most 20.6 μm, it is correct to assume that part of the light shone through the PBS-erythrocyte solution was

absorbed and a portion, as aforementioned, was scattered. This combined mechanism is the most likely cause of the apparent decrease in the surface potentials measured in § 5.5 upon addition of increasing amounts of RBCs. In fact, the higher the concentration of RBCs in PBS solution, the more likely it is that a single photon will not reach the semiconductor surface because of scattering or absorption mechanisms. Hence, the low light intensity reaching the sample surface was probably not sufficient to create the flatband condition that characterized the measurement upon strong illumination and the $V_{cpd,light}$ value tended to match the $V_{cpd,dark}$ value.

Specifically, we observed a φ_s reduction upon addition of 1% RBCs in PBS: in this case the cell density (ρ_c) in the solution was 64×10^3 cells/μL. Ideally assuming that the cells are points equally spaced within the solution we can calculate a total of $\sqrt[3]{\rho_c} = 40$ cells along one of the dimensions of a 1 mm^3 cube. This assumption implies that the average distance between RBCs would be d_c = 1 mm / 40 = 25 μm. Considering their biconcave shape and assuming an average diameter of 6 μm and thickness of 1.2 μm [138] their average distance is found to be 23.2 μm. Because of the concave shape of the cells, the probability that the plane of incidence and of exit for a single incident photon are parallel strongly decreases, which, applied for a large number of cells, leads to a significant scattering mechanism (Fig. 5.12). Furthermore, hemoglobin is a high percentage within the erythrocytes cytoplasm. Assuming a maximum light penetration depth within the intracellular hemoglobin solution of 20.6 μm and a minimum erythrocyte dimension of 1.2 μm, the probability that a light photon will pass through more than 16 cells is extremely low. For a cell density of 3.2×10^6 cells/μL the measured φ_s was null. Proceeding as above we obtain that in this case the average distance of the

cells (considered as points) is d_c = 1mm / $\sqrt[3]{\rho_c}$ = 6.8 µm which therefore indicates a close-packed structure in the real case and a practical impossibility for photons to reach the semiconductor surface.

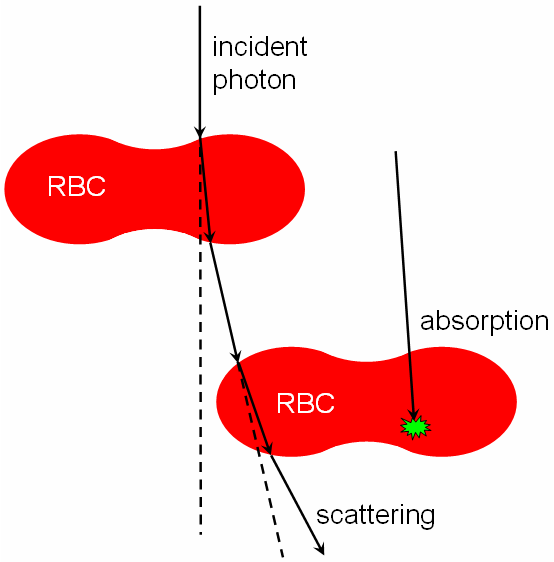

Figure 5.12. Schematic representation of the scattering and absorption of photons by the hemoglobin contained in the cell.

Summarizing, the cell concentration dependent φ_s measured in § 5.4 is, unfortunately, not caused by the electrical charge of cells but by the light scattering and absorption operated by hemoglobin. While the effect of cells on semiconductor surfaces may be present, other methods for measuring this interface electrically are needed and will be discussed in the next chapter.

5.7. Summary

In conclusion we have reported pioneering and challenging work that has been done to this point to try to investigate the electronic interactions between a semiconductor and a biological cell. We have described the experimental procedures developed for

performing CPD measurements of semiconductor-electrolyte systems and we have shown that, thanks to an appropriate calibration of the system and to suitable experimental approaches, CPD measurements of semiconductors in liquid are not only possible but highly repeatable. Despite the success reached in the preparatory phase necessary for the implementation of CPD measurements of semiconductor-cell-electrolyte systems, the results obtained from the final measurements did not yield the desired results. It appears that the electronic effect of cell charge on the semiconductor energy bands is lower in magnitude than expected and therefore not detectable with the implemented CPD system which displayed a maximum accuracy of roughly 15 mV. In addition we have developed a theoretical model that identifies a major issue in the cell adhesion morphology: since cells are in strict contact with the semiconducting surface only in the proximity of adhesion plaques, the quantity of charge that, in a liquid environment, can affect the electronic status of the semiconductor is drastically reduced. For CPD investigations of RBC-SiC systems, where a stronger cell electronic effect might have been expected, optical issues complicated the matter making it impossible to probe the effect of cell charges on the semiconductor electronic state with a method utilizing illumination. A careful examination of the results and insightful determination of their possible causes kept us from mistakenly associating the observed promising results with the effect of erythrocytes' charge on the semiconductor surface potential.

We believe that the results presented in this section, revealing many of the possible problems that may be encountered when studying cell-semiconductor systems via CPD, may be extremely helpful for the future implementation of improved apparatus suitable for cell-semiconductor electronic interaction investigations. In fact, we do not exclude *a*

priori the possibility that, by increasing the measuring sensitivity of the CPD apparatus used (e.g., lowering the average standard deviation of measurements in liquid below 15 mV)) and by using cells that display a higher charge than the ones used in this work, an effect of the cell charge on the electronic status of the semiconductor substrate may be monitored. However, since still very few data presently exist regarding the surface charge of biological cells, and since the surface charge is dependent on the media where cells are suspended, it may be particularly difficult to select the right cell-media combination which may yield successful results. CPD monitoring of electrogenically active cells (e.g., neurons) cultured on SiC surfaces may be a study approach that could possibly lead to the detection of measurable electronic signals (e.g., observation of the electric extracellular 'spikes' which offers the possibility of an AC measurement technique and thus higher signal to noise ratio). Also, other techniques may be tried in the future to study the still unknown cell-semiconductor electronic interactions. However, this interesting matter goes beyond the purpose of this chapter and hence will be exhaustively treated in Chapter 6.

Chapter 6. Conclusion and Future Work

6.1. Conclusion

This work is an extensive study which investigates the properties of crystalline SiC (e.g., 3C-, 4H-, and 6H) for bio-sensing applications. In Chapter 2, we have described how we prepared SiC surfaces for morphological, chemical and crystallographic characterization by using H-etching. An optimum etching process has been developed for each SiC polytype, yielding well-ordered, atomically flat surfaces perfectly suitable for surface science studies. This allowed us to characterize in depth the surfaces of all the studied polytypes and in particular H-etched 3C-SiC surfaces that have displayed, upon LEED analysis, a surface reconstruction (e.g., (5×1)) never investigated in the past. The SiC surfaces presented and characterized in Chapter 2 are extremely appealing for bio-research applications. In fact, several biomolecular surface science studies are presently investigating the interaction of cell proteins with well-prepared, atomically flat surfaces for achieving a better understanding of the semiconductor/cell interface [139, 140]. In Chapter 3 we have shown, for the first time, that single-crystal SiC is biocompatible and capable of directly interfacing cells without the need for surface functionalization. Also, SiC has been shown to be significantly better than Si as a substrate for cell culture, with a noticeably reduced toxic effect and enhanced cell proliferation. This result opens up exciting perspectives for the use of SiC in bio-technological applications, suggesting that SiC should be preferred to Si which, at present, is the leading crystalline semiconductor

for bio-applications. The main factors that have been shown to define SiC biocompatibility are its hydrophilicity and surface chemistry. SiC surface morphology is shown to influence cell adhesion only when macropatterned while SiC polytypism and doping concentration seem to have no influence on cell proliferation. We have also brought to attention how the cleaning chemistry may affect cell proliferation and emphasized the importance of the selection of an appropriate cleaning procedure for bio-substrates. From the results reported in Chapter 3 it can be easily concluded that SiC is an ideal substrate for bio-applications such as smart-implants, drug delivery and cellular electronic interaction studies. The latter possibility has been particularly investigated in Chapters 4 and 5 leading to interesting results. Specifically, in Chapter 4, a CPD apparatus has been implemented and calibrated for measurements of semiconductors immersed in liquid, that in the past have been shown to be particularly challenging. This measurement apparatus has been used to characterize the electronic status of SiC surfaces upon different chemical charging processes and has also been used to investigate the effect that H-etching has on the electrical properties of SiC polytypes (e.g., measurements in air, Chapter 4). From these studies we have obtained an accurate description of the response of SiC surfaces to added charges and the novel result that H-etching electronically passivates 3C-SiC(001) surfaces. The latter finding may be a topic for future studies both in the surface science and in the bio-medical fields. In Chapter 5, CPD measurements of SiC surfaces immersed in electrolytes have been performed and the obtained results have been discussed with the aid of existent theoretical models to define the electronic effect of different electrolytes on SiC surfaces. Unfortunately, CPD measurements of semiconductor-cell-electrolyte systems did not reveal a measurable

effect of mammalian cell charge on the electronic status of SiC surfaces. However, this acquired knowledge has allowed us to create a model where cell adhesion morphology and electric field decay are of primary importance in defining the amount of charge actively influencing the semiconductor surface. Because of this model, it appears that the cell charge effect on semiconducting surfaces is smaller in magnitude than initially estimated and cannot be detected with a measuring system which presents a maximum accuracy of 15 mV.

Summarizing, this work exhaustively investigated SiC's surface characteristics and bio-potentialities and for the first time introduced crystalline SiC as a biomaterial. At the same time a pioneering first step which helps to move towards a better understanding of cell-semiconductor electronic interactions was made, leading to interesting results that may help to select new approaches for successful future investigations (§ 6.2).

6.2. Future work

The impossibility of detecting the charge associated with cells while performing CPD measurements (§ 5.4-6) has been explained by a suitable model (§ 5.6) that identifies cell adhesion morphology and cell charge electrical decay as two of the major causes. However, the initial idea of detecting, using a contactless technique, the band bending induced by cells in semiconducting surfaces is still extremely appealing and should not be abandoned. Possible modifications that could be made to the presented CPD measurements and hence lead to successful results are as follows: 1) elimination of the deep illumination feature that has been shown to complicate the measurement (Chapter 5); 2) monitoring of adherent electrogenically active cells such as neurons, heart muscle cells, or toad bladder epithelial cells [122, 141, 142] since their electrical activity

has been well characterized by previous studies [132]. Hence, time-dependent monitoring of the electrical activity of these cells and its influence on the semiconductor electronic state could be attempted. The observation of the effect of an AC signal on the semiconductor space charge would be most likely facilitated by the higher signal to noise ratio of the experiment.

Also, completely different approaches may be attempted to investigate the electronic effect of cells on semiconducting surfaces. One possibility would be, for example, to use XPS measurements of semiconducting surfaces whose molecules are bonded to adhesion proteins to define the entity of band bending introduced by the biological matter. In fact, as already discussed in Chapter 4, core level binding energies in XPS spectra vary with the energy band bending and can be used to quantify energy band shifts. Furthermore, XPS studies could be performed to identify the chemical components of the adhesion proteins remaining on sample surfaces after trypsinization or RCA cleaning (Chapter 3). We actually have already started, in collaboration with Dr. Starke's group (Max Planck Institute, Stuttgart, DE), the aforementioned XPS investigations which have provided promising preliminary results. Specifically, two 3C-SiC substrates were used in these preliminary experiments. HaCaT human keratinocytes cells were cultured on one, while the other was used as control. Both samples were immersed in media during cell culture and then the cells were trypsinized (Trypsin + EDTA, (ATCC)) after a thorough rinse in PBS. Subsequently, the samples were immersed in DMEM culturing mdia (10 % of FBS added) to block the trypsinization process and leave part of the adhesion proteins attached to the substrate, and then rinsed in DI water. XPS analysis of the two surfaces provided interesting results. The sample

with adhesion proteins displayed a higher content of carbon with several unknown components (see Fig. 6.1).

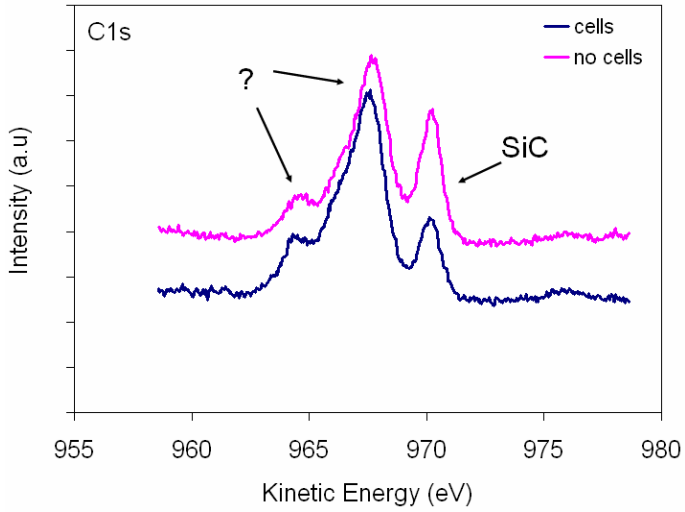

Figure 6.1. XPS spectra of 3C-SiC samples with and without cell adhesion proteins.Several unknown C-peaks are present in both the spectra. No comparison should be made between the peak magnitudes of the two samples; only elemental percents within an individual sample are significant.

The identification of the different carbon chemical components present on the spectra may yield precious information regarding the binding mechanism between SiC and mammalian cells. Also, in-depth studies of core binding energy levels for these samples may lead to the quantification of energy band shifts induced by the presence of biological material.

The interesting passivating effect that hydrogen etching has on 3C-SiC surfaces will surely be a rich topic for future investigations. Scanning tunneling microscopy (STM) could be used to finalize a model to describe the surface structure of H-etched 3C-SiC(001) samples. Also, additional ATR-FTIR or infrared absorption spectroscopy (IRAS) studies may be performed to investigate in depth the molecular binding present at

this surface which are a probable cause of the observed electronic passivation [143]. Since it has been suggested that transfer of electrons from the occupied valence band of proteins into free states of the semiconductor may cause protein modifications [30, 12], the electronic passivation observed on etched 3C-SiC surfaces may lead to different enlightening experiments. Proteins (e.g., fibrinogen) could be deposited on electronically passivated and standard 3C-SiC surfaces. A direct comparison of the protein behavior (e.g., if electronic exchange occurs, fibrinogen decomposes into fibrin monomer and fibrino-peptide) would allow detection of differences in the electronic behavior of the two substrates. If, for example, proteins do not decompose on the H-etched surfaces (as might be expected due to the electronic passivation), H-etched 3C-SiC surfaces would represent an ideal material for blood sensing devices. It is in fact known that a high charge exchange between blood proteins and contacting surfaces leads to thrombo-formation.

Zeta potential measurements of SiC surfaces could also be attempted to better understand the electronic behavior of this material within electrolytes. The results obtained from these studies would be of fundamental importance for a better definition of the potentiality of this material for *in-vivo* applications and may facilitate future cell-electronic interactions studies.

References

1. J.T Groves, "Learning the chemical language of cell-surface interactions," *Science's STKE*, pp. 45, 2005.

2. M.A. Hjortso and J.W. Roos, "Cell adhesion in bioprocessing and biotechnology," 1st edition, CRC, 1994.

3. M.F. Maitz, M. Pham, E. Wieser, "Blood compatibility of titanium oxides with various crystal structure and element doping," *Journal of biomaterials applications* 17, (4), pp. 303-319, 2003.

4. I. Simon-Reuss, G.M. Cook, G.V.F. Seaman, and D.H. Heard, "Electrophoretic studies on some types of mammalian tissue cell," *Cancer Research* 24, pp. 2038-2043, Dec. 1964.

5. C. Sato, K. Kojima, M. Onozawa, and T. Matsuzawa, "Relatioship beteen recovery of cell surface charge and colony-forming ability following radiation damage in three cell-lines," *Int. J. Radiat. Biol,* 22, (5), pp. 479-488, 1972.

6. H.A. Abramson and L. S. Moyer, "The electrical charge of mammalian red blood cells," *Journal of General Physiology*, pp. 601-607, 1935.

7. M. Abercrombie and E.J. Ambrose, "The surface properties of cancer cells: a review," *Cancer Research* 22, pp. 525-548, June 1962.

8. S.C. Bayliss, L.D. Buckberry, P.J. Harris, M. Tobin, "Nature of the Silicon-Animal Cell Interface," *Journal of Porous Material* 7, pp. 191-195, 2000.

9. A.H. Mayne, S.C. Bayliss, P. Barr, M. Tobin, and L.D. Buckberry, "Biologically interfaced porus silicon devices," *Phys. Stat. Sol. (a)*, 182, pp. 505, 2000.

10. S.C. Bayliss, P.J. Harris, L.D. Buckberry, C. Rousseau, "Phosphate and cell growth on nanostructured semiconductors," *Journal of Material Science Letters* 16, pp. 737-740, 1997.

11. A. Angelescu, I. Kleps, M. Mihaela, M. Simion, T. Neghina, S. Petrescu, N. Moldovan, C. Paduraru and A. Raducanu, "Porus silicon matrix for applications in biology," *Rev. Adv. Sci.* 5, pp. 440-449, 2003.

12. J.Y. Chen, Y.X. Leng, X.B. Tian, L.P. Wang, N. Huang, P.K. Chu, and P. Yang, "Antithrombogenic investigation of surface energy and optical bandgap and hemocompatibility mechanism of $Ti(Ta^{+5})O_2$ thin films," *Biomaterials* 23, pp. 2545-2552, 2002.

13. X.G. Zhang, "Electrochemistry of silicon and its oxide," Kluwer Academic /Plenum Publishers, New York, 2001.

14. J.I. Carrasso and M.M. Faktor, "Oxidation reactions and potentials of germanium and silicon," in "The electrochemistry of semiconductors," P.J. Holmes Editor, Academic Press, London, 1962, pp. 205-255.

15. X. Li, X. Wang, R. Bondokov, J. Morris, Y.H. An, T.S. Sudarshan, "Micro/Nanoscale Mechanical and Tribological Characterization of SiC for Orthopedic Applications," *J. Biomed. Mater. Res. B: Appl. Biomater.* 72, (2), pp. 353-61, 2005.

16. P. Gonzalez, J. Serra, S. Liste, S. Chiussi, B. Leon, M. Perez-Amor, J. Martinez-Fernandez, A.R. de Arellano-Lopez, F.M. Varela-Feria, "New biomorphic SiC ceramic coated with bioactive glass for biomedical applications," *Biomaterials* 24, pp. 4827-4832, Nov. 2003.

17. S. Santavirta, M. Takagi, L. Nordsletten, A. Anttila, R. Lappalainen, Y.T. Konttinen, "Biocompatibility of silicon carbide in colony formation test in vitro," *Arch. Orthop. Trauma Surg.* 118, pp. 89-91, 1998.

18. L. Nordsletten, A.K. Hogasen, Y.T. Konttinen, S. Santavirta, P. Aspenberg, and A.O. Aasen, " Human monocytes stimulation by particles of hydroxyapatite, silicon carbide and diamond: in vitro studies od new prosthesis coatings," *Biomaterials* 17, pp. 1521-1527, 1996.

19. P. Aspenberg, A. Aniila, Y.T. Konttinen *et al.*, "Benign response to particles of diamond and SiC. Bone chamber studies of new joint replacement coating materials in rabbit," *Biomaterials* 17, pp. 807-812, 1995.

20. U. Kalnins, A. Erglis, I. Dinne, I. Kumsars, S. Jegere, "Clinical outcomes of silicon carbide coated stents in patient with coronary disease," *Med. Sci. Monit.* 8, (2), 2002.

21. H.G. Yamins, W.A. Zisman, "A new mothod of studying the electrical properties of monomolecular films on liquids," *J. Chem. Phys.* 1, pp. 656, 1933.

22. E.F. Porter, "Monomolecular films of α-aminostearic acid, stearic acid, and heptadecylamine," *J. Am Chem. Soc.* 59, pp. 1883, 1937.

23. S. Rosenfeld, W.M. Hoskins, “A modified Zisman apparatus for measuring contact potential differences in air,” *Rev. Sci. Instrum.* 16, 343, 1945.

24. K. Jan and S. Chien, “Role of surface electric charge in red blood cell interactions,” *The Journal of General Physiology* 61, pp. 638-654, 1973.

25. D.C. Chang, “Guide to electroporation and electrofusion,” D.C Chang, B.M. Chassy, J.A. Saunders and A.E. Sowers Eds., Academic Press, Inc., San Diego, 1992.

26. D.D. Clayton, “Presolar galactic merger spawned SiC grain mainstream,” *Lunar and Planetary Science XXXIV*, pp. 1059, 2003.

27. W.J. Choyke and G. Pensl, “Physical properties of SiC,” *MRS Bulletin* 185-188, March 1997.

28. S.E. Saddow and A. Agarwal, “Advances in silicon carbide processing and applications,” Artech House, Inc., Norwood, MA, 2004.

29. S.H. Monnink, A.J. van Boven, H.O. Peels, I. Tigchelaar, P.J. de Kam, H.J. Crijns, and W. van Oeveren, *Journal of Investigative Medicine* 47, 304, 1999.

30. A. Bolz and M. Schaldach, “Artificial heart valves: improved blood compatibility by PECVD a-SiC:H coating,” *Artificial Organs* 14, (4), pp. 260-269, 1990.

31. Y. Takami, S. Yamane, K. Makinouchi, G. Otsuka, J. Glueck, R. Benkowski, and Y. Nose, “Protein adsorption onto ceramic surfaces,” *Journal of Biomedical Materials Research* 40, (1), pp. 24-30, Dec. 1998.

32. D. Carrie, K. Khalife, M. Hamon, *et al.*, ”Initial and follow-up results of the Tenax coronary stent,” *J. Intervent Cardiol,* 14, pp. 1-5, 2001.

33. J.A. Fournier, J. Calabuig, A. Merchan, *et al.*, “Initial results and 6-month clinical follow-up after implantation of a silicon carbide coated coronary stent,” *Rev. Esp. Cardiol.* 54, pp. 567-572, 2001.

34. C. Hamm, “TENAX-XR a:SiC-H coated stent versus noncoated stents in 485 patients with acute coronary syndrome: 9- and 18-month uollow-Up: the TRUST trial,” *J. Am. Coll. Cardiol.* 39, 310A, 2002.

35. M.B. Leon, G.S. Mintz, “Interventional Vascular Product Guide,” Martin-Dunitz, London, 1999.

36. A.J. Rosenbloom, D.M. Sipe, Y. Shishkin, Y. Ke, R.P. Devaty and W.J. Choyke, Nanoporus SiC: A Candidate Semi-Permeable Material for Biomedical Applications, *Biomedical Microdevices* 6, (4), pp. 261-267, 2004.

37. A. Naji and M.F. Harmand, "Cytocompatibility of two coating materials, amorphousalumina and silicon carbide, using human differentiated cell cultures," *Biomaterials* 12, (7), pp. 690-694, 1991.

38. M. Allen, R. Butter, L. Chandra, A. Lettington, and N. Rushton, "Toxicity of particulate silicon carbide for macrophages, fibroblasts and osteoblast-like cells in vitro," *Bio-Medical Materials and Engineering* 5, (3), pp. 151-159, 1995.

39. I. Svensson, E. Artursson, P. Leanderson, R. Berglind, and F. Lindgren, "Toxicity of some silicon carbides and silicon nitrides: whiskers and powders," *American Journal of Industrial Medicine* 31, pp. 335-343, 1997.

40. D.K. Schroeder, "Semiconductor material and device characterization," 2nd Edition, Wiley-Interscience, 1998.

41. C.P. Sherman Hsu, "Infrared Spectroscopy" in "Handbook of instrumental techmiques for analytical chemistry," F.A. Settle Editor, Prentice Hall, 1997, pp. 247-283.

42. L. Kronik and Y. Shapira, "Surface photovoltage phenomena: theory, experiment, and applications," *Surface Science Reports* 37, pp. 1-206, 1999.

43. D.K. Schroeder, "Surface voltage and surface photovoltage: history, theory and applications," *Meas. Sci. Technol*. 12, R16-31, 2001.

44. W. Thomson (Lord Kelvin), *Phil. Mag.* 46, 82, 1898.

45. A. Savtchouk, E. Oborina, A.M. Hoff, and J. Lagowski, "Non-contact Doping Profiling in Epitaxial SiC**,"** *Materials Science Forum* Vols. 457-460, pp. 1349-1352, 2004.

46. R.S. Muller and T.I. Kamins, "Device electronics for integrated circuits," 2nd Edition, John Wiley & Sons, 1977.

47. S.R. Morrison, "Electrochemistry at semiconductor and oxidized metal electrodes," Plenum Press, New York, 1980.

48. H.F. Okorn-Schmidt, "Characterization of silicon surface preparation processes for advanced gate dielectrics," *IBM J. Res. Develop.* 43, (3), May 1999.

49. P.P. Konorov, A.M. Yafyasov, and V.B. Bogevolnov, "Field effect in semiconductor-electrolyte interfaces," Princeton University Press, New Jersey, 2006.

50. C.J. Anthony, A.J. Pidduck, M.J. Uren, "Surface morphology improvement of SiC epitaxy by sacrificial oxidation," *Mater Sci. Forum* 264-268, pp. 367-370, 1998.

51. U. Starke, Ch. Bram, P.R. Steiner, W. Hartner, L. Hammer, K. Heinz, K. Muller, *"*The (0001)-surface of 6H-SiC: morphology, composition and structure*," Appl. Surf. Sci.* 89, 175, 1995.

52. M. Shur, S. Rumyantsev, M. Levinshtein, "SiC materials and devices," Volume 1, World Scientific, 2006, 761.

53. J.S. Shor in "Properties of SiC", Ed. G.L. Harris, EMIS Data Review No. 13, INSPEC, London, UK, 1995, pp. 141-149.

54. L. Zhou, V. Audurier, P. Pirouz, J.A. Powell, "Chemomechanical polishing of silicon carbide," *J. Electrochem. Soc.* 144, L161, 1997.

55. S.J. Pearton, "Wet and dry etching of SiC," Chapter 4 in "Process technology for silicon carbide devices," C.M. Zetterling Editor, Institution of Electrical Engineers, INSPEC, 2002.

56. J. Bernhardt, J. Schardt, U. Starke and K. Heinz, "Epitaxially ideal oxide-semiconductor interfaces: silicate adlayers on hexagonal (0001) and (000-1) SiC surface," .*Appl. Phys. Lett.* 74, pp. 1084, 1999.

57. T. Seyller, "Passivation of hexagonal SiC surfaces by hydrogen termination," J. Phys.: Cond. Mat., 16**,** S1755, 2004.

58. S. Soubatch, S.E. Saddow, S.P. Rao, W. Y. Lee, M. Konuma, and U. Starke, "Structure and Morphology of 4H-SiC Wafer Surfaces after H2-Etching," *Mat. Sci. Forum* 483-485, pp. 761, 2005.

59. Z.Y. Xie, C.H. Wei, L.Y. Li, Q.M. Yu, J.H. Edgar, "Gaseous etching of 6H-SiC at relatively low temperatures," *Journal of crystal growth* 217, pp. 115-124, 2000.

60. S. Karmann, W. Suttrop, A. Schoner, M. Schadt, C. Haberstoh, F. Engelbrecht, R. Helbig, G. Pensl, R.A. Stein, S. Leibenzeder, "Chemical vapor deposition and characterization of undoped nitrogen-doped single crystalline 6H-SiC," *J. Appl Phys*. 72, pp. 5437, 1992.

61. J.A. Powell, D.J. Larkin, P.B. Abel, "Surface morphology of silicon carbide epitaxial films," *J. Electron. Mater.* 24, pp. 295, 1995.

62. C. Hallin, F. Owman, P. Martensson, A. Ellison, A. Konstantinov, O. Kordina, E. Janzen, "In situ substrate preparation for high-quality SiC chemical vapour deposition;" *Journal of crystal growth* 181, pp. 241-253, 1997.

63. V. Ramachandran, M.F. Brady, A.R. Smith, R.M. Feenstra, D.W. Greve, "Preparation of atomically flat surfaces on silicon carbide using hydrogen etching," *Journal of Electronic Materials* 27, (4), 1998.

64. F. Owmann, C. Hallin, P. Martensson, E. Janzen, "Removal of polishing induced damage from 6H-SiC(0001) substrates by hydrogen etching," *Journal of crystal growth* 167, pp. 391-395, 1996.

65. R. L. Myers, Y. Shishkin, O. Kordina, and S.E. Saddow, "High growth rates (>30μm/h) of 4H-SiC epitaxial layers using a horizontal hot-wall CVD reactor", *Journal of Crystal Growth* 285**,** pp. 483-486, 2005.

66. Meralys Reyes-Negron, Yevgeniy Shishkin, S. Harvey and Stephen E. Saddow, "Development of a high-growth rate 3C-SiC on Si CVD process," *Mater. Res. Soc. Symp. Proc* 911, pp. 79, 2006.

67. C. Coletti, M.J. Jarozseski, M. Reyes, A.M. Hoff, S. Harvey, and S.E. Saddow,"3C-SiC(001) on Si(001) films for biotechnological applications," Book of abstracts of Hetero-SiC '07 28-29 June 2007, Grenoble, France.

68. C.L. Frewin, "Design and implementation of a 200 mm 3C-SiC CVD reactor," M.S. Thesis, Dept. Elect. Eng., University of South Florida, Tampa, FL, 2006.

69. C. Coletti, M. Hetzel, C. Virojanadara, U. Starke, and S. E. Saddow, "Surface morphology and structure of hydrogen etched 3C-SiC(001) on Si(001)," *Mater. Res. Soc. Symp. Proc.* 911, pp. 131, 2006.

70. R. Kaplan, *Surf. Sci*. 215, 111, 1989.

71. V. Bermudez, *Phys. stat. sol (b)* 202, 447, 1997.

72. C. Coletti, S.E. Saddow, M. Hetzel, C. Virojanadara, and U. Starke, "Surface studies of H2-etched 3C-SiC(001) on Si(001)," *Applied Phyisics Letters* 91, pp. 061914, Aug. 2007.

73. P.G. Soukiassian, and H.B. Enriquez, "Atomic scale control and understanding of cubic silicon carbide surface reconstructions, nanostructures and nanochemistry," *J. Phys.: Cond. Mat*. 16, S1611, 2004.

74. M. D'Angelo, H. Enriquez, M.G. Silly, V. Derycke, V. Yu. Aristov, P. Soukiassian, C. Ottavianni, M. Pedio and P. Perfetti, *Mat. Sci. Forum* 457-460, 399, 2004.

75. S. Hara, W.F.J. Slijkerman, J.F. van der Veen, I. Odhomari, S. Misawa, E. Sakuma and S. Yoshida, *Surf. Sci.* 231, L196, 1990.

76. J.M. Powers, A. Wander, P.J. Rous, M.A. van Hove, and G.A. Somorjai, *Phys. Rev. B* 44, 11159, 1991.

77. J. Pollmann, P. Krüger and W. Lu, "Theory of structural and electronic properties of cubic SiC surfaces," *Mat. Sci. Forum* 338-342, 369, 2000.

78. U. Starke, W.Y. Lee, C. Coletti, S.E. Saddow, R.P. Devaty, and W.J. Choyke, "SiC Pore Surfaces: Surface Studies of 4H-SiC (-1102) and 4H-SiC (-110 -2)," *Applied Physics Letters* 88, (3), pp. 031915, 2006.

79. U. Starke, J. Bernhardt, J. Schardt, and K. Heinz, "SiC surface reconstruction: relevancy of atomic structure for growth technology," *Surf. Rev. Lett.* 6, pp. 1129, 1999.

80. A. Sagar, C.D. Lee, R.M. Feenstra, C.K. Inoki, and T.S. Kuan, "Morphology and effects of hydrogen etching of porous SiC," *J. Appl. Phys*. 92, pp. 4070, 2002.

81. A.A. Burk Jr., L.B. Rowland, "The role of excess silicon and in situ etching on 4H-SiC and 6H-SiC epitaxial layer morphology," *Journal of Crystal Growth* 167, pp. 586-595, 1996.

82. S. Dogan, A. Teke, D. Huang, H. Morkoc, C. B. Roberts, J. Parish, B. Ganguly, M. Smith, R. L. Myers and S. E. Saddow, "4H-SiC photoconductive switching devices for use in high-power applications," *Applied Physics Letters* 82, (18), pp. 3107-3109, 2003.

83. R.L. Meyers, "High Growth Rate SiC CVD via Hot-Wall Epitaxy," Ph.D. dissertation, , Dept. Elect. Eng., University of South Florida, Tampa, FL, 2006.

84. D.R. Shankln and D.L. Smalley, "The immunopathology of siliconosis. History, clinical presentation, and relation to silicosis and the chemistry of silicon and silicone," *Immunol. Res.* 18, 125, 1998.

85. I. Svensson, E. Artursson, P. Leanderson, R. Berglind, and F. Lindgren, *Amer. J. Ind. Med.* 31, 335, 1997.

86. C.C. Perry and T. Keeling-Tucker, "Aspects of the bioinorganic chemistry of silicon in conjunction with the biometals calcium, iron and aluminium," *J. Inorg. Biochem.* 69, 181, 1998.

87. C. Coletti, M. Jaroszeski, A. M. Hoff and S.E. Saddow, "Culture of mammalian cells on single crystal SiC substrates," *Mater. Res. Soc. Symp. Proc.* 950, 2006.

88. C. Coletti, M.J. Jaroszeski, A. Pallaoro, A.M. Hoff, S. Iannotta and S.E. Saddow, "Biocompatibility and wettability of crystalline SiC and Si surfaces," *IEEE EMBS Proceedings***,** pp. 5849-5852, 2007.

89. M. Okada, H. Karube, M. Niitsuya, Y. Aizawa, I. Okayasu, and M. Kotani, "In vitro toxicity of gallium arsenide in alveolar macrophages evaluated by magnetometry, cytochemistry and morphology," *Tohoku J. Exp. Med.*189, (4), 1999.

90. S.C. Bayliss, R. Heald, D.I. Fletcher, and L.D. Buckberry, "The culture of mammalian cells on nanostructured silicon," *Advanced Materials* 11, (4), pp.318-321, 1999.

91. P. Somasundaran, " Encyclopedia of surface and colloid science," CRC Press, pp. 1526, 2006

92. R.I. Freshney, "Culture of animal cells," John Wiley & Sons, Inc., Hoboken, NJ, 2005, pp. 105-113.

93. B.D. Boyan, T.W. Hummer, D.D. Dean, Z. Schwartz, "Role of material surface in regulating bone and cartilage cell response," *Biomaterials* 17, pp. 137-146, 1998.

94. D.D. Deligianni, N.D. Katsala, P.G. Koutsoukos, and Y.F. Missirlis, "Effect of surface roughness of hydroxyapatite on human bone marrow cell adhesion, proliferation, differentiation and detachment strength," *Biomaterials* 22, pp. 87-96, 2001.

95. M. Kononen, M. Hormia, J. Kivilaathi, J. Hautaniemi, and I. Thesleff, "Effect of surface processing on the attachment, orientation and proliferation of human gingival fibroblasts on titanium," *J. Biomed. Mat. Res.* 26, pp. 1325-1341, 1992.

96. X. Zhu, K.L. Mills *et al*., "Fabrication of reconfiguarable protein matrices by cracking," *Nature Materials* 4, May 2005.

97. R.G. Richards, "The effect of surface roughness on fibroblast adhesion *in vitro*," *Injury* 27, (3), pp 38-43, 1996.

98. B.G. Keselowsky, D.M. Collard, A.J. Garcia, "Integrin binding specificity regulates biomaterials surface chemistry effects on cells differentiation," *Proc. Natl. Acad. Sci. U.S.A.* 102, pp. 5953-5957, 2005.

99. Brian K. Brandley, Ora A. Weiszi, and Ronald L. Schnaarn, "Cell Attachment and Long-term Growth on Derivatizable Polyacrylamide Surfaces," *Journal of Biological Chemistry* 362, (13), pp. 6431-6437, May 1987.

100. A.S.G. Curtis, J.V. Forrester, and P. Clark, "Substrate hydroxylation and cell adhesion," *J. Cell Sci.* 86, pp. 9-24, 1986.

101. L.G. Jacobshon, I.V. Afanasyev-Charkin, D.W. Cooke, R.K. Schulze, R.D. Averitt, and M. Nastasi, "Incorporation of fluorine in hydrogenated silicon carbide films deposited by pulse glow discharge," *Journal of vacuum science and technology a: Vacuum, surfaces, and films* 22, (4), pp. 1223-1228, July 2004.

102. G. Hodes, "Electrochemistry of nanomaterials," Wiley-VCH, 2001.

103. J. Hubbell, “Materials as morphogenetic guides in tissue engineering,” *Curr. Opin. Biot.* 14, pp. 551-558, 2003.

104. R. Langer, D.A. Tirrell, “Designing materials for biology and medicine,” *Nature* 428, pp. 487-492, 2004.

105. B. Geiger, A. Bershadsky, R. Pankov, and K.M. Yamada, “Transmembrane extracellular matrix-cytoskeleton crosstalk,” *Nature Reviews* 2, pp. 793-805, Nov. 2001.

106. B. Wehrle-Haller, and B.A. Imhof, “The inner lives of focal adhesions,” *Trends in Cell Biology* 12, (8), pp. 382-389, Aug. 2002.

107. G. Cicero, G. Galli, and A. Catellani, “Interaction of water molecules with SiC(001) surfaces,” *J. Phys. Chem. B* 108, pp. 16518-16524, 2004.

108. R. Thewes, C. Paulus *et al.*, “Integrated circuits for the biology-to-silicon interface,” *ESSDERC Proceedings 2004*, pp.19-28, 2004.

109. J.F. III Rizzo, J. Wyatt, S. Kelly, and D. Shire, “Perpetual efficacy of electrical stimulation of human retina with a microelectrode array during short-term surgical trials,” *Invest. Ophtalmol. Vis. Sci.* 44, pp. 5362-9, 2003.

110. M.S. Humayun *et al.* “Visual perception in a blind subject with a chronic microelectronic retinal prosthesis,” *Vis. Res.* 43, pp. 2537-81, 2003.

111. http://www.monroe-electronics.com/

112. SDI, private communications.

113. H. Angermann, “Characterization of wet-chemically treated silicon interfaces by surface photovoltage measurements,” *Analytical and Bioanalytical Chemistry* 374, (4), pp. 676-680, Oct. 2002.

114. Th. Dittrich, H. Angermann, W. Fussel, and H. Flietner, “Electronic properties of the HF-passivated Si(111) surface during the initial oxidation in air,” *Phys. Stat. Sol. A* 140, 463, 1993.

115. H.R. Philipp, “Intrinsic optical absorption in single-crystal silicon carbide,” *Phisical Review* 111, (2), pp. 440-441, Jul. 1958.

116. S.F. Avramenko, S.I. Kirilova, V.S. Kiselev, V.E. Primachenko, E.F. Venger, and V.A. Chernobai, “Surface electron properties of 6H and 15R modifications of silicon carbide,” *Semicond. Sci. Technol.* 12, pp. 189-194, 197.

117. N. Sieber, B.F. Mantel, Th. Seyller, J. Ristein, L. Ley, "Hydrogenation of 6H-SiC as a surface passivation stable in air," *Diamond and Related Materials* 10, pp. 1291-1294, 2001.

118. Th. Seyller, "Electronic properties of SiC surfaces and interfaces: some fundamental and technological aspects," *Applied Physics A: Material Science & Processing* 85, (4), pp. 371-85, Dec. 2006.

119. K. Nauka, and T.I. Kamins, "Surface photovoltage measurements of hydrogen-treated Si surfaces," *Journal of the Electrochemical Society* 146, (1), pp. 292-295, 1999.

120. F. Amy, and Y.J. Chabal, "Interaction of H, O_2, and H_2O with 3C-SiC surfaces," *Journal of chemical physics* 119, (12), pp. 6201-09, Sept. 2003.

121. H. Tsuchida, I. Kamata, and K. Izumi, "Infrared spectroscopy of hydrides on the 6H-SiC surface," *Appl. Phys. Lett.* 70, (23), Jun. 1997.

122. A. Offenhusser, and W. Knoll, "Cell-transistor hybrid systems and their potential applications," *Trends in Biotechnology* 19, (2), Feb. 2001.

123. J.N.Y. Aziz, R. Genov, B.L. Bardakjian, M. Derchansky, and P.L. Carlem, "Brain-silicon interface for high-resolution *in vitro* neural recording," *Biomedical circuits and systems* 1, (1), pp. 56-62, Mar. 2007.

124. C. Sprossler, M. Denyer, S. Britland, W. Knoll, and A. Offenhusser, "Electrical recordings from rat cardiac muscle cells using field-effect transistors," *Phys. Rev. E* 60, pp. 2171-2176, 1999.

125. M. Krause, S. Ingebrandt, D. Ritcher, M. Denyer, M. Scholl, C. Sprossler, and A. Offenhausser, "Extended gate electrode arrays for extracellular signal recordings," Sens. & Act. B 70, pp. 101-107, 2000.

126. S. McLaughlin, "Electrostatic potentials at membrane solution interfaces," *Curr. Top. Membr. Trans.* 9, pp. 71-144, 1977.

127. "Zetasizer Nano Series user manual," Issue 1.1, pp. 16.4, Feb. 2004.

128. E.H. Eylar, M.A. Madoff, O.V. Brody, and J.L. Oncley, "The contribution of sialic acid to the surface charge of the erythrocyte," *The Journal of Biological Chemistry* 237, (6), Jun. 1962.

129. J. Wall, F. Ayoub, and P. O'Shea, "Interactions of macromolecules with the mammalian cell surface," *Journal of Cell Science* 108, pp. 2673-82, 1995.

130. C. Sato, K. Kojima, and K. Nishizawa, "Target of X irradiation and dislocation of sialic acid in decrease of cell surface charge of erythrocytes," *Radiation Research* 69, (2), pp. 367-74, Feb. 1977.

131. X. Huang, D.W. Greve, D.D. Nguyen, and M.M. Domach, "Impedance based biosensor array for monitoring mammalian cell behavior," *Sensors, Proceedings of IEEE* 1, pp. 304-9, Oct. 2003.

132. R. Ponsley, and R.C. Barr, "Bioelectricity a quantitative approach," 2nd edition, Kluwer Academic/Plenum Publishers, New York, 2000.

133. A. Alonso, A. Arrazola, A. Garciandia, N. Esparza, C. Gomez-Alamillo, J. Diez, "Erythrocyte anion exchanger activity and intracellular pH in essential hypertension," *Hypertension, Journal of the American Heart Association* 22, pp. 348-356, 1993.

134. V.V. Tuchin, R.K. Wang, E.I. Galanzha, and D.M. Zhelstkov, "Scattering model of whole blood at hemoglobin glycation monitored by refractive index measurement with OCT," *Lasers and Electro-Optics* 2, May 2004.

135. X. Xu, R.K. Wang, J.B. Elder, and V.V. Tuchin, "Effect of dextran-induced changes in refractive index and aggregation on optical properties of whole blood," *Phys. Med. Biol.* 48, pp. 1205-1221, 2003.

136. B. Rappaz, A. Barbul, F. Charriere, J. Kuhn, P. Marquet, R. Korenstein, C. Depeursinge, and P. Magistretti, "Erythrocytes volume and refractive index measurement with a digital holographic microscope," *Proceedings of SPIE* 6445, Optical Diagnostic and Sensing VII, G.L. Cote, A.V. Priezzhev, Editors, Feb. 2007.

137. http://omlc.ogi.edu/spectra/hemoglobin/index.html

138. R. Skalak, A. Tozeren, R.P. Zarda, and S. Chien, "Strain energy function of red blood cell membranes," *Biophys. J.* 13, (3), pp. 245-264, Mar. 1973.

139. T. Classen, M. Lingenfelder, Y. Wang, R. Chopra, C. Virojanadara, U. Starke, and G. Costantini, "Hydrogen and coordination bonding supramolecular structures of trimesic acid on Cu(110)," *J. of Phys. Chem. A*, accepted, 2007.

140. A. Pallaoro, T. Toccoli, C. Coletti, N. Coppede, L. Vanzetti, R. Canteri, S.E. Saddow, and S. Iannotta, "Study and characterization of different SiC terminations and their interactions with biomolecules," *XVIII Congresso Nazionale sulla Scienza e Tecnologia del Vuoto* (18th National Congress on Vacuum Science and Technology), Florence, Italy 2-4 April, 2007.

141. K.M. Lipman, R.T. Dodelson, and R.M. Hays, "The surface charge of isolated toad bladder epithelial cells," *The Journal of General Physiology* 49, 1966.

142. W.J. Parak, J. Domke *et al.*, "Electrically excitable normal rat kidney fibroblasts: a new model system for cell-semiconductor hybrids," *Biophysical Journal* 76, pp. 1659-67, Mar. 1999.

143. T. Miura, M. Niwano, D. Shoji, and N. Myiamoto, "Kinetics of oxidation on hydrogen-terminated Si(100) and (111) surfaces stored in air," *J. Appl. Phys.* 79, (8), pp. 4373-4379, Apr. 196.

About the Author

Camilla Coletti was born on November 9th 1979 in Marsciano (Perugia), Italy. In 1998, she earned the *Maturita' Scientifica* from the Scientific Liceum 'L. Salvatorelli' of Marsciano (IT). In 2004, she received the *Laurea* (M.S. degree) *cum laude* in electrical engineering from the University of Perugia (IT) with a thesis entitled "Characterization of Scanning Spreading Resistance Microscopy (SSRM) measurements by device simulation" performed in collaboration with the Swiss Federal Institute of Technology (ETH) of Zurich (CH). In 2005, she passed the *Esame di Stato* (italian Professional Engineer qualification) and entered the electrical engineering Ph.D. program at the University of South Florida (USF) in Tampa, FL (USA). During her Ph.D. program she has collaborated with the Max-Planck Institute (MPI) of Stuttgart (DE) and the Institute of Photonics and Nanotechnology of the Italian National Research Council (IFN-CNR) of Trento (IT) and authored two publications in *Applied Physics Letters* (one first author) and several peer-reviewed conference papers.